



UPPSALA
UNIVERSITET

*Digital Comprehensive Summaries of Uppsala Dissertations
from the Faculty of Science and Technology 1760*

Materials Modelling for Energy Harvesting

From Conversion to Application through Storage

AMITAVA BANERJEE



ACTA
UNIVERSITATIS
UPSALIENSIS
UPPSALA
2019

ISSN 1651-6214
ISBN 978-91-513-0544-8
urn:nbn:se:uu:diva-369695

Dissertation presented at Uppsala University to be publicly examined in 80101, Ångströmlaboratoriet, Lägerhyddsvägen 1, Uppsala, Thursday, 15 February 2018 at 09:15 for the degree of Doctor of Philosophy. The examination will be conducted in English. Faculty examiner: Prof. Dr. Tejs Vegge (Department of Energy Conversion and Storage, Technical University of Denmark).

Abstract

Banerjee, A. 2019. Materials Modelling for Energy Harvesting. From Conversion to Application through Storage. *Digital Comprehensive Summaries of Uppsala Dissertations from the Faculty of Science and Technology* 1760. 96 pp. Uppsala: Acta Universitatis Upsaliensis. ISBN 978-91-513-0544-8.

In this Ph.D. thesis, ab initio density functional theory along with molecular dynamics and global optimization methods are used to unveil and understand the structures and properties of energy relevant materials. In this connection, the following applications are considered: i. electrocatalyst for solar fuel production through water splitting, ii. hybrid perovskite solar cell for generation of electrical energy and iii. Battery materials to store the electrical energy. The water splitting mechanism in terms of hydrogen evolution and oxygen evolution reactions (HER and OER) on the catalytic surfaces has been envisaged based on the free energy diagram, named reaction coordinate, of the reaction intermediates. The Ti-functionalized two-dimensional (2D) borophene monolayer has been emerged as a promising material for HER and OER mechanisms as compared to the pristine borophene sheet. Further investigation in the series of this noble metal free monolayer catalyst is 2D Al_2C monolayer both in form of pristine and functionalized with nitrogen (N), phosphorous (P), boron (B), and sulphur (S). It has been observed that only B substituted Al_2C shows very close to thermoneutral, that could be the most promising candidate for HER on functionalized Al_2C monolayer. The adsorption of O^* intermediate is stronger in S-substituted Al_2C , whereas it is less strongly adsorbed on N-substituted Al_2C . The subsequent consideration is being the case of n-type doping (W) along with Ti codoped in BiVO_4 to enhance the efficiency of BiVO_4 photoanode for water splitting. The determined adsorption energy and corresponding Gibbs free energies depict that the Ti site is energetically more favorable for water splitting. Moreover, the Ti site possesses a lower overpotential in the W–Ti codoped sample as compared to the mono-W doped sample. We have also explored the effect of mixed cation and mixed anion substitution in the hybrid perovskite in terms of structural stability, electronic properties and optical response of hybrid perovskite crystal structures. It has been found that the insertion of bromine (Br) into the system could modulate the stability of the Guanidinium lead iodide (GAPbI_3) hybrid perovskite. Moreover, the band gap of the mixed hybrid perovskite is increased with the inclusion of smaller Br anion while replacing partially the larger iodine (I) anion. Finally the electrochemical storage mechanism for Sodium (Na) and lithium (Li) ion insertion has been envisaged in inorganic electrode (eldfellite, $\text{NaFe}(\text{SO}_4)_2$) as well as in more sustainable organic electrode (di-lithium terephthalate, Li_2TP). The full desodiation capability of the eldfellite enhances the capacity while the activation energies (higher than 1 eV) for the Na^+ ion diffusion for the charged state lower the ionic insertion rate. The key factor as the variation of Li-O coordination in the terephthalate, for the disproportionation redox reaction in Li_2TP is also identified.

Keywords: Materials Modelling, DFT, Energy Materials, Photocatalysis, HER and OER, Hybrid Perovskite Solar Cells, Stability, Thermodynamics and Kinetics in Na-ion battery, Organic Crystal Battery

Amitava Banerjee, Department of Physics and Astronomy, Materials Theory, Box 516, Uppsala University, SE-751 20 Uppsala, Sweden.

© Amitava Banerjee 2019

ISSN 1651-6214

ISBN 978-91-513-0544-8

urn:nbn:se:uu:diva-369695 (<http://urn.kb.se/resolve?urn=urn:nbn:se:uu:diva-369695>)

Dedicated to my parents

List of papers

This thesis is based on the following papers, which are referred to in the text by their Roman numerals.

- I **Scrupulous Probing of Bifunctional Catalytic Activity of Borophene Monolayer: Mapping Reaction Coordinate with Charge Transfer**
A Banerjee, S Chakraborty, NK Jena, R Ahuja
ACS Applied Energy Materials, 2018, 1 (8), 3571-3576

- II **Theoretical Evidence behind Bifunctional Catalytic Activity in Pristine and Functionalized Al₂C Monolayers**
R Almeida, A Banerjee, S Chakraborty, J Almeida, and R Ahuja
ChemPhysChem, 2018, 19 (1), 148-152

- III **Simultaneous enhancement in charge separation and onset potential for water oxidation in a BiVO₄ photoanode by W–Ti codoping**
X Zhao, J Hu, B Wu, A Banerjee, S Chakraborty, J Feng, Z Zhao, S Chen, R Ahuja, T C Sum, and Z Chen
Journal of Materials Chemistry A, 2018, 6 (35), 16965-16974

- IV **Bromination-induced stability enhancement with a multivalley optical response signature in guanidinium [C(NH₂)₃]⁺-based hybrid perovskite solar cells**
A Banerjee, S Chakraborty, and R Ahuja
Journal of Materials Chemistry A, 2017, 5 (35), 18561-18568

- V **Rashba Triggered Electronic and Optical Properties in De Novo Designed Mixed Halide Hybrid Perovskites**
A Banerjee, S Chakraborty, and R Ahuja
Submitted

- VI **Cesium bismuth iodide, Cs_xBi_yI_z, solar cell compounds from systematic molar ratio variation**
M. B. Johansson, B. Philippe, A Banerjee, D. Phuyal, S. Chakraborty, M. Cameau, H. Zhu, R. Ahuja, G. Boschloo, H. Rensmo and E. M. J. Johansson
Submitted

- VII **Unveiling the thermodynamic and kinetic properties of $\text{Na}_x\text{Fe}(\text{SO}_4)_2$ ($x = 0-2$): toward a high-capacity and low-cost cathode material**
A Banerjee, RB Araujo, and R Ahuja
Journal of Materials Chemistry A, 2016, 4 (46), 17960-17969
- VIII **Designing strategies to tune reduction potential of organic molecules for sustainable high capacity battery application**
RB Araujo, *A Banerjee*, P Panigrahi, L Yang, M Strømme, M Sjödín, C M Araujo, and Rajeev Ahuja
Journal of Materials Chemistry A, 2017, 5 (9), 4430-4454
- IX **Assessing the electrochemical properties of polypyridine and polythiophene for prospective applications in sustainable organic batteries**
RB Araujo, *A Banerjee*, P Panigrahi, L Yang, M Sjödín, M Strømme, C M Araujo, and R Ahuja
Physical Chemistry Chemical Physics, 2017, 19 (4), 3307-3314
- X **Divulging the Hidden Capacity and Sodiation Kinetics of $\text{Na}_x\text{C}_6\text{Cl}_4\text{O}_2$: A High Voltage Organic Cathode for Sodium Rechargeable Batteries**
RB Araujo, *A Banerjee*, and R Ahuja
The Journal of Physical Chemistry C, 2017, 121 (26), 14027-14036
- XI **Identifying the tuning key of disproportionation redox reaction in terephthalate: A Li-based anode for sustainable organic batteries**
A Banerjee, RB Araujo, M Sjödín, and R Ahuja
Nano Energy, 2018, 47, 301-308

Reprints were made with permission from the respective publishers.

Comments on my own contribution:

For all of my first author articles, I have done calculation, analysed data, drawn figures, and wrote either part of the manuscript or full manuscript. First authorship is shared in article II and VIII. Articles III, VI, VIII, IX are the outcomes of experiment-theory joint collaboration. In these articles, I have done part of the calculations and wrote theoretical portion of the manuscript.

List of papers not included in thesis

Articles which are co-authored by me but not included in the thesis.

- I **Hydrogen storage materials for mobile and stationary applications: current state of the art**
Q Lai, M Paskevicius, DA Sheppard, CE Buckley, AW Thornton, MR Hill, Q Gu, J Mao, Z Huang, H K Liu, Z Guo, A Banerjee, S Chakraborty, R Ahuja, KF Aguey Zinsou
ChemSusChem, 2015, 8 (17), 2789-2825
- II **Static and Dynamical Properties of heavy actinide Monopnictides of Lutetium**
SH Mir, PC Jha, MS Islam, A Banerjee, W Luo, SD Dabhi, PK Jha, and R Ahuja
Scientific reports, 2016, 6, 29309
- III **Sensitive and selective detection of copper ions using low cost nitrogen doped carbon quantum dots as a fluorescent sensing platform**
V Singh, V Kumar, U Yadav, RK Srivastava, VN Singh, A Banerjee, S Chakraborty, AK Shukla, DK Misra, R Ahuja, A Srivastava, P S Saxena
ISSS Journal of Micro and Smart Systems, 2017, 6 (2), 109-117
- IV **Valence Level Character in a Mixed Perovskite Material and Determination of the Valence Band Maximum from Photoelectron Spectroscopy: Variation with Photon Energy**
B Philippe, TJ Jacobsson, JP Correa-Baena, NK Jena, A Banerjee, S Chakraborty, U B Cappel, R Ahuja, A Hagfeldt, M Odelius, H Rensmo
The Journal of Physical Chemistry C, 2017, 121 (48), 26655-26666
- V **Current computational trends in polyanionic cathode materials for Li and Na batteries**
S Chakraborty, A Banerjee, T Watcharatharapong, RB Araujo, and R Ahuja
Journal of Physics: Condensed Matter, 2018, 30 (28), 283003
- VI **Silver substrate effect on the enhancement of HER activity of 2D B₂C sheet**

A Banerjee, J Wärnå, S Chakraborty, and R Ahuja
in manuscript

VII Band alignment through functionalisation of Mg_3N_2 to enhance the HER activity

A Banerjee, J Wärnå, S Chakraborty, and R Ahuja
in manuscript

VIII Theoretical investigation of HER micro-kinetics on Mg_3N_2 surface

J Wärnå, A Banerjee, S Chakraborty, and R Ahuja
in manuscript

IX Relation of Na-O coordination chemistry to the redox potential of organic batteries: An aspect of crystal structure evolution

A Banerjee, RB Araujo, and R Ahuja
in manuscript

X Tuning the energetics of intermediates of water electrolysis at iron-doped nickel oxide

Z. Qiu, A Banerjee, Y. Ma, S. Chakraborty, R. Ahuja, T. Edvinsson
in manuscript

Contents

| | |
|---|----|
| Part I: Introduction & Theoretical formalism | 11 |
| 1 Introduction | 13 |
| 2 Theoretical Methods | 21 |
| 2.1 The Many body problem | 21 |
| 2.2 Density Functional Theory | 23 |
| 2.2.1 Hohenberg-Kohn theorems | 23 |
| 2.2.2 Kohn-Sham formalism | 25 |
| 2.3 Exchange-Correlation approximation | 26 |
| 2.3.1 Local density approximation | 27 |
| 2.3.2 Generalised-Gradient approximation | 28 |
| 2.3.3 Hybrid Exchange-Correlation functional | 28 |
| 2.3.4 Van der Walls interaction | 29 |
| 2.4 Computational Methods | 30 |
| 2.4.1 Basis Set | 30 |
| 2.4.2 Periodic System: Bloch Electrons | 31 |
| 2.4.3 Pseudopotential | 32 |
| 2.4.4 Projected Augmented Wave method | 35 |
| 2.4.5 Hellmann-Feynman Force Theorem | 38 |
| 2.4.6 Crystal Structure Prediction: Constrained Evolutionary Algorithm | 38 |
| Part II: Energy Production | 43 |
| 3 Probing Hydrogen and Oxygen Evolution Reaction Mechanism | 45 |
| 3.1 Hydrogen Evolution Reaction | 46 |
| 3.2 Oxygen Evolution Reaction | 47 |
| 3.3 2D ultra-thin catalyst | 48 |
| 3.3.1 Probing of bifunctional catalytic activity of borophene monolayer | 48 |
| 3.3.2 Catalytic activity in pristine and functionalized Al_2C monolayers | 50 |
| 3.4 Metal Oxide photocatalyst | 53 |
| 3.4.1 Water oxidation in BiVO_4 photoanode by W-Ti codoping | 53 |

| | | |
|--------------------------------|--|----|
| 4 | Electronic and Optical Properties of Stable Mixed Hybrid Perovskite Solar Cells | 56 |
| 4.1 | Bromine induced thermodynamic stability in mixed-halide perovskite | 57 |
| 4.2 | Electronic structure and optical response of mixed cation-mixed anion based Hybrid Perovskites | 59 |
| Part III: Energy Storage | | 63 |
| 5 | Thermodynamics and Kinetics of Battery Materials | 65 |
| 5.1 | Thermodynamics of Ion Insertion in the Electrodes | 65 |
| 5.1.1 | Thermodynamics of Na insertion in $\text{Na}_x\text{Fe}(\text{SO}_4)_2$ | 68 |
| 5.1.2 | Ion insertion potential and capacity of organic cathode: chloranil | 70 |
| 5.1.3 | Thermodynamics of Li-based organic anode: Terephthalate | 74 |
| 5.2 | Diffusion kinetics of the guest ion | 76 |
| 5.2.1 | Ionic diffusion in $\text{Na}_x\text{Fe}(\text{SO}_4)_2$ | 77 |
| 6 | Summary and Future Outlook | 80 |
| 7 | Svensk sammanfattning | 83 |
| 8 | Acknowledgments | 86 |
| References | | 87 |

Part I:
Introduction & Theoretical formalism

1. Introduction

The evolution of human civilization has been strongly dependent on energy consumption ever since the stone age, which has made the energy demand a metonymy for the basic needs. This energy could be classified as “Non-Renewable” and “Renewable” based on the associated resources. The non-renewable energy sources, viz. coal, oil, and natural gas are most widely utilized due to their historical abundance and easy commercialization, as well as due to the world economic and geo-political dependencies. However, it has been found that these resources could not be able to satisfy the huge energy demand that taking into account the population growth and the high living standard. It is well known that the end product of fossil fuel (coal, oil and natural gas) is mostly CO_2 , the main component of green house gas, which is the most dangerous and alarming factor behind the global warming. It has been reported that the global emission of CO_2 in 2010 is 30.4 Gt (gatonnes), which has been projected to be 43.3 Gt in 2035 [1] based on the current scenario. This impacts the environment drastically. For instance, a recent report from World Bank [2] expressed the impact of climate change in near future on various famous sea-cities. It has been reported that almost 40% of the Bangkok (the capital of Thailand) will be inundated by seawater near 2030 due to extreme climate change, heavy rainfall and rise in sea level. So the emissions of green house gases, the prime reason of global warming, is a serious threat for human civilization. Not only the emissions of green house gasses, even the resources of fossil fuel are spontaneously diminishing. According to Topal et. al. after 2042, the coal will be the only fossil fuel in the earth, while there will be no-more fossil fuel after 2112 [3]. However, the drastic increase in world population claims more and more energy demand, e.g. even within 2009 to 2035, the energy demand will increase from 12 to 18 billion ton oil equivalent [1, 2]. Therefore it is envisioned that to save the human civilization, the non-renewable energy technology based on fossil fuel should be replaced by the sustainable energy technology, which could be cheaper enough compared to the fossil fuel.

At present, the most promising candidate for the eco-friendly energy source is solar energy with solar synthetic fuel as the prolific energy carrier. This green energy production together with the sustainable energy storage technologies would make the sustainable *green energy cycle* (see Figure 1.1). All these factors motivate this thesis’s work, which will be mainly focused on solar energy and hydrogen as the energy carrier, which originates from hydrogen evolution reaction (HER) along with inorganic and organic-green batteries in order to store the produced energy.

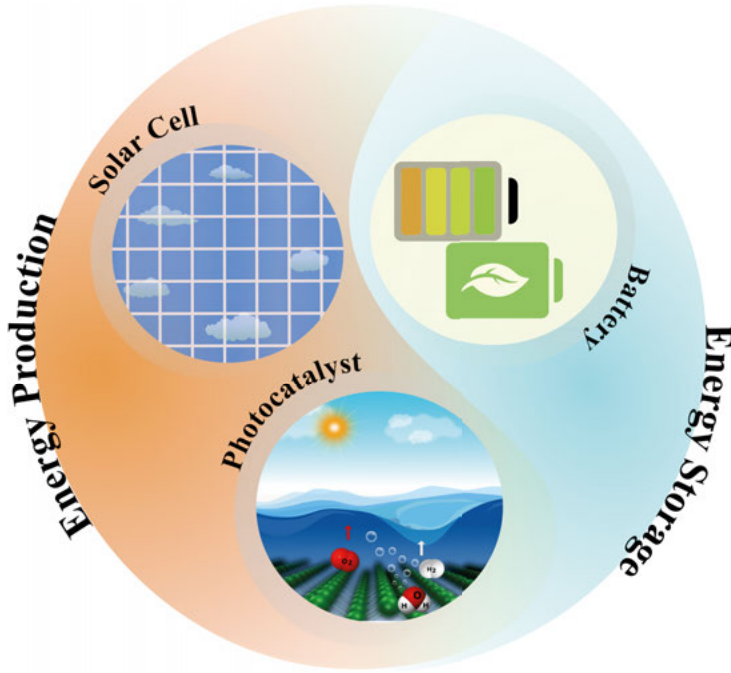


Figure 1.1. Schematic of Sustainable Green Energy Cycle

Solar energy is one of the tangible most futuristic energy in the quest for clean energy resource in the world. Every second, 340 J/m^2 of the solar electromagnetic radiation penetrates the Earth's outer atmosphere. Now, if we consider only half of the Earth surface as the illuminated area, then the incoming radiation could correspond to the energy of around 416000 TW, despite the fact that $\sim 52\%$ of this radiation is reflected back [4]. This much energy is 20000 times higher than the total power consumption of the human population, which is estimated to be $\sim 17.5 \text{ TW}$ [5, 6]. The main problem is the effective conversion of solar power to more convenient electrical energy for the use in daily life. This paves the way to the research area of photovoltaic cell (Solar Cell), which could directly convert solar energy into electrical energy without any negative impact on the environment. The conventional solar cell consists of a p-n junction. In this case the photon with the associated energy comparable to the band gap of the semiconductor incidents on the junction, subsequently the charge carriers, i.e. electrons and holes are generated and getting separated. The charge carriers accumulated at the respective electrode create the potential difference across the junction. At present, the most actively studied photovoltaics, hybrid perovskite solar cell consists of p-i-n junction [7], where the perovskite active layer plays the absorber role between hole transport (HT) or p-layer and electron transport (ET) or n-layer. The built-in potential in between HT and ET layer induces built-in electric field within the i-layer. This

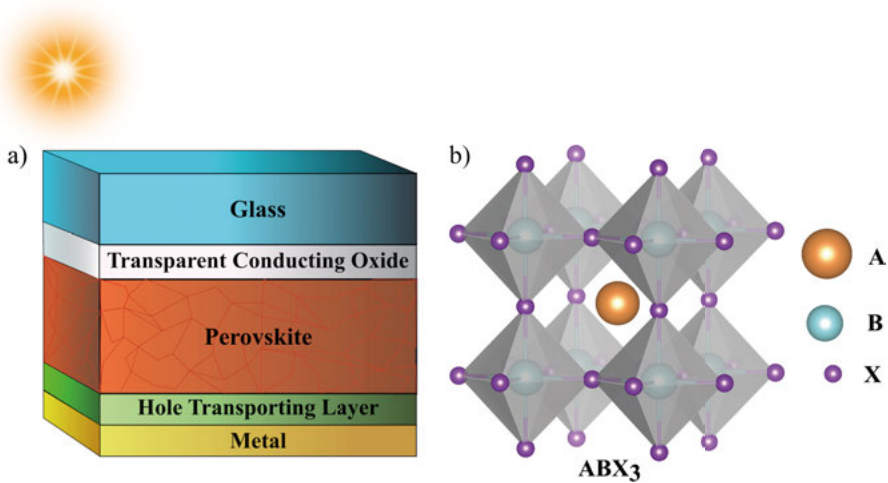


Figure 1.2. a) Schematic view of the perovskite solar cell configuration, b) Crystal structure of a ABX_3 type perovskite.

field separates the photon generated electron-hole pairs, and directs the hole to the HT layer and electron to the ET layer. The ET and HT layer respectively extracts consequently the electron and hole at the cathode and anode of the photovoltaic cell. It is noteworthy to mention that this ET and HT layer should attain appropriate position in the energy level diagram so that it could selectively extract the charge carriers from the perovskite layer. Eventually, the work function difference between HT and ET layer triggers to move off the charge carrier in opposite direction. However, perovskite solar cells without the HT layer have been reported recently [8, 9]. The first solar cell was made from silicon in 1940 by Russel Ohl, after the discovery of photovoltaic in 1839 by Alexandre [10]. Since then several decades have been dedicated to the research activities and technological advancement to develop highly efficient and cost effective solar cell using various kind of materials [11, 12]. Based on this background, the photovoltaic solar cell could be categorized as 1) first generation solar cell, 2) second generation solar cell and 3) third generation solar cell [13]. The first generation solar cells are mainly the wafer based mono-crystalline and polycrystalline silicon, which are commercially most viable technology. The second generation solar cell includes thin film based amorphous silicon, CdTe and CIGS. The third generation solar cells are based on nano crystal (quantum dot), polymer, dye sensitizer, and hybrid perovskite materials. Among the third generation solar cells, the most emerging photovoltaic is based on hybrid perovskite. Despite their efficiency and stability issues, the perovskite solar cells hold the advantage over the traditional silicon solar cells, due to its simplicity in processing. For instance, the traditional silicon solar cells consist of multistep high temperature ($\sim 1000^\circ\text{C}$) pro-

cess and high vacuum technology, which increase the large scale production cost, whereas hybrid perovskite involves simple wet chemistry and solution processing [13]. Within the past few years, perovskite solar cells have shown exciting development in this field. In the early 19th century, this perovskite mineral was discovered and named after the Russian mineralogist Lev Perovski [14]. Subsequently, Victor Goldschmidt analyzed their crystal structure and classified this family of minerals in ABX_3 form (where, A and B are two types of cation and X is the anion) as shown in Figure 1.2 [15]. In 2009 Kojima *et. al.* first reported hydrid perovskite based sensitized solar cell with a liquid electrolyte of power conversion efficiency of 3.8% [16]. However, the stability of this kind of solar cells was not good because of the dissolving tendency of perovskite material in the liquid electrolyte [17]. Later on, in 2012, all solid state solar cell of efficiency of 9.7% and 10.9% were fabricated to overcome the stability issues of electrolyte [18, 19]. Afterwords, with several scientific advancement and breakthroughs in the solar-to-electricity power conversion efficiencies [11], hydrid perovskite solar cell achieved the certified efficiency of 22.7% in 2017 [20, 21]. It is important to highlight that the efficiency of the perovskite solar cells are comparable to polycrystalline Si solar cells (22.3%), CIGS (22.6%), CdTe solar cell (22.1%) and approaching very close to recent record of Si solar cell of 26.6% [22, 23]. In the effort of this development of experimental processing technique, theoretical modeling of perovskite could shorten trial and error process and provide more theoretical insight of the solar cell mechanism. Many theoretical approaches have been prescribed to tune the chemical composition, band gap and the absorption intensity of the material [24–26]. The exciton binding energy and its stability could also be predicted through electronic structure calculation. Recently, density functional theory has been used to address the most rising topic, i.e. moisture stability of this hybrid perovskites [27]. This thesis therefor focuses on the theoretical prediction of electronic and optical properties of perovskite with the compositional variation, as well as the chemical and structural stability.

In the quest for clean energy source, hydrogen is the most well-known energy vector. The reasons behind the potentiality of hydrogen are: i) highest energy per mass ratio among all the chemical fuels, ii) most earth abundancy, and iii) after burning in fuel cell the byproduct is water. In spite of such potential relevances, there are several issues need to be tackled to make this technology economically viable. One of the major problems is mass production of low cost hydrogen which is generally formed in organic molecule and water resources. Many strategies have been proposed, like thermochemical conversation of biomass, gasification, biofuel reforming, high temperature electrocatalysis, although they are advantageous in terms of exergy efficiency, but those are just another way of fossil fuel consumption [28]. Among all the explored strategies, the most promising one is water splitting in presence of solar irradiation, which is most environmentally benign and cost-effective process [28]. Therefore, increase in both energy and exergy efficiencies of solar-based

water splitting could make the hydrogen production a more sustainable choice. In this regard, photocatalyst is immensely important to catalyze the water splitting process. The mechanism of photocatalytic water splitting is divided into

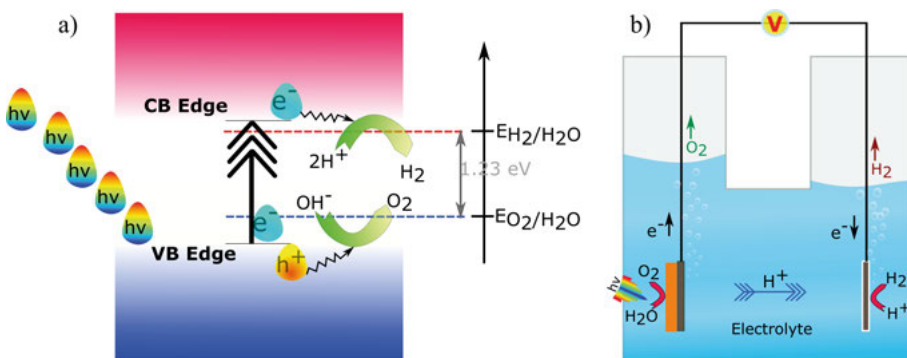


Figure 1.3. a) Mechanism of photocatalytic water splitting, b) Schematic of photo-electrochemical cell

the following 4 stages : I) photon with energy equal or higher than the band gap excites the semiconductor upon incident, II) subsequently electron moves from valance band (VB) to conduction band (CB), III) the separated electrons and holes move to the surface of the electrode, and IV) the reduction and oxidation of adsorbed reactants to generate H_2 and O_2 respectively at CB and VB edges as shown in Figure 1.3. The efficiency of the hydrogen evolution reaction (HER) and oxygen evolution reaction (OER) depends on the distance of CB and VB edge towards the HER and OER potential respectively. In 1972, Fujishima and Honda first discovered the photocatalytic process in photo-electrochemical cell (PEC). The main difference with the previously described mechanism (as shown in Figure 1.3) is that, here the photo-generated electrons from photo-anode are transferred through the external circuit towards the photo-cathode and simultaneously H^+ moves through the electrolyte towards the photo-cathode. There have been a quite a large number of investigations regarding various semiconductor materials have been reported as promising photocatalyst [29–38]. Among them, the most propitious is TiO_2 due to its abundance nature along with non-corrosiveness, eco-friendliness, and structural stability. One of the drawback of this material is the corresponding large UV-active band gap of 3.2 eV. The UV light is only 4% of the total incoming solar radiation on the surface, whereas the visible light contributes almost 50%. Therefore, it is preferable to perform band gap tuning of TiO_2 and other photocatalyst material to make them more photoactive. In this circumstance, the theoretical modeling based on the electronic structure calculations is most effective way to tune the band gap, either through searching appropriate dopant or by doing structural modification. In addition to the band gap, another crucial feature in the photocatalytic phenomena is the binding mechanism of the reactant to the surface. From the adsorption energy, it is possible to predict the

trend in the exchange current density, micro-kinetics and hence could suggest the optimum possible catalyst for HER and OER [39, 40]. Using state-of-the-art DFT calculations, this thesis has been focussed on the dopant effect along with the reactant binding energy, adsorption free energy and over potential of the redox reaction (HER & OER) to generate H_2 and O_2 .

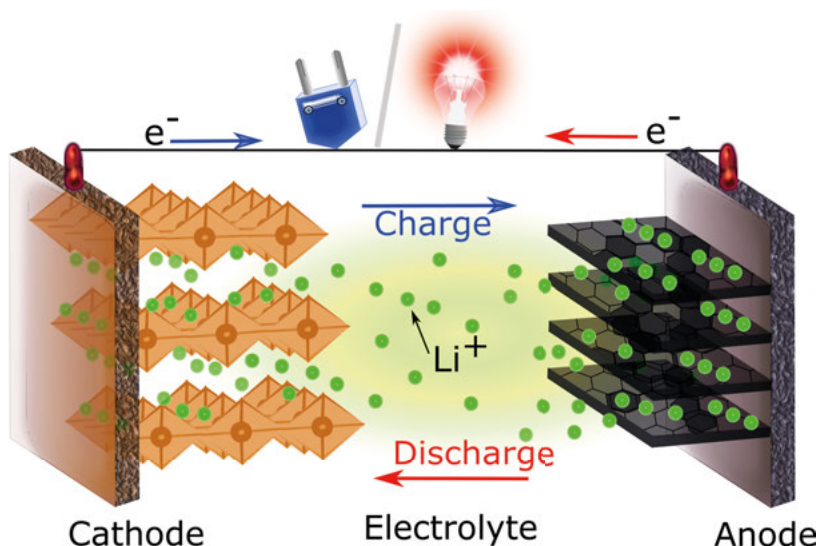


Figure 1.4. Schematic of Li-ion battery mechanism

Along with the quest for renewable energy production, the energy storage technology is equally important to make the sustainable green energy cycle feasible. Since it is quite natural to have the sunlight through out the year with variable intensity, this will not generate the similar amount of energy all the time. Even in absence of sunlight, the solar cell will not be able to produce any electricity. Therefore, it is required to store the energy in some form of devices. In this perspective, battery technology could resolve this issue by storing and subsequently supplying the electrical energy on demand. Since the first commercialization of rechargeable Li ion battery (LIB) technology in 1991, it has been the most promising candidate for portable storage devices [41]. LIB technology dominates the portable electronic markets due to its inherent lightweight, durability, high energy density and high rate of storage capability as compared to the other currently used electrochemical storage device [42]. The working principle of this electrochemical device has been depicted in Fig.3, which is considering $LiCoO_2$ as cathode and graphite as the anode material. In the charging process, the Li^+ ions which have been released from the cathode and intercalate into the anode, whereas in the discharging process (during the application of the device), the intercalated Li ions again reside on the cathode. During this redox process, Li^+ ions migrate through the electrolyte and simultaneously the released electron circulates through the exter-

nal circuit to maintain the charge neutrality of the electrodes. However, with the great success of LIB technology, it still carries some concern like the geographical abundance of lithium. Moreover, the LIB is not appropriate solution for all-electric vehicle and in power grid, where the gravimetric energy density is not important. To overcome the aforementioned bottleneck, another alkali metal next to lithium, sodium could be a promising replacement. Since the abundance of sodium is more than the lithium, being the sixth most abundant element in the earth crust, and hence could reduce the production cost as well as device cost of SIB technology, where the gravimetric density is not the most concerned criteria. Over the past several years many Li based electrode, as cathodes, like layered (LiCoO_2 , $\text{LiNi}_{0.33}\text{Mn}_{0.33}\text{Co}_{0.33}\text{O}_2$), spinel (LiMn_2O_4), olivine (LiFePO_4), tavorite (LiFeSO_4F); and as anodes, like graphite, Si, Ge, Sn, $\text{Li}_4\text{Ti}_5\text{O}_{12}$ have been studied [43–45]. Similarly, Na based cathodes such as $\text{Na}_{\frac{2}{3}}\text{Ni}_{\frac{1}{3}}\text{Mn}_{\frac{2}{3}}\text{O}_2$, $\text{NaNi}_{0.5}\text{Mn}_{0.5}\text{O}_2$, $\text{Na}_2\text{FePO}_4\text{F}$ and Na based efficient anodes such as NaSi, NaGe, $\text{Na}_{15}\text{Sn}_4$, $\text{Na}_{15}\text{Pb}_4$, and Na_3Sb have been explored [43–45]. In addition to the arduous search for inorganic electrode materials, the scientific community has rejuvenated the research on organic battery in past few years. This may be due to the elemental abundance, inexpensive-ness, environmentally more benign synthetic process and easy to tailor the redox potential of interest. In the conventional inorganic alkali metal battery, the charging/discharging mechanism involves intercalation of alkali metal ion, which is occurred by the lattice transformation or change in inter-layer distance. The drastic effect of this is slow kinetics and heat generation during the process. However, the electrochemical process in organic electrode is mainly governed by its inherent flexibility and the correspondingly straightforward redox reaction. This essentially makes the redox process faster and hence could provide the excellent rate performance along with long cycle life. Moreover, the energy extensive synthesis process and possibility to extract the organic raw material from the biomass, make the organic battery technology most viable choice for green battery. Almost five decades ago, in 1969, the dichloroisocyanuric acid was recognized as a first organic cathode material of a high open circuit voltage of 4 V, having self-discharge and anode passivation problem [46]. Since then several organic small molecules, such as quinones, anhydrides, and doped conjugated polymers have been investigated as the organic cathodes due to their high theoretical capacity and fast electrochemical process [47, 48]. Among them, poly (aniline) and poly (pyrrole) are also commercialized by BASF and Bridgestone-Seiko [47, 49]. However, the research on organic materials have been dimmed out due to the discovery of intercalated inorganic transition metal cathode with high open circuit voltage in the order of 5 V with respect to Li/Li^+ . However it is worth to mention that the organic battery technology also possess a number of drawbacks, such as poor electrical conductivity, high solubility within the electrolyte, dopant dependent potential, low energy densities due to the actual low delivered potential. To overcome

these drawbacks, it has been proposed to use redox active pendant group with the polymer backbone chain. On the basis of this idea, Nakahara *et. al.* first proposed the organic battery with discharge voltage of 3.5 V with 70% theoretical capacity [50]. Subsequently, many studies have been focussed on this issue to resolve using quinone and terephthalate based molecule [51–55]. This quest is still ongoing in order to achieve a voltage as well as high capacity and low cost rechargeable battery for portable as well as stationary applications.

From the above mentioned research area, it has been realized that solar cell technology, hydrogen evolution through water splitting and the battery technology to store the energy are all needed in order to have a complete circle of energy applications in daily life. The prime issues to mostly care about those technologies are scalability, cost-effectiveness. Hence, the technology needs to be much smaller, faster, effective, at the same time should be as cheap as the fossil fuel technologies. In this scenario importance of material science could be manifested since the main concerns, in the energy production and storage are innately correlated with the materials properties. In this thesis, the *ab-initio* approach to the material science has been used to investigate and predict the crystal structures, electronic properties, chemical reactions related to the energy application. Keeping all these considerations in nutshell, the outline of the thesis is as follows: background of the theoretical methods used to investigate is discussed in Chapter 2; case specific applications are deliberated in Chapter 3 for hybrid perovskite solar cell, Chapter 4 for water splitting (HER-OER reaction) and Chapter 5, the thermodynamics and kinetics of organic and inorganic battery electrodes. All the chapters are connected with the basic motivation of energy.

2. Theoretical Methods

The chapter is focussed on the theoretical framework, which has been used throughout the studies in this thesis. The discussion in the chapter starts from the foundation of many-body problem, which is subsequently followed by the density functional theory and its implementation. The basic concepts of crystal structure prediction with constrained evolutionary algorithm is depicted at the end of this chapter.

2.1 The Many body problem

The determination of the electronic structure of materials is intertwined with the prediction of their inherent properties. Electrons in a material are quantum mechanically correlated, which brings further complexity to describe an electron within the system with large number of electrons. This problem is referred as quantum-mechanical “many-body problem”.

In most of the quantum chemical approaches, including the cases, studied here, the uttermost goal is to approximate the solution of the non-relativistic time-independent Schrödinger equation:

$$\hat{H}\Psi_i(\mathbf{x}_1, \mathbf{x}_2, \dots, \mathbf{x}_N, \mathbf{R}_1, \mathbf{R}_2, \dots, \mathbf{R}_M) = E_i\Psi_i(\mathbf{x}_1, \mathbf{x}_2, \dots, \mathbf{x}_N, \mathbf{R}_1, \mathbf{R}_2, \dots, \mathbf{R}_M), \quad (2.1)$$

where Ψ_i is the wave function of the i^{th} state of the quantum mechanical system, which depends on \mathbf{x}_i , that is a collective term of the $3N$ spatial r_i and N spin coordinates of the electrons and the $3M$ spatial coordinates of the nuclei, \mathbf{R}_I . The energy of the corresponding state is represented by E_i . \hat{H} is the Hamilton operator for the system consisting of M nuclei and N electrons, considering there spatial coordinate only, which has the following form:

$$\begin{aligned} \hat{H} = & -\frac{1}{2} \sum_i^N \nabla_i^2 - \sum_k^M \frac{1}{2M_k} \nabla_k^2 - \sum_i^N \sum_k^M \frac{Z_k e^2}{|\mathbf{r}_i - \mathbf{R}_k|} \\ & + \sum_i^N \sum_{j>i}^N \frac{e^2}{|\mathbf{r}_i - \mathbf{r}_j|} + \sum_k^M \sum_{l>k}^M \frac{Z_k Z_l e^2}{|\mathbf{R}_k - \mathbf{R}_l|}, \end{aligned} \quad (2.2)$$

where, M_k are mass of representative k^{th} nuclei, respectively. Z_k and Z_l are the atomic number of respective k^{th} and l^{th} nuclei. The first two terms in the Eq. (2.2) respectively represents the kinetic energy of the system consisting of all N

electrons and M nuclei. The remaining three terms constitute the potential part of the Hamiltonian, where the 3rd, 4th and 5th term are associated with the Coulomb interaction between electrons-nuclei, electron-electron and nuclei-nuclei.

In order to determine the ground state properties of the system, we need to solve the Schrödinger equation, which is possible to solve exactly only for one electron-nuclei system, without analytical complexity. However as one mole of solid contains $\sim 10^{23}$ electrons, hence corresponding many-body wave functions increase the complication to solve the equation exactly. This will certainly imply one has to simplify the problem.

The Schrödinger equation could be simplified by considering the approximation of lighter electrons motion with the field of fixed and rather heavier nuclei. Consequence of that, decouples the electron and nuclear wave function, in fact the nuclear coordinates don't explicitly appear in electron wave function, ψ_{elec} . This approximation is notified as Born-Oppenheimer approximation [56]. The constrained of nuclei motion nullifies the kinetic energy of nuclei and the total energy of the system could be defined as the sum of E_e and a constant nuclei-nuclei repulsive term. Therefore, the Hamiltonian in Eq. (2.2) will be reduced to only electronic Hamiltonian

$$\hat{H}_e = -\frac{1}{2} \sum_i^N \nabla_i^2 - \sum_i^N \sum_k^M \frac{Z_k e^2}{|\mathbf{r}_i - \mathbf{R}_k|} + \sum_i^N \sum_{j>i}^N \frac{e^2}{|\mathbf{r}_i - \mathbf{r}_j|}. \quad (2.3)$$

Consequently, the Schrödinger equation, Eq. (2.2) can be formulated in the form of

$$\hat{H}_e \Psi_{elec} = E_e \Psi_{elec}. \quad (2.4)$$

The 2nd term of \hat{H}_e , i.e. Coulomb attractive term could be seen as an external potential, which does not need to be limited up to the nuclear field. In order to obtain the properties of any quantum mechanical system, we need to solve a simplified form of the Schrödinger equation, Eq. (2.4). However, still it is practically intractable, mainly due to the 3rd term of the \hat{H}_e in Eq. (2.3), the electron-electron repulsive term and also the complexity of many-electron wave function. Therefore, we need further approximation to solve the many electron problem. For doing this, many methods have been developed in last decades, viz. Hartree-Fock and density functional theory. The present thesis will discuss the density functional theory, which has extensively been utilized in the studies. The Hartree-Fock formalism is a wave function based approach (having $4N$ variables for each N electrons). It neglects the Coulomb correlation, which will increase the complexity with large number of electrons in the system [57, 58]. In contrast, the electron density, a three variable object (along three cartesian directions) is used in density functional theory (DFT) to solve the Schrödinger equation, as discussed in the subsequent section.

2.2 Density Functional Theory

Before discussing the formalism of density functional theory, let us look on the various aspect of electron density $\rho(\mathbf{r})$. First of all, unlike the wave function, electron density is a measurable quantity. Being an observable, the electron density could provide comparable realistic view of the system. By integrating it over a specified volume, the total number of electron will be expressed as follows:

$$\int \rho(\mathbf{r})d\mathbf{r} = N. \quad (2.5)$$

The $\rho(\mathbf{r})$ shows its maximum value at the position of nuclei, \mathbf{R}_I , owing to the attractive forces of nuclei. The density gradient at this position is discontinuous and forms a cusp. The density at the position of nucleus provides the information of nuclear charge.

The electron density as a variable rather than the many-body wave function has been proposed first time by Thomas and Fermi [59, 60]. The central idea of this model is expressing kinetic energy in terms of non-interacting uniform electron density. However, the electron-electron repulsive and electron-nuclei attractive interactions are treated classically. Inefficiency of this model lays on the coarse approximation of the kinetic energy, due to the absence of exchange and correlation energy. These difficulties to accurately depict the many-body system remained even after incorporation of exchange energy by Dirac [61]. For example, one of the shortcomings of this model is that the energy of the molecule is higher than the summation of energy of individual atoms. Therefore, one needs to improve the DFT methods further. The Hohenberg-Kohn formulation is an improvement of DFT, which is till date successfully applied to determine the electronic structure, and hence properties of many materials.

2.2.1 Hohenberg-Kohn theorems

In 1964, Hohenberg and Kohn laid the foundation of DFT, by introducing an exact theory of interacting many-body systems [62]. It is based on the following two remarkable theorems¹:

Theorem I

For any system of interacting particles in an external potential $V_{ext}(\mathbf{r})$, the potential $V_{ext}(\mathbf{r})$ can be determined uniquely, except for a constant, by the ground state particle density $\rho_0(\mathbf{r})$

¹The statements of the two theorems are written exactly as in the book titled “Electronic Structure: Basic Theory and Practical Methods” written by Richard M. Martin.[63]

Theorem II

A universal functional for the energy $E[\rho]$ in terms of density $\rho(\mathbf{r})$ can be defined, valid for any external potential $V_{ext}(\mathbf{r})$. For any particular $V_{ext}(\mathbf{r})$, the exact ground state energy of the system is the global minimum value of this functional, and the density $\rho(\mathbf{r})$ that minimizes the functional is the exact ground state density $\rho_0(\mathbf{r})$

It could be generalized that, according to the first theorem, the energy of the ground state, E_0 is a unique functional of the electron density (as shown by the red ball in the schematic 2.1). Now, this electron density could be obtained (using the second theorem) by minimizing the energy of the functional, $E[\rho(\mathbf{r})]$ (as shown in the schematic 2.1) and the density corresponds to this lowest energy is the exact ground state density, $\rho_0(\mathbf{r})$. The first theorem also could be

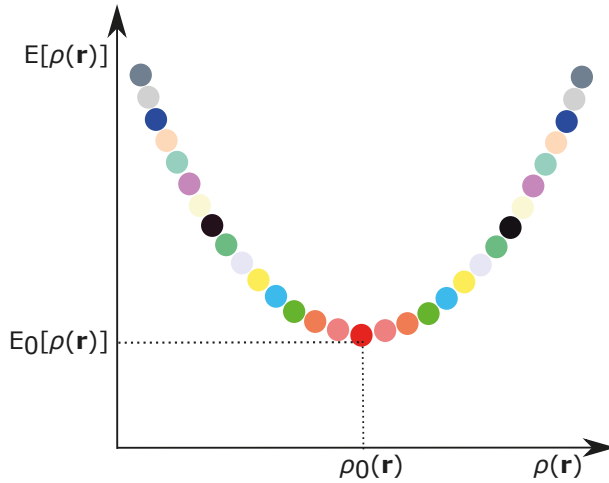


Figure 2.1. Schematic of the energy as a functional of the electron density

interpreted as follows: it is possible to reconstruct the Hamiltonian by knowing the ground-state particle density and observable quantities could be obtained as a functional of particle density as

$$\langle \Psi | A | \Psi \rangle = A[\rho(\mathbf{r})]. \quad (2.6)$$

The ground state density is sufficient to know all the properties of the system. The second theorem mostly justifies how the certain density will be the ground state density. It represents the total energy functional universality and the variational principle. According to these two theorems, for any external potential, $V_{ext}(\mathbf{r})$ the total energy of the system can be defined as

$$E[\rho(\mathbf{r})] = F[\rho(\mathbf{r})] + \int V_{ext}(\mathbf{r})\rho(\mathbf{r}) d\mathbf{r}. \quad (2.7)$$

Here, the universal functional, $F[\rho(\mathbf{r})]$ includes all the internal energies and the kinetic energy of the interacting system, which has the following form

$$F[\rho(\mathbf{r})] = T[\rho(\mathbf{r})] + J[\rho(\mathbf{r})] + E_{ncl}[\rho(\mathbf{r})], \quad (2.8)$$

where 1st, 2nd and 3rd terms respectively represents the kinetic energy, the classical Coulomb interaction and the non-classical term due to self interaction, exchange, and electron correlation effects. If one knows the exact form of $F[\rho(\mathbf{r})]$, it is possible to obtain the ground state energy and corresponding density by global minimization of the energy functional, $E[\rho(\mathbf{r})]$. However, only the 2nd term in Eq. (2.8) is known and explicit form other two terms is unknown, which still keep the complexity of many electron system.

2.2.2 Kohn-Sham formalism

The Hohenberg-Kohn theorem shows the existence of a universal functional without specifying the exact form, or determination of the ground state density. The Kohn-Sham (KS) formulation provides the exact approach to obtain those mentioned above. The main idea of this is to map the kinetic energy (T) of the real many body system to the exact kinetic energy (T_S) of the non-interacting reference system, which is having the same density of the real system, so that the Hohenberg-Kohn-theorems are still valid. The non-interacting kinetic energy, T_S , using the Kohn-Sham orbital, ζ_i could be expressed as follows:

$$T_S = -\frac{1}{2} \sum_{i=1}^N \langle \zeta_i | \nabla^2 | \zeta_i \rangle. \quad (2.9)$$

Although this T_S is not exactly equal to the true kinetic energy, T of the system. The actual kinetic energy could be written as

$$T = T_S + T_C, \quad (2.10)$$

where T_C is the residual part of the true kinetic energy, that is not included in T_S . Then Eq. (2.8) of universal functional, $F[\rho(\mathbf{r})]$ could be reformed as

$$\begin{aligned} F[\rho(\mathbf{r})] &= T_S[\rho(\mathbf{r})] + J[\rho(\mathbf{r})] + T_C[\rho(\mathbf{r})] + E_{ncl}[\rho(\mathbf{r})] \\ &= T_S[\rho(\mathbf{r})] + J[\rho(\mathbf{r})] + E_{XC}[\rho(\mathbf{r})], \end{aligned} \quad (2.11)$$

where E_{XC} is called the *exchange-correlation energy*, which includes the non-classical electrostatic contribution and the residual part of the true kinetic energy. Therefore, according to this formalism, total energy functional of Eq. (2.7) could be expressed as

$$\begin{aligned} E[\rho(\mathbf{r})] &= T_S[\rho(\mathbf{r})] + \int V_{ext}(\mathbf{r})\rho(\mathbf{r})d\mathbf{r} \\ &+ \frac{1}{2} \iint \frac{\rho(\mathbf{r})\rho(\mathbf{r}_2)}{|\mathbf{r} - \mathbf{r}_2|} d\mathbf{r} d\mathbf{r}_2 + E_{XC}[\rho(\mathbf{r})]. \end{aligned} \quad (2.12)$$

The 2nd term in Eq. (2.12) is the energy contribution from electron-nuclei interaction and 3rd term is the classical Coulomb contribution. According to the second theorem of Hohenberg-Kohn, the solution of the Kohn-Sham auxiliary system could be obtained by minimizing the KS energy functional in Eq. (2.12) with respect to the density $\rho(\mathbf{r})$, which formulate the following Schrödinger-like KS equation,

$$H_{KS}(\mathbf{r})\zeta_i(\mathbf{r}) = \left[-\frac{1}{2}\nabla^2 + V_{KS}(\mathbf{r}) \right] \zeta_i(\mathbf{r}) = \varepsilon_i \zeta_i(\mathbf{r}), \quad (2.13)$$

where ε_i represents the eigenvalues and V_{KS} is the effective potential, which has the following form

$$V_{KS}(\mathbf{r}) = V_{ext}(\mathbf{r}) + V_H(\mathbf{r}) + V_{XC}(\mathbf{r}), \quad (2.14)$$

where V_{ext} is the external potential as specified in Eq. (2.7) and V_H is the Hartree potential expressed as follows :

$$V_H = \int \frac{\rho(\mathbf{r}_2)}{|\mathbf{r} - \mathbf{r}_2|} d\mathbf{r}_2. \quad (2.15)$$

Additionally V_{XC} is the potential due to exchange-correlation energy, E_{XC} , the exact form of which is unknown. So, V_{XC} could be expressed simply as the functional derivative of E_{XC} with respect to the density $\rho(\mathbf{r})$ as follows :

$$V_{XC} = \frac{\delta E_{XC}[\rho(\mathbf{r})]}{\delta \rho(\mathbf{r})}. \quad (2.16)$$

We can construct the ground state density in the following form :

$$\rho(\mathbf{r}) = \sum_{i=1}^N |\zeta_i(\mathbf{r})|^2. \quad (2.17)$$

Based on the above assumption, it is possible to obtain the effective potential, V_{KS} from Eq. (2.13). Provided that we have exact form of exchange-correlation potential, then the exact ground state density and hence the ground state energy could be extracted by self-consistently solving the single particle KS equation, Eq. (2.13). In principle, KS formalism is exact, as there are no approximations yet. It maps the fully interacting many-body system to an auxiliary non-interacting system of same density. However, in this formalism, the exact form of V_{XC} is unknown, so to solve the KS equation and to obtain the ground state energy, we need to approximate the exchange-correlation potential.

2.3 Exchange-Correlation approximation

The strength of the KS approach in DFT strongly depends on the accuracy of the chosen approximation for E_{XC} [64, 65]. Hence, to successfully implement

KS approach, the finding of better functionals is the main challenge, which would be discussed in details in the following subsections.

2.3.1 Local density approximation

The central idea of this local density approximation (LDA) model is uniform electron gas, which is although far from realistic feature with rapidly varying electron density. According to this assumption² the E_{XC} could be written as

$$E_{XC}^{LDA}[\rho(\mathbf{r})] = \int \rho(\mathbf{r}) \varepsilon_{XC}^{ueg}[\rho(\mathbf{r})] d\mathbf{r}, \quad (2.18)$$

where, $\varepsilon_{XC}^{ueg}[\rho(\mathbf{r})]$ is the *exchange-correlation* energy per electron in the uniform electron gas (*ueg*) distribution, which is further weighted by $\rho(\mathbf{r})$ to ensure the presence of electron at this position in space. The $\varepsilon_{XC}^{ueg}[\rho(\mathbf{r})]$ could be splitted into two contributing terms, exchange, ε_X , and correlation, ε_C ,

$$\varepsilon_{XC}^{ueg}[\rho(\mathbf{r})] = \varepsilon_X[\rho(\mathbf{r})] + \varepsilon_C[\rho(\mathbf{r})]. \quad (2.19)$$

The explicit form of the exchange part, ε_X , can be approximated from Hartree-Fock exchange as derived by Dirac [61],

$$\varepsilon_X[\rho(\mathbf{r})] = -\frac{3}{4} \left[\frac{3\rho(\mathbf{r})}{\pi} \right]^{\frac{1}{3}}. \quad (2.20)$$

But there is no explicit form known for the remaining term, i.e. correlation, ε_C . However, Perdew-Zunger [66] and Perdew-Wang [67] prescribed analytical expression of ε_C based on the the quantum Monte Carlo calculations by Ceperley and Alder [68] for homogeneous electron gases at various densities.

Irrespective of the simplicity of the LDA approximation, it works better for many real systems, where the density of actual systems is rarely uniform. LDA could successfully determine various molecular properties, *viz.* equilibrium structures, harmonic frequencies or charge moments [69]. However, LDA shows its poor performance at energetic context, such, bond energy, because of over binding. This over binding comes due to the centered LDA exchange hole, which is more appropriate for homogeneous molecular density rather inhomogeneous atoms density, that particularly makes the exchange energy of molecular case to be more negative, hence results could be notorious as for the binding is concerned.

²This approximation can be extended to an unrestricted version, where instead electron spin density is considered, i.e. $\rho(\mathbf{r}) = \rho_\alpha(\mathbf{r}) + \rho_\beta(\mathbf{r})$. This extended approximation, is denoted as *Local Spin-Density Approximation*, LSD, which has the similar form of Eq. (2.18) as follows:

$$E_{XC}^{LSD}[\rho(\mathbf{r})] = \int \rho(\mathbf{r}) \varepsilon_{XC}^{ueg}[\rho_\alpha(\mathbf{r}), \rho_\beta(\mathbf{r})] d\mathbf{r}.$$

2.3.2 Generalised-Gradient approximation

An improvement over the LDA is prescribed within the framework of Generalised-Gradient approximation (GGA). As the name suggests, gradient of the electron density is also considered instead of only local constant density to incorporate the effects of inhomogeneities in the considered system. According to this assumption, the *exchange-correlation* energy could be expressed as

$$E_{XC}^{GGA}[\rho(\mathbf{r})] = \int \rho(\mathbf{r}) \varepsilon_{XC}^{ueg}[\rho(\mathbf{r})] F_{XC}[\rho(\mathbf{r}), \nabla\rho(\mathbf{r})] d\mathbf{r}, \quad (2.21)$$

where, $F_{XC}[\rho(\mathbf{r}), \nabla\rho(\mathbf{r})]$ is the analytical enhancement factor, based on the reduced density gradient, $s(\mathbf{r})$ as follows:

$$s(\mathbf{r}) = \frac{|\nabla\rho(\mathbf{r})|}{\rho^{\frac{4}{3}}(\mathbf{r})}. \quad (2.22)$$

Here, $s(\mathbf{r})$ is the local inhomogeneity which is a dimensionless parameter. Unlike the LDA, there is no unique form of GGA owing to various proposed form of F_{XC} , such as Becke (B88) [70]; Perdew and Wang (PW91) [71]; Perdew, Burke, and Ernzerhof (PBE) [72]. All the investigations that have been included in this thesis are based on PBE functional.

2.3.3 Hybrid Exchange-Correlation functional

The hybrid exchange-correlation functional has improved the approximation of the *exchange-correlation* energy, over the LDA and GGA, in such a way that these are the most accurate functionals available as per the energy of the system is concerned. The central idea of these functionals are mixing the exact exchange from the Hartree-Fock into the exchange-correlation energy of explicit density functional (LDA/GGA). By incorporating the exact exchange, the self-interaction³ of GGA could be partly reduced. There are various types of Hybrid functional formalisms, such as BPW91, B3LYP etc [73–75] In this thesis, Heyd-Scuseria-Ernzerhof (HSE) [76] formalism has been used, where the form of HSE exchange-correlation functional is expressed as follows:

$$E_{XC}^{HSE} = \alpha E_X^{SR}(\eta) + (1 - \alpha) E_X^{PBE,SR}(\eta) + E_X^{PBE,LR}(\eta) + E_C^{PBE}, \quad (2.23)$$

where E_X^{SR} is the short range Hartree–Fock exact exchange functional, $E_X^{PBE,SR}(\eta)$ and $E_X^{PBE,LR}$ are respectively the short and long range parts of the PBE exchange functional, E_C^{PBE} is the PBE correlation functional. The

³It is the error due to the spurious interaction of density with itself. That is due to incomplete neutralization of classical Coulomb term with the *exchange-correlation* term of LDA and GGA, which is not likely in HF.

amount of exact exchange is defined by the parameter, α in this equation (2.23). There is another parameter, η , which is a screening parameter that defines the long range (LR) and short range (SR) separation [76].

2.3.4 Van der Walls interaction

It has been known for a long period that the inability of the density functional theory to describe the intermolecular binding originates from the dispersion of Van der Walls (vdW) interaction [77–79]. A typical vdW interaction is shown

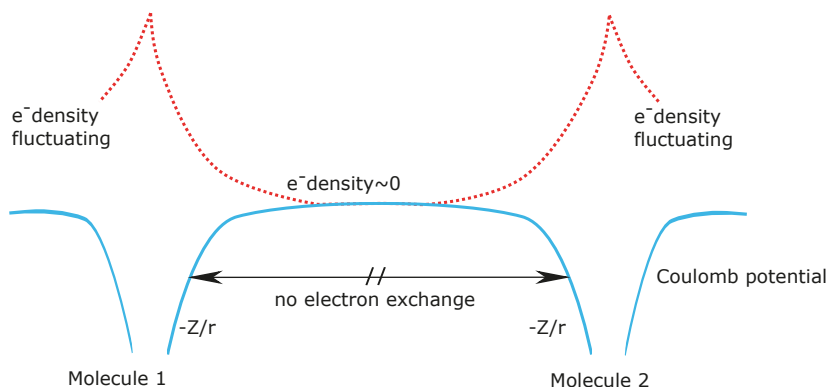


Figure 2.2. Schematic of the qualitative vdW interaction. This figure is reproduced with permission from the ref. [80].

in Figure 2.2, where the electron densities due to Coulomb potential are decaying exponentially. Usually the molecules are far apart (5-10 Å separation), and the broken arrow in between two molecule depicts the forbidden non-classical effects like electron exchange. Typically this long-range non local correlation is neglected in the LDA as well as in GGA formalism. This long-range attractive force is termed as vdW force. The origin of the force could be due to (i) two permanent dipoles, (ii) a permanent dipole and a corresponding induced dipole, and (iii) two instantaneously induced dipoles (London dispersion force) [77–79]. The present discussion is focused on the London dispersion force only, which is a long-range attractive force and it decays with inverse six power of the intermolecular distance. There are many methods to treat this interaction, *viz.* DFT-D [81–83], TS-vdW [84] and all the investigations in this thesis are based on Grimme DFT-D approach. In this method, a pairwise atomistic correction is used to account the vdW forces, where the total energy of the system is described as follows,

$$E_{DFT-D} = E_{KS} + E_{disp}, \quad (2.24)$$

where the E_{KS} is the KS energy obtained from the self consistent density functional formalism such as LDA, GGA. However, E_{disp} is the empirically cor-

rected dispersion energy, which has the following form,

$$E_{disp} = -s_6 \sum_{i=1}^{N_a-1} \sum_{j=i+1}^{N_a} \frac{C_6^{ij}}{R_{ij}^6} f_{damp}(R_{ij}), \quad (2.25)$$

where, C_6^{ij} is the dispersion coefficient of $\langle ij \rangle$ atom pair, which is geometric mean of C_6^i and C_6^j , N_a is the number of atoms, R_{ij} represents the interatomic distance in between i and j atom. s_6 is the global scaling factor. $f_{damp}(R_{ij})$ is the damping function preserves the long-range behavior of the dispersion interaction while prevent near singularities for small R . The damping function has the following from,

$$f_{damp}(R_{ij}) = \frac{1}{1 + e^{-d(R_{ij}/R_r - 1)}}. \quad (2.26)$$

Here, d is an adjustable parameter and R_r is the sum of the vdW atomic radius, R_i and R_j . One of the drawback of this formalism is the lack of information of the local chemical environment in the pair correlation coefficient, C_6^{ij} , which is considered in the recent version DFT-D3 [83], where the dispersion coefficients and cutoff radii are computed from first principles calculation.

2.4 Computational Methods

2.4.1 Basis Set

By computing the KS Eq. (2.13), it is possible to obtain KS wave function (ζ_i) and eigenvalues (ε_i) provided that we have properly defined exchange correlation functional. But, to solve Eq. (2.13) self-consistently, one needs to have the exact definition of the KS orbital (ζ_i), which is generally unknown. This is quite possible to express mathematically as a combination of a set of coefficients ($C_{i\gamma}$) and the basis set (Φ_γ),

$$\zeta_i = \sum_{\gamma=1}^N C_{i\gamma} \Phi_\gamma, \quad (2.27)$$

where, N is the number of basis functions. In principle, this basis set should follow the similar limiting behavior of the wave function. The coefficients ($C_{i\gamma}$) is also unknown and by substituting this ζ_i in Eq. (2.13) we have got the following equation

$$\left[-\frac{1}{2} \nabla^2 + V_{KS}(\mathbf{r}) \right] \sum_{\gamma=1}^N C_{i\gamma} \Phi_\gamma = \varepsilon_i \sum_{\gamma=1}^N C_{i\gamma} \Phi_\gamma. \quad (2.28)$$

Multiplying by the conjugate basis function, Φ_γ^* Eq. (2.28) and integrating over a volume element V takes the form,

$$\sum_{\gamma=1}^N C_{i\gamma} \int_V \Phi_\gamma^* \hat{h}_{KS} \Phi_\gamma d\mathbf{r} = \varepsilon_i \sum_{\gamma=1}^N C_{i\gamma} \int_V \Phi_\gamma^* \Phi_\gamma d\mathbf{r}, \quad (2.29)$$

where \hat{h}_{KS} has the following form,

$$\hat{h}_{KS} = \left[-\frac{1}{2} \nabla^2 + V_{KS}(\mathbf{r}) \right]. \quad (2.30)$$

The integral in Eq. (2.29) can be considered as matrix element of the KS, (\mathbf{H}^{KS}) and overlap (\mathbf{S}) matrices as follows:

$$\begin{aligned} \mathbf{H}^{KS} &= \int_V \Phi_\gamma^* \hat{h}_{KS} \Phi_\gamma d\mathbf{r}, \\ \mathbf{S} &= \int_V \Phi_\gamma^* \Phi_\gamma d\mathbf{r}. \end{aligned} \quad (2.31)$$

By introducing other two matrices, \mathbf{C} and ε for $C_{i\gamma}$ and eigenvalues (ε_i) respectively, the KS equation, Eq. (2.29) could be rewritten as follows:

$$\mathbf{H}^{KS} \mathbf{C} = \mathbf{S} \mathbf{C} \varepsilon. \quad (2.32)$$

The basis set involved in the new form of KS equation could be various types of mathematical function. In this thesis Gaussian type functions and plane waves are used to treat the molecule and periodic systems (solid) respectively.

2.4.2 Periodic System: Bloch Electrons

In a periodic system, not only the correlated nature of the electron, but also the infinite number of electrons raise the difficulties to predict the electronic structure by solving the KS equation. Employing the Bloch's theorem [85], the requirement of infinite number of electrons could be overcome by the finite number of electrons in a unit cell. It also states that the electrons in the solid are influenced by the effective potential, which is periodic in nature. In terms of Bloch wave function, the KS orbital can be expressed as follows:

$$\zeta_{j\mathbf{k}}(\mathbf{r}) = e^{i\mathbf{k} \cdot \mathbf{r}} u_{j\mathbf{k}}(\mathbf{r}), \quad (2.33)$$

where $u_{j\mathbf{k}}(\mathbf{r})$ is periodic function, possesses the crystal lattice periodicity, i.e. $u_{j\mathbf{k}}(\mathbf{r} + \mathbf{R}) = u_{j\mathbf{k}}(\mathbf{r})$, where \mathbf{R} is unit cell length or the translational vector. In Eq. (2.33), \mathbf{k} is the wave vector in the first Brillouin zone and j is the band index. The periodic function in Eq. (2.33) could be expanded in terms of Fourier series as follows:

$$u_{j\mathbf{k}}(\mathbf{r}) = \sum_{\mathbf{G}} \frac{1}{\sqrt{\Omega}} c_{j\mathbf{k}}(\mathbf{G}) e^{i\mathbf{G} \cdot \mathbf{r}}, \quad (2.34)$$

where $c_{j\mathbf{k}}$ are the plane wave expansion coefficients, and \mathbf{G} is the reciprocal lattice vector, expressed through, $\mathbf{G} \cdot \mathbf{r} = 2\pi m$, where m is an integer and \mathbf{r} is the real space vector. Now the KS orbital in a linear combination of the plane waves could be written as follows,

$$\zeta_{j\mathbf{k}}(\mathbf{r}) = \sum_{\mathbf{G}} c_{j\mathbf{k}}(\mathbf{G}) \times \frac{1}{\sqrt{\Omega}} e^{i(\mathbf{k}+\mathbf{G}) \cdot \mathbf{r}}, \quad (2.35)$$

where \mathbf{k} is the Bloch wave vector, $c_{j\mathbf{k}}$ are the expansion coefficient of the wave function in plane wave basis, $e^{i(\mathbf{k}+\mathbf{G}) \cdot \mathbf{r}}$, and $\frac{1}{\sqrt{\Omega}}$ is the normalization factor. Now the KS equation in terms of plane wave basis set could be expressed as in Eq. 2.28. Now the KS equation could take this form by expanding the electronic wave function in terms of plane wave,

$$\sum_{\mathbf{G}'} \left[\frac{\hbar^2}{2m_e} |\mathbf{k} + \mathbf{G}|^2 \delta_{\mathbf{G}'\mathbf{G}} + V_{KS}(\mathbf{G} - \mathbf{G}') \right] c_{j\mathbf{k}}(\mathbf{G}) = \varepsilon_{j\mathbf{k}} c_{j\mathbf{k}}(\mathbf{G}). \quad (2.36)$$

The Eq. (2.36) could be obtained by substituting Eq. (2.35) in Eq. (2.28), and subsequently replacing⁴ atomic unit with fundamental constant and multiplying with $e^{-i(\mathbf{k}+\mathbf{G}') \cdot \mathbf{r}}$ from the left and integrating over \mathbf{r} . This Eq. (2.36) could be solved by diagonalising the Hamiltonian matrix $H_{\mathbf{k}+\mathbf{G},\mathbf{k}+\mathbf{G}'}$, whose matrix elements are the terms in the bracket above. It could be depicted from Eq. (2.36) that the kinetic energy is diagonal, and the potential (V_{KS}) is in terms of Fourier components. The size of the matrix depends on the cut off energy (E_{cut}) which is defined as,

$$E_{cut} = \frac{\hbar^2}{2m_e} |\mathbf{k} + \mathbf{G}_{max}|^2. \quad (2.37)$$

This E_{cut} has been suggested to obtain the finite basis set by fixing the highest reciprocal lattice vector, \mathbf{G} , used in plane wave expansion. Moreover, the size of the matrix also depends on the number of valence and core electrons in the system. The all-electron calculation together with Coulombic potential for nuclei is also expensive with plane wave basis set. Since high oscillatory nature of the valence electrons and the tightly bound core orbitals require the large number of plane wave basis sets to properly describe the electronic wave functions. This latter problem could be overcome by considering another approximation, *pseudopotential*, which has been discussed in the subsequent section.

2.4.3 Pseudopotential

This section is devoted to discuss the solution to overcome the computational difficulties to represent the highly localised core electron (close to nucleus)

⁴ All the previous equations in this thesis are written in atomic unit without considering explicitly any fundamental physical constant

wave functions along with the strong nuclear Coulomb potential by considering the *pseudopotential* approximation. This approximation is based upon the observation that the core electrons are relatively unperturbed by the crystalline environment of an atom. So the actual changes in the valence electron energies are most important when isolated atoms are brought together to form a chemical bond to form molecule or crystal. Since the core electron wave-functions are significantly unaffected during bond formation, then it is possible to combine the core potential with the nuclear Coulomb potential. Subsequently the valence electrons would perceive this combined potential, named as *pseudopotential*. The method of combining the core with the nuclear Coulomb potential is called frozen-core approximation.

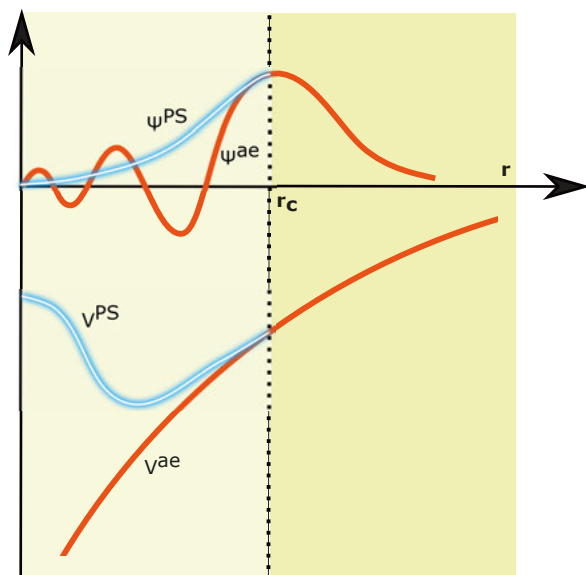


Figure 2.3. Schematic illustration of the pseudopotential concept. The solid red lines show the all-electron wave function ($\Psi^{\text{ae}}(\mathbf{r})$), and ionic potential ($v_{\text{ion}}^{\text{ae}}(\mathbf{r})$), while the double-colored lines show the pseudopotential ($v^{\text{PS}}(\mathbf{r})$) and corresponding pseudo-wavefunction ($\Psi^{\text{PS}}(\mathbf{r})$). All the potentials and wave functions are shown as a function of distance, \mathbf{r} , from the atomic nucleus. Beyond the cutoff radius (r_c) (the dotted line) pseudo wave function and pseudopotential shows the resemblance of the all-electron nature.

The pseudopotential approximation replaces the strong and steep ionic potential ($-\frac{Z}{r}$) in the core region, by a weaker pseudopotential. Correspondingly, the all-electron wavefunctions $\psi^{\text{ae}}(\mathbf{r})$ in the core region are replaced by the set of pseudo-wavefunctions $\psi^{\text{PS}}(\mathbf{r})$ and those are identical above the chosen cut-off radius r_c . In the core region (where $r < r_c$), the $\psi^{\text{PS}}(\mathbf{r})$ does not have the nodal structure that causes the oscillations, which means the wave functions in this region could be described with a reasonable number of plane-waves.

A schematic illustration of the pseudopotential concept is depicted in Figure 2.3. The separation between core and valence electrons depends on the target accuracy of the calculation⁵ by specifying the cutoff radius.

In 1959, Phillips and Kleinman [86] formulated the first pseudopotential theory based on the orthogonalised-plane-wave (OPW) method of Herring [87]. Following the orthogonalised plane-waves approach, let ψ_i be a state vector and E be its energy eigenvalue. Here the suffix, $i = c$ and v represents respectively core and valence state. Then, with Hamiltonian \hat{H} , the Schrödinger equation takes the following form

$$\hat{H}|\psi_i\rangle = E_i|\psi_i\rangle . \quad (2.38)$$

From these states, we can write, ψ_v in terms of a smoother pseudo-state $|\varphi\rangle$ and a linear combination of core eigen states ($|\psi_c\rangle$) with coefficients a_{cv} for the oscillating parts, as follows:

$$|\psi_v\rangle = |\psi^{PS}\rangle + \sum_c |\psi_c\rangle a_{cv} . \quad (2.39)$$

Now the expansion coefficients a_{cv} are obtained from the orthogonality condition of valence state with core state:

$$\langle\psi_c|\psi_v\rangle = 0 = \langle\psi_c|\psi^{PS}\rangle + a_{cv} . \quad (2.40)$$

Thus with the substitution of a_{cv} , Eq. (2.39) will be as follows,

$$|\psi_v\rangle = |\psi^{PS}\rangle - \sum_c |\psi_c\rangle \langle\psi_c|\psi^{PS}\rangle . \quad (2.41)$$

Further substituting the Eq. (2.39) in the Schrödinger equation, Eq. (2.38) gives,

$$\begin{aligned} \hat{H}|\psi^{PS}\rangle - \sum_c E_c |\psi_c\rangle \langle\psi_c|\psi^{PS}\rangle &= E_v \left(1 - \sum_c |\psi_c\rangle \langle\psi_c| \right) |\psi^{PS}\rangle \\ \Rightarrow \hat{H}|\psi^{PS}\rangle + \sum_c (E_v - E_c) |\psi_c\rangle \langle\psi_c|\psi^{PS}\rangle &= E_v |\psi^{PS}\rangle . \end{aligned} \quad (2.42)$$

⁵For few elements this separation is obvious, for example if we consider the first element in Halogen series, Fluorine, the electronic configuration of which is: $1s^2 2s^2 2p^5$. Now $1s$ state has ionisation potential in the order of 1keV while for $2s, 2p$ is in the order of 10-100 eV. Also $1s$ state is highly localised compare to $2s$ and $2p$ state. So there is a clear chemical intrusion to consider $1s$ state only in the core. Now if we consider the Titanium atom, whose electronic configuration: $1s^2 2s^2 2p^6 3s^2 3p^6 4s^2 3d^2$. Here, it is difficult to draw the universal r_c . There could be small core ($1s^2 2s^2 2p^6$) and large core ($1s^2 2s^2 2p^6 3s^2 3p^6$) possibility due to the very close ionisation potential of $3p$ (99.2 eV) and $4s$ (43.3 eV) and overlap in the localisation region of $3p$ and $4s$. Then the change of possible occupation in $4s$ may change the potential felt by $3p$ and rearrange the $3p$ state. The small core could be appropriate to get the proper electronic structure in case of $BaTiO_3$, where oxygen pump in the Ti electron could also rearrange the $3s$ & $3p$. Whereas in case of Ti metal, large core is appropriate where $4s$ & $3d$ could be considered as valence orbitals.

So with the energy-dependent non-local potential (\hat{V}_{nl}), the pseudo-state also obeys the schrödinger equation of the following form:

$$\begin{aligned} (\hat{H} + \hat{V}_{nl}) |\psi^{PS}\rangle &= E_v |\psi^{PS}\rangle \\ \text{where, } \hat{V}_{nl} &= \sum_c (E_v - E_c) |\psi_c\rangle \langle \psi_c|. \end{aligned} \quad (2.43)$$

Then the pseudopotential (\hat{V}_{PS}) is defined by combining the true potential, \hat{V} and \hat{V}_{nl} ,

$$\hat{V}_{PS} = \hat{V} + \hat{V}_{nl}. \quad (2.44)$$

From the above construction of \hat{V}_{PS} with Eq. (2.44) and Eq. (2.43), we can observe that \hat{V}_{PS} is weaker than the true potential (\hat{V}), which is due to the lower core energy (E_c) as compared to the valence energy (E_v). The \hat{V}_{nl} term in the core region is repulsive in nature, which is partially canceling the attractive potential \hat{V} , then weaken the pseudopotential and hence corresponding pseudo wave function becomes smooth.

2.4.4 Projected Augmented Wave method

In the projected augmented wave (PAW) method, the system is divided into two parts: augmented region, which is made up of non-overlapping sphere around each ion of the system and rest of the system as interstitial region. The strategy of this method is based on also separating the true wave function into two regions: partial wave function for inside and envelop function for outside the augmented sphere [88]. Both of these wave functions must be matched outside the sphere and continuous at the interface of augmented-interstitial region. Due to the large number of partial waves close to the core, the true all electron wave function (ψ) should be mapped into the computationally convenient fictitious smooth or auxiliary wave function ($\tilde{\psi}$) with less number of partial wave basis sets. This auxiliary wave functions should be the eigenfunctions of the KS equations for an isolated atom. Inside the augmented sphere of volume Ω_R , the auxiliary wave function could be expanded as linear combination of partial wave basis sets, similar to the true all electron wave function:

$$\begin{aligned} |\psi(\mathbf{r})\rangle &= \sum_i c_i |\phi_i(\mathbf{r})\rangle \quad \text{inside } \Omega_R \\ |\tilde{\psi}(\mathbf{r})\rangle &= \sum_i d_i |\tilde{\phi}_i(\mathbf{r})\rangle \quad \text{inside } \Omega_R. \end{aligned} \quad (2.45)$$

where c_i , d_i are the expansion coefficients, and index i refers to the angular momentum (l,m) and atomic site R . Outside the sphere, i.e. beyond the cut-off radius (r_c) the all electron and the auxiliary partial wave are identical, hence

one can write the following:

$$\phi_i(\mathbf{r}) = \tilde{\phi}_i(\mathbf{r}) \quad \text{outside } \Omega_R . \quad (2.46)$$

The auxiliary partial wave could be obtained from the all electron partial wave, which is the solution of Schrödinger equation for an isolated atom. The all electron partial wave function is connected with the auxiliary partial wave function through the linear transformation operator, τ , as follows:

$$|\psi\rangle = \tau|\tilde{\psi}\rangle , \quad (2.47)$$

$$\text{where } \tau = \hat{\mathbf{1}} + \sum_R S_R . \quad (2.48)$$

The transformation operator (τ) defines the way to reach the true wave function from the auxiliary partial wave. This τ consists of a identity operator $\hat{\mathbf{1}}$ and a sum of the atomic contribution at each particular site R , denoted as S_R . The S_R actually represents the difference between all electron partial wave function and the auxiliary partial wave, i.e.

$$S_R|\tilde{\phi}_i\rangle = |\phi_i\rangle - |\tilde{\phi}_i\rangle . \quad (2.49)$$

Now let us define the projector operator, $|\tilde{P}_i\rangle$, which form a connection between the augmented and the interstitial region. This operator must fulfill the following completeness relation,

$$\sum_i |\tilde{\phi}_i\rangle\langle\tilde{P}_i| = 1 , \quad (2.50)$$

and the orthogonality relation,

$$\langle\tilde{\phi}_i|\tilde{P}_j\rangle = \delta_{i,j}; \text{ for } i, j \in R . \quad (2.51)$$

By using the above relations, the auxiliary wave function could be expressed as,

$$|\tilde{\psi}\rangle = \sum_i |\tilde{\phi}_i\rangle\langle\tilde{P}_i|\psi\rangle . \quad (2.52)$$

Inserting Eq. (2.52) in Eq. (2.47), the all electron true wave function could be represented following PAW ansatz, as below:

$$|\psi\rangle = |\tilde{\psi}\rangle + \sum_i (|\phi_i\rangle - |\tilde{\phi}_i\rangle)\langle\tilde{P}_i|\tilde{\psi}\rangle , \quad (2.53)$$

$$= |\tilde{\psi}\rangle + \sum_R \left(|\psi_R^1\rangle - |\tilde{\psi}_R^1\rangle \right) , \quad (2.54)$$

where,

$$|\psi_R^1\rangle = \sum_{i \in R} |\phi_i\rangle \langle \tilde{P}_i | \tilde{\psi} \rangle , \quad (2.55)$$

$$|\tilde{\psi}_R^1\rangle = \sum_{i \in R} |\tilde{\phi}_i\rangle \langle \tilde{P}_i | \tilde{\psi} \rangle . \quad (2.56)$$

While outside the sphere of volume Ω_R , $|\psi_R^1\rangle = |\tilde{\psi}_R^1\rangle$, i.e. the auxiliary wave function is identical to the true wave function, whereas inside the sphere, $|\psi\rangle = |\tilde{\psi}_R^1\rangle$. A graphical illustration of PAW ansatz is shown in Figure 2.4.

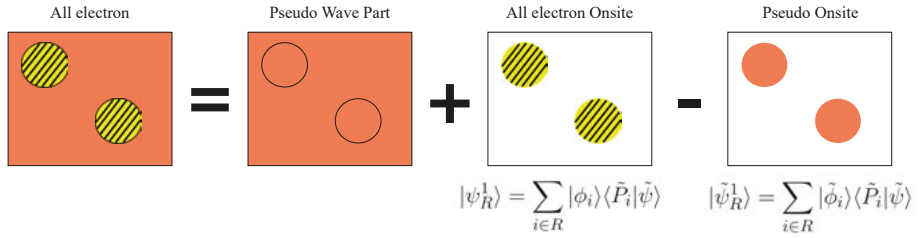


Figure 2.4. Schematic of the PAW method

The left box represents the true wave function as a combination of smooth (shown by orange colour) at the interstitial and hard (shown by yellow colour) i.e. oscillating part at the core region. The true wave function in terms PAW method is expressed as combination of pseudo plane wave part summed with all electron partial wave on the sphere and subtracted the pseudized partial wave on the sphere. The Eq. (2.53) could be rearranged in the form of,

$$|\psi\rangle = \left(\hat{\mathbf{1}} + \sum_i (|\phi_i\rangle - |\tilde{\phi}_i\rangle) \langle \tilde{P}_i | \right) |\tilde{\psi}\rangle . \quad (2.57)$$

Now if we recall Eq. (2.47) and compare with Eq. (2.57), the transformation operator (τ) will be,

$$\tau = \hat{\mathbf{1}} + \sum_i (|\phi_i\rangle - |\tilde{\phi}_i\rangle) \langle \tilde{P}_i | . \quad (2.58)$$

By means of transformation operator, the KS equation could be written as,

$$\left(\tilde{H} - \varepsilon \tilde{O} \right) |\tilde{\psi}\rangle = 0 , \quad (2.59)$$

where, $\tilde{H} = \tau^\dagger H \tau$ and $\tilde{O} = \tau^\dagger \tau$ are respectively represented the pseudo-Hamiltonian and the overlap operator. Now the problem becomes computationally less expensive as less number of plane waves needed to describe the KS orbitals.

2.4.5 Hellmann-Feynman Force Theorem

The force between the ions is an important parameter to justify the equilibrium position or the ground state of the system. At the exact ground state, the total force acting on the system is in principle zero, which is not true for the atoms that are not in equilibrium position. The force acting on the given nucleus at position R_N could be expressed as,

$$F_N = -\frac{\partial E}{\partial R_N}, \quad (2.60)$$

where the total energy of the system,

$$E = \frac{\langle \psi | H | \psi \rangle}{\langle \psi | \psi \rangle} \quad (2.61)$$

The wave function or the KS orbital ψ should be normalized, i.e. $\langle \psi | \psi \rangle = 1$. Now by substituting Eq. (2.61) in Eq. (2.60),

$$F_N = -\langle \psi | \frac{\partial H}{\partial R_N} | \psi \rangle - \langle \frac{\partial \psi}{\partial R_N} | H | \psi \rangle - \langle \psi | H | \frac{\partial \psi}{\partial R_N} \rangle \quad (2.62)$$

By recalling the KS equation, $H|\psi\rangle = E|\psi\rangle$,

$$F_N = -\langle \psi | \frac{\partial H}{\partial R_N} | \psi \rangle - E \left(\frac{\partial \langle \psi | \psi \rangle}{\partial R_N} \right). \quad (2.63)$$

While using $\langle \psi | \psi \rangle = 1$, F_N becomes as follows:

$$F_N = -\langle \psi | \frac{\partial H}{\partial R_N} | \psi \rangle. \quad (2.64)$$

It means the expectation value of the Hamiltonian's derivative is the derivative of the energy with respect to any parameter. This Eq. (2.64) represents the Hellmann-Feynman force theorem [63]. In the calculation process, the ions should move in such a way that the force of the system goes to zero while corresponding energy of the system will take the lowest energy value.

2.4.6 Crystal Structure Prediction: Constrained Evolutionary Algorithm

In addition to the chemical composition, the crystal structure is the most important factor to determine the properties of the material. In this connection, prediction of the global structure is most valuable task to design them prior to experimental synthesis. For crystal structure prediction, various global optimization techniques are invented and utilized, e.g. simulated annealing [89, 90], evolutionary algorithms (EA) [91, 92], random sampling [93], basin hopping

[94], minima hopping [95]. In the global optimization process, a good balance between the exploration (global) and exploitation (local) technique is the key to successfully predict the global crystal structure. Compared to other global optimization methods, EA has some distinct advantage. As the name *evolution* suggested that during the exploration of search space it will go through a series of intelligently designed moved, self-learning, natural selection to evolve the global structure. This technique has been well explored and reported for prediction of inorganic crystal structures, even with the application of external pressure [96, 97]. For inorganic systems and also the system with small molecule, like CO_2 and H_2O , it is mostly used by assembling the individual atoms. However for prediction of organic crystal with the large molecule, considering the individual atoms as the building unit will complicate the technique and enlarge the search space further, hence will make the process computationally expensive. More explicitly the following concerns should take into account to predict the organic crystal structure:

(i) usually the presence of a large number of atoms in the unit cell compares to the typical inorganic crystal structure

(ii) large empty space within the crystal due to intermolecular distance and vdW force leads to large cell size

(iii) thermodynamical instability of the molecules compared to their small derivative, force the algorithm to spend time on exploring uninteresting disordered structures. For example, to predict the global crystal structure of Hydroquinone ($C_6H_6O_2$), the algorithm should not explore the search space of mixed structure of CO, CH_4 , H_2O etc.

(iv) more than 80 % of the organic crystal structure (having mostly monoclinic and triclinic family) possess lower symmetry space group, $P2_1/c$ (36.59 %), $P\bar{1}$ (16.92%), $P2_12_12_1$ (11.00%), $C2/c$ (6.95%), $P2_1$ (6.35%) and $Pbca$ (4.24%).

The last two features could be used to enhance the efficiency of the search process, whereas the first two are implying the large search space and hence expensive search space. Here comes the importance of the *constrained evolution algorithm*, where instead of taking the individual atom, the whole molecule is the building unit, which will remain same (rigid) in terms of chemical nature and chemical bond even after the natural selection, hence will reduce the search space and computational cost. Therefore to predict the organic crystal structure, we have used *constrained evolution algorithm*, similar to the method implemented in USPEX[91, 98]. The procedures to create the global structure are as follows:

(I) initial organic crystals are generated randomly with the randomly selected space group by keeping the molecules at the Wyckoff position under the specified constraints⁶. Here we can consider only the space group of upto orthorhombic crystal system (upto the space group 74).

⁶such as interatomic distances, intermolecular distance, lattice parameter.

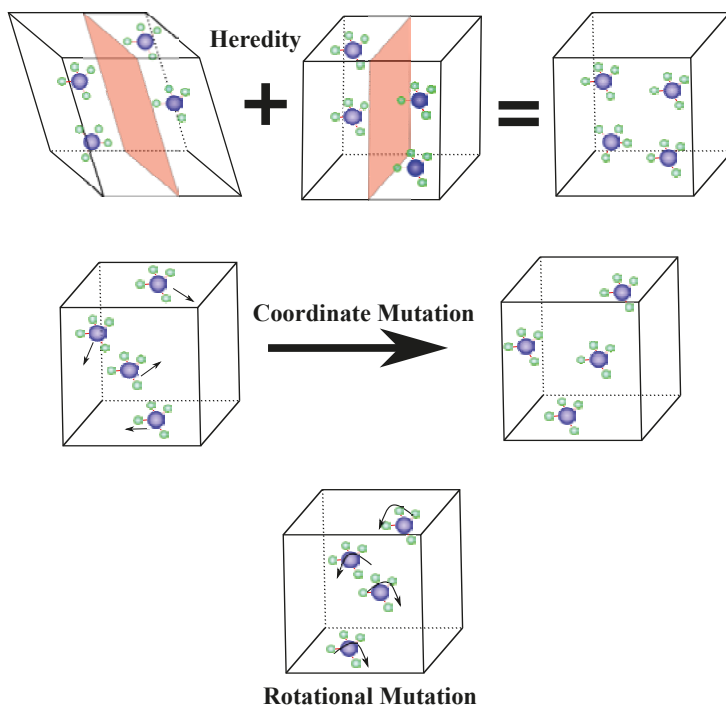


Figure 2.5. Schematic of the variation operators

(II) after creating the initial population, all the structures are allowed to relaxed locally on the basis Kohn-Sham formalism including vdW dispersion.

(III) the non-identical structures are identified using the fingerprint function⁷ and ranked are based on the Kohn-Sham energy. Then a few percentage (depending on the choice of setting) of the higher energy structures are removed and rest of them are allowed to form new generation by employing the variation operators.

(IV) after identifying the parent structure, all other off-spring structures are generated by using the variation operators. To maintain the diversity of the new generation population: the best individuals of previous generation and new randomly generated structures from the symmetry are inserted in the present population.

(V) subsequently the new population under goes through the local optimization and all structures are evaluated and ranked.

(VI) searching process (repeating the (IV) and (V) step) is continued until the halting criteria reached. The halting criteria could be defined as follows:

⁷It is a descriptor (formulated based on interatomic distance, number of atoms, unit cell volume) to identify the similar structure.

the same best structure should be created repeatedly within the specified number of generations⁸.

Now various operators are: (1) heredity, (2) permutation, (3) coordinate mutation, (4) rotational mutation and (5) softmutation. The *heredity* operator is based on the cut-splice method. This operator cut a slab of random thickness at random height of the individual cell and then combine them together to form the child structure. Now during this process to fix the total number atoms of the parent structure a corrector process is also performed to add or subtract the atoms. In the *permutation* operator, swapping of the chemical nature takes place randomly in between selected pairs of the building blocks. The *coordinate mutation* operator moves the center of the molecule i.e. in fact the whole molecule randomly in random directions. Whereas the *rotational mutation* operator rotates the randomly selected molecules with a random angle. To predict the organic molecule crystal this operator is most important to predict the proper molecular packing corresponding to the global structure. The *softmutation* operator displaced the coordinates along the softest mode eigenvectors or along the linear combination of the softest eigenvectors. This is also referred as a hybrid operator, which combines the rotational and coordinate mutation operator. This *constrained evolution algorithm* is employed in this thesis in the prediction of global molecular crystal, such as dilithium terephthalate ($Li_2C_8H_4O_4$), sodiated quinone ($Na_XC_6Cl_4O_2$)[53, 54].

The density functional theory has been used in the subsequent chapters of this thesis. More specifically, the constrained evolutionary algorithm has been used in *Chapter 5* to find out the global structure of electrode materials.

⁸For example, we can specify halting criteria for the simulation, e.g., the best structure should come 20 times out of 30 generations.

Part II:

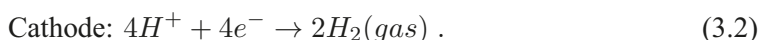
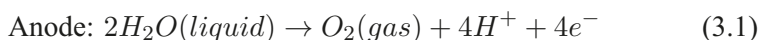
Energy Production

3. Probing Hydrogen and Oxygen Evolution Reaction Mechanism

One of the important parameters for achieving the hydrogen energy economy is to find out the cheapest and clean source of hydrogen. For this quest direct splitting of water could be an efficient way of producing hydrogen. Water is most practical choice due to its plentifulness and the produced hydrogen without any carbon contamination which is very common in the production processes based on hydrocarbons decomposition. The splitting reaction is endothermic, which means it requires energy supply to start the reaction. One of the simplest ways to provide the required energy is through electrochemical reaction. This electrochemical water splitting has drawn substantial interest from the past few years as a key process in hydrogen production from sunlight and other sources of electricity [99].

In the water electrolysis process hydrogen and oxygen gasses are generated from water as follows: $2H_2O(liquid) \rightarrow 2H_2(gas) + O_2(gas)$. In the electrochemical cell a minimum potential difference of 1.23 V is required under thermodynamic equilibrium at room temperature (298 K) and standard pressure, which is an ideal condition. Practically to drive the non-spontaneous reaction, a higher potential has to be applied in terms of overpotential and resistance losses.

The overall reaction could be divided into two half cell reactions,



Eq. (3.2) and Eq. (3.1) are denoted as hydrogen evolution and oxygen evolution reaction at acidic condition, respectively.

Only the full cell potentials could be measured directly, so to obtain the half cell potential of the working electrode, the potential of the reference electrode must be known. In all the studies here, standard hydrogen electrode (SHE) is considered as the reference electrode, which keeps the equilibrium of the reaction:



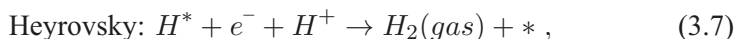
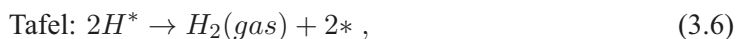
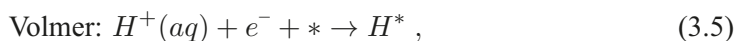
It is worth to mention here that the equilibrium of this reaction is dependent on the chemical potential of protons as well as electrons. Theoretically, it is more convenient to calculate the energy of H_2 rather than the other two species. The construction of this reference electrode has been elaborated in literatures [100–102].

3.1 Hydrogen Evolution Reaction

The hydrogen evolution reaction (HER) is an electrochemical half-cell reaction in which protons are reduced into hydrogen [103–105]. That's why it is also known as hydrogen reduction reaction. The HER is mostly occurred as a cathodic reaction during water electrolysis as shown in Eq. (3.2). This is a two electron transfer process, where protons are reduced to form molecular hydrogen. Similar to Eq. (3.2) the overall HER in acidic medium could be rewritten as follows:



The HER could be further splitted up into the following elementary reactions:



where the $*$ denotes a site on the catalyst surface (so only an $*$ means a free site) and H^* denotes a hydrogen atom adsorbed on the catalyst surface. It is commonly admitted that the first step in the HER is the Volmer process, where a proton-electron pair forms an adsorbed hydrogen atom on the surface. The second step of the HER, where hydrogen molecule is formed, could be occurred through either the Tafel or the Heyrovsky reaction or through both. In the Tafel reaction (Eq. (3.6)), two adsorbed hydrogen atoms first diffuse on the catalyst surface and subsequently form a hydrogen molecule upon interacting. In case of Heyrovsky reaction, (Eq. (3.7)), a proton from the electrolyte first adsorbs directly onto a hydrogen atom already adsorbed on the surface of the catalyst, then gets reduced to form hydrogen molecule. However, it has been proven difficult to understand that which mechanism dominates [104, 106, 107]. Despite this uncertainty in the understanding of HER from all these reaction it has been observed that the adsorbed hydrogen, H^* is the only one intermediate species in the entire process.

According to the qualitative rule of Sabatier, a catalyst material to be an excellent catalyst for a given process, should not interact too strongly or too weakly with the reactants [108]. Now in context of the HER, the Sabatier principle suggests that the optimal HER catalyst should not bind hydrogen too strongly or too weakly [109, 110]. This means the adsorption free energy of hydrogen under the standard conditions of the HER (at 298 K and 1 bar) should be zero eV at an electrode potential of $U = 0$. Consequently at standard condition, the adsorption free energy of the Eq. (3.5) could be calculated as the free energy of the reaction of $H^* \rightarrow * + \frac{1}{2}H_2$. To predict the good catalyst for HER, we need to determine only the adsorption energy of the hydrogen atom on the catalyst. The adsorption energy is related with the the adsorption free

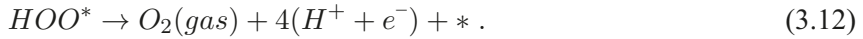
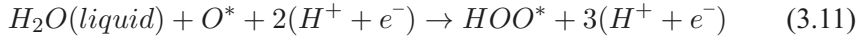
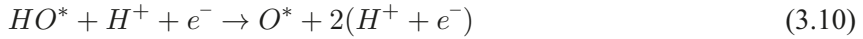
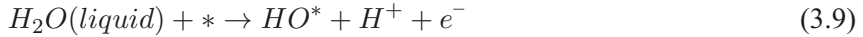
energy by using the following equation:

$$\Delta G = \Delta E + \Delta ZPE - T\Delta S, \quad (3.8)$$

where ΔE is the adsorption energy calculated using DFT, ΔZPE is the difference in zero point energies and ΔS is the change in entropy during the reaction.

3.2 Oxygen Evolution Reaction

Production of hydrogen through water-electrolysis is correlated with substantial energy losses and the hydrogen intermediate in the HER. However, most of the overpotential giving rise to the losses and the source of the hydrogen intermediate are associated with the electrochemical processes at the anode, where oxygen evolution reaction (OER) is taking place [111]. The oxygen evolution reaction (OER) is more complex than HER and it involves more than one intermediates, unlike HER. The OER could also be classified as four-electron pathway, since it involves four electrons in the reaction. In acidic condition, the OER mechanism could be written as follows:



According to the above reactions, in the first step of the OER (Eq. (3.9)), water molecule is dissociated into an adsorbed hydroxide and a solvated proton. Subsequently, the adsorbed hydroxide is further oxidised to form adsorbed atomic oxygen and another set of solvated protons as shown in Eq. (3.10). In Eq. (3.11) the adsorbed atomic oxygen is further reacted with another water molecule to form the adsorbed peroxide, HOO^* . Finally, the molecular oxygen is formed from the adsorbed peroxide and releases the absorbed site of the surface as depicted in Eq. (3.12).

Mechanism of the water oxidation to produce the molecular oxygen through the OER has been elucidated by using free energy model, which relate the overpotential to the binding energies of the intermediates [100, 102]. Determining the binding energies of intermediates such as O^* , OH^* and HOO^* are the main key of this model. DFT could be used to calculate this binding energy of the intermediates on the catalyst surface. The adsorption free energy of the intermediates could be obtained from the binding energy by using the Eq. (3.8). The change in the free energy for each step in the reaction at $U = 0V$ could be calculated by using SHE. Thermodynamical feasibility of each step in the reaction is defined by this change in free energy, which should be either zero

or negative. The adsorption free energy of all the four steps together will form a free energy diagram as shown in Figure 3.1. The largest height of the step

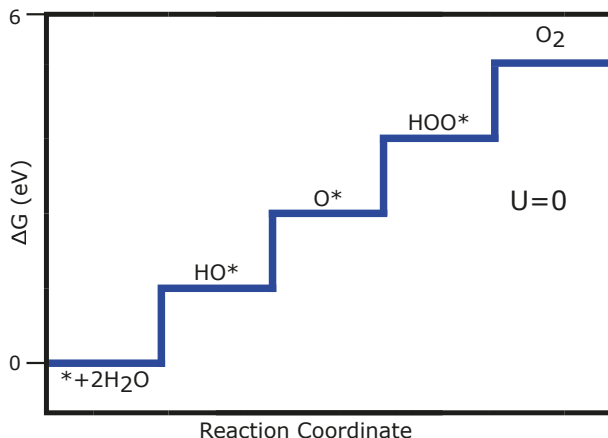


Figure 3.1. Standard free energy diagram for the OER at $U=0$ for ideal catalyst.

in the free energy diagram, Figure 3.1, is the magnitude of the potential determining step or the rate limiting step for OER. The theoretical over potential at standard condition could be obtained from this rate limiting step with respect to the equilibrium potential, 1.23 V. Essentially when all steps are downhill in energy with the applied potential, the OER reaction could proceed at significant rate. The application of this model on various catalyst surfaces like 2D monolayer and metal oxide are discussed in the following section in an elaborate form.

3.3 2D ultra-thin catalyst

In the past couple of decades, noble metal platinum (Pt) has been emerged to be the best catalyst for the HER, due to its high activity and stability [103, 112]. However, the cost-effectiveness along with the geopolitical abundance of Pt, urge to design an efficient catalyst based on the abundant and cheap elements of the periodic table to replace the precious metal based catalyst for HER and OER [113, 114]. In this context, ultra-thin 2D sheets based on B, C, Al and also for metal oxide are evaluated as HER/OER catalysts.

3.3.1 Probing of bifunctional catalytic activity of borophene monolayer

First-principles DFT based spin-polarized electronic structure calculations have been performed in order to find the minimum energy configurations of pristine

and Ti-functionalized borophene monolayer. Figure 3.2 depicts the 2D pristine buckled borophene sheet from the top and side perspectives, where T1, T2 and B1, B2 are the top and bottom boron atom, respectively, with similar bond lengths T1–T2 and B1–B2 and with the corresponding buckling height of 0.877 Å. The bird's eye and side views of the relaxed lowest energy Ti-functionalized borophene structure are shown in Figure 3.2. Strong coordina-

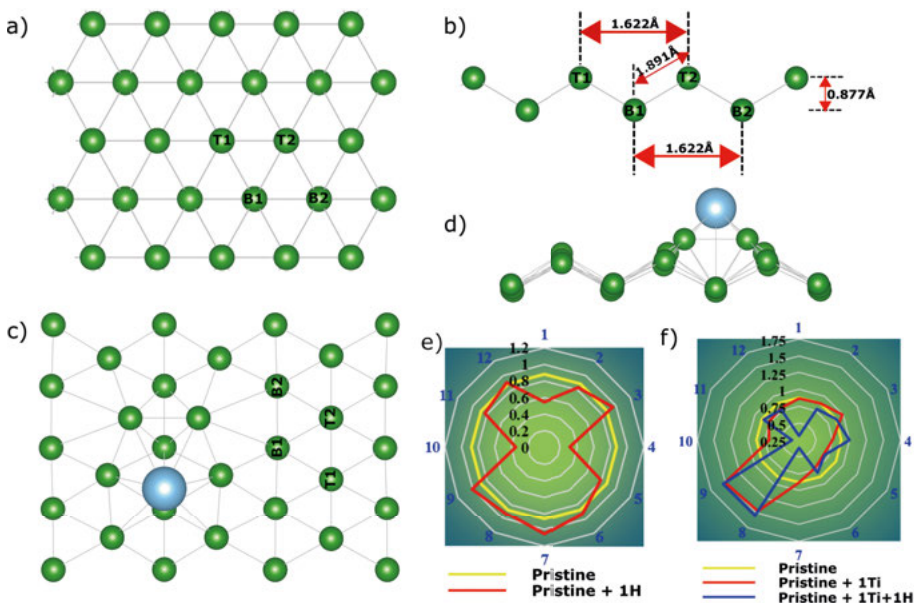


Figure 3.2. (a) Bird's eye view and (b) side view of borophene; (c) Bird's eye view and (d) side view of Ti-functionalized borophene; (e) variation of buckling height in monohydrogenated borophene in comparison with pristine borophene; (f) variation of buckling height of Ti-decorated borophene in comparison with pristine borophene. Green, light pink, and sky blue represent boron, hydrogen, and Ti atoms, respectively. This figure is taken with permission from [105]. Copyright © 2018, American Chemical Society.

tion of Ti adatom with the pristine sheet that has been reflected in terms of buckling height variation, due to the substantial charge distribution in the Ti-functionalized borophene sheet. The buckling height is ramping strongly with Ti functionalization as compared to the pristine monolayer of borophene, as represented in Figure 3.2. Moreover, change in buckling height with monohydrogenation is also depicted in Figure 3.2, while with mono-hydrogenation of pristine borophene the buckling height varies from 0.311 to 1.053 Å. The calculated vibrational frequency of the adsorbed hydrogen in pristine borophene is 2443.15 cm^{-1} with the B–H bond length of 1.204 Å, whereas in case of Ti-functionalized borophene is 2364.66 cm^{-1} with the B–H bond length of 1.213 Å.

After studying the structural variation with hydrogenation, the corresponding adsorption free energy diagram at equilibrium potential and pH = 0 is shown in Figure 3.3 (a). It shows that the associated proton transfer for the catalytic reaction on pristine as well as on Ti-functionalized borophene monolayer is exothermic. The adsorption free energy of the pristine and Ti-functionalized borophene sheet is 0.41 eV and 0.20 eV respectively. The associated adsorption free energy for HER with the inclusion of Ti functionalization is much more thermoneutral while getting close to the ideal Pt catalyst. However, this calculated adsorption free energy only considers the intermediate binding energy of HER at pH=0 and zero bias voltage without specifying the explicit water environment.

The free energy diagram with respect to the reaction coordinate associated with the OER mechanism, as it shown in Figure 3.3 (b). The adsorption free energies are obtained after adsorbing O^* , OH^* , and OOH^* in different structural configurations on pristine and Ti-functionalized borophene sheets in order to find the relaxed structures with the lowest energy values. The change in free energy in between OH^* and O^* , and in between O^* and OOH^* are denoted as ΔG_1 and ΔG_2 respectively. The ΔG_1 and ΔG_2 in both the cases of pristine and Ti-functionalized sheets are $\Delta G_1^B = 1.165$ eV, $\Delta G_1^{B+Ti} = 1.904$ eV, $\Delta G_2^B = -3.945$ eV, $\Delta G_2^{B+Ti} = -0.357$ eV. Apart from the competitive free energy for the hydroxyl formation for both cases, the possible rate-determining step in the pristine and the Ti-functionalized case is O^* oxidation to OOH^* and OH^* oxidation to O^* , respectively. Moreover, under the influence of Ti functionalization, the subsequent reaction barrier, O^* to OOH^* , has become negligible, which indicates the easy formation of OOH^* . The details of the reaction mechanism and charge distribution of the system during the reaction have been discussed in *Paper I* of this thesis.

3.3.2 Catalytic activity in pristine and functionalized Al_2C monolayers

The amount of energy required by a photon to split the water is 1.23 eV, which is essentially equivalent to the optimum band gap needed in photocatalytic material for water splitting. The incident photon with energy equal or higher than 1.23 eV on the catalytic surface are subsequently excited the electron to the conduction band edge and hole to the valance band edge. This excited electron and hole respectively assist to generate hydrogen through HER and oxygen through OER. However, at the same time possibility of the recombination of electrons and holes could diminish the photocatalytic efficiency.

The monolayer of aluminium carbide (Al_2C) is a newly predicted 2D material in the 2D material horizon [116]. This 2D material could be one of the possible photocatalytic materials with a band gap of 1.05 eV [116]. The Al_2C monolayer consists of planar tetra coordinate carbon (ptC) structure, where

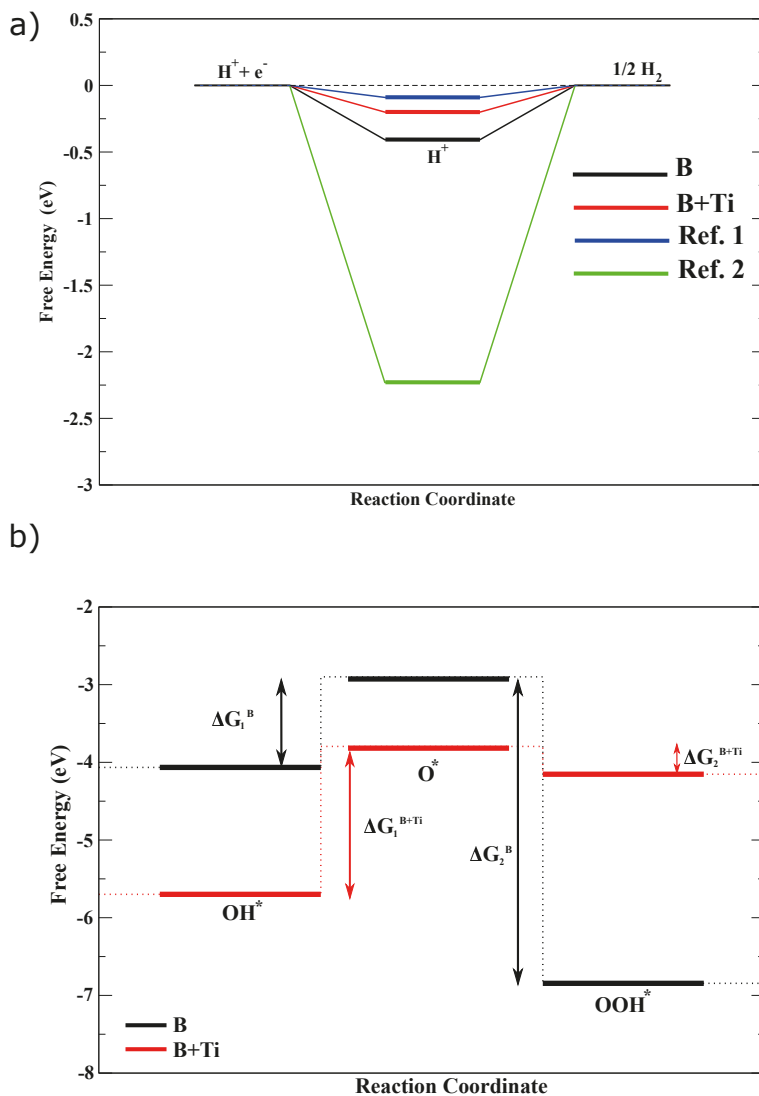


Figure 3.3. Free energy diagram for (a) hydrogen evolution reaction and (b) oxygen evolution reaction at equilibrium on pristine and Ti- functionalized borophene monolayer. Ref. 1 is for 0.25 ML on Pt [40] and Ref. 2 is for other reported 2D borophene sheet [115]. This figure is taken with permission from [105]. Copyright © 2018, American Chemical Society.

one C is coordinated with 4 Al atoms in plane. The unit cell of Al_2C contains one formula unit, i.e. two Al and one C atom. In this study, the effect of substitutional defects in the C -site has been investigated. Various metalloid and non-metal elements close to C atom, such as B , N , P , and S are considered for the mono-substitution [117]. All the optimized systems have come out as stable pristine monolayer without substantial planarity distortion [117]. However, the calculated band gap with PBE type GGA exchange–correlation functional is 0.6 eV for pristine and very narrow gap of 0.1 eV for B substituted case. While the remaining systems are showing metallic character. It is noteworthy to mention that the calculated band gap with PBE-GGA strongly underestimates the band gap. The substantial band gap value could be obtained by using the hybrid exchange–correlation functional. So at this moment it is very hard to select the photocatalytic material from the substituted systems based on the band gap only. However, it has been reported it is possible to show good HER or OER property irrespective of the material's band gap [118, 119].

The main focus of this work is understanding the anionic substitution effect in pristine Al_2C monolayer on the HER and OER activity. Therefore it is important to know how the adsorption energy of the intermediate is changing with different anionic substitution. For HER, adsorption free energy of H^* on the considered catalytic systems are calculated. Although it is well known that in the free energy model for OER constituted with OH^* , O^* , and OOH^* intermediates. Here, the adsorption free energy of O^* is only considered as an intermediate to study part of the OER. More specifically, with a given constant difference between the OH^* and OOH^* adsorption free energy levels, overpotential of OER could be governed by the position of the adsorption free energy level of O^* within that difference [39]. By using Eq. (3.8), the adsorption free energy could be calculated from the adsorption energy of the intermediate with addition of zero point energy and entropic contribution. The correction term is on the order of 0.24 eV and 0.33 eV, respectively for H^* and O^* intermediate [39, 117]. In the calculation, it has been observed that hydrogen adsorption is most favorable at the top site of the C atom and the substituent atoms for pristine and functionalized Al_2C sheet, respectively. On the basis of adsorption energy of the H^* intermediate [117], the adsorption free energies in eV are -0.05, -1.06, 1.13, 1.25, and 1.23 for pristine, B , N , P , and S substituted Al_2C respectively. Therefore at standard condition ($U=0$, $pH=0$, 298 K) the proton transfer is exothermic in pristine and B substituted Al_2C , while it is endothermic in N , P , and S substituted Al_2C . Apart from pristine Al_2C case, only B substituted Al_2C shows very close to thermoneutral, which could be the most promising candidate for HER on Al_2C monolayer. The calculated adsorption free energy of pristine, B , N , P , and S substituted Al_2C are -4.42 eV, -3.39 eV, -2.64 eV, -3.28 eV, and -4.78 eV. So the absorption of the O^* intermediate is more strong in S substituted Al_2C , whereas it is less strongly adsorbed in N substituted Al_2C . This adsorption free energy of the O^* could tune OER activity of the material by controlling the oxidation of

adsorbed hydroxide and formation of adsorbed peroxide. The catalytic activity and electronic properties of pristine and substituted Al_2C monolayer have been discussed elaborately in **Paper II** of this thesis.

3.4 Metal Oxide photocatalyst

3.4.1 Water oxidation in $BiVO_4$ photoanode by W–Ti codoping

Monoclinic $BiVO_4$ is one of the most promising candidates in the search of efficient photoanodes for photoelectrochemical water-splitting. It has optical bandgap of 2.4 eV corresponds to the theoretical conversion efficiency of 9.1%. It also possesses a favorable conduction band edge position for water splitting [120, 121]. So in this study, the mono and co-doping effect of W and W-Ti on photocatalytic efficiency are investigated to support the experimental findings. In this consequence, both bulk and surface structure are considered to envisage the doping effect on OER. It has been observed that the substitution of V by W and also co-doping of W-Ti increase the cell volume of pristine $BiVO_4$ by 0.53% and 0.86% respectively [122]. This change in volume could be attributed to the volume of doped polyhedra that induces distortion in the neighbouring polyhedra. Additionally, the doping does not bring any prominent change in the surface structure of $BiVO_4$ (010) facet as shown in Figure 3.4 a). The density of states of pristine, W-doped $BiVO_4$ and W-Ti codoped $BiVO_4$ depict not much impact on the band gap of pristine $BiVO_4$ (of around 2.0 eV), which is consistent with the light absorption measurement in the experiment [122]. Meanwhile, comparing W mono and W-Ti codoping, there is a very small change in band gap (0.01 eV) [122]. Absence of the trap states (which could act as recombination centers) in the PDOS of W–Ti codoped $BiVO_4$ indicates that W–Ti codoping facilitates the surface catalytic activity without this kind of recombination center [122].

Adsorption energy of the intermediates, OH^* , O^* , and OOH^* are calculated on various sites of $BiVO_4$ surface except the V site. The V-site is not considered as an active site here, since it cannot be further oxidized on a pristine surface [123, 124]. The adsorption energies of OH^* intermediate on Bi atom are -0.90 eV, -2.49 eV and -1.18 eV for pristine, W doped and Ti doped $BiVO_4$ (010) facets respectively. Therefore, the doped surface could greatly improve the adsorption ability especially for the W doped surface. Moreover, the doped atoms in the surface could also act as the active sites on the surface. The calculated Gibbs free energies of the intermediates in different surface sites during the OER process on the $BiVO_4$ (010) surface are shown in Figure 3.4 (b). It could be concluded by comparing the Gibbs free energies on different sites from Figure 3.4 (b), that OER on Ti site is closer to the ideal OER catalyst than other possible sites. It indicates that the Ti site is energetically more favorable for water splitting. The surface catalytic ability could further understand by calculating overpotentials of different surface sites as shown in

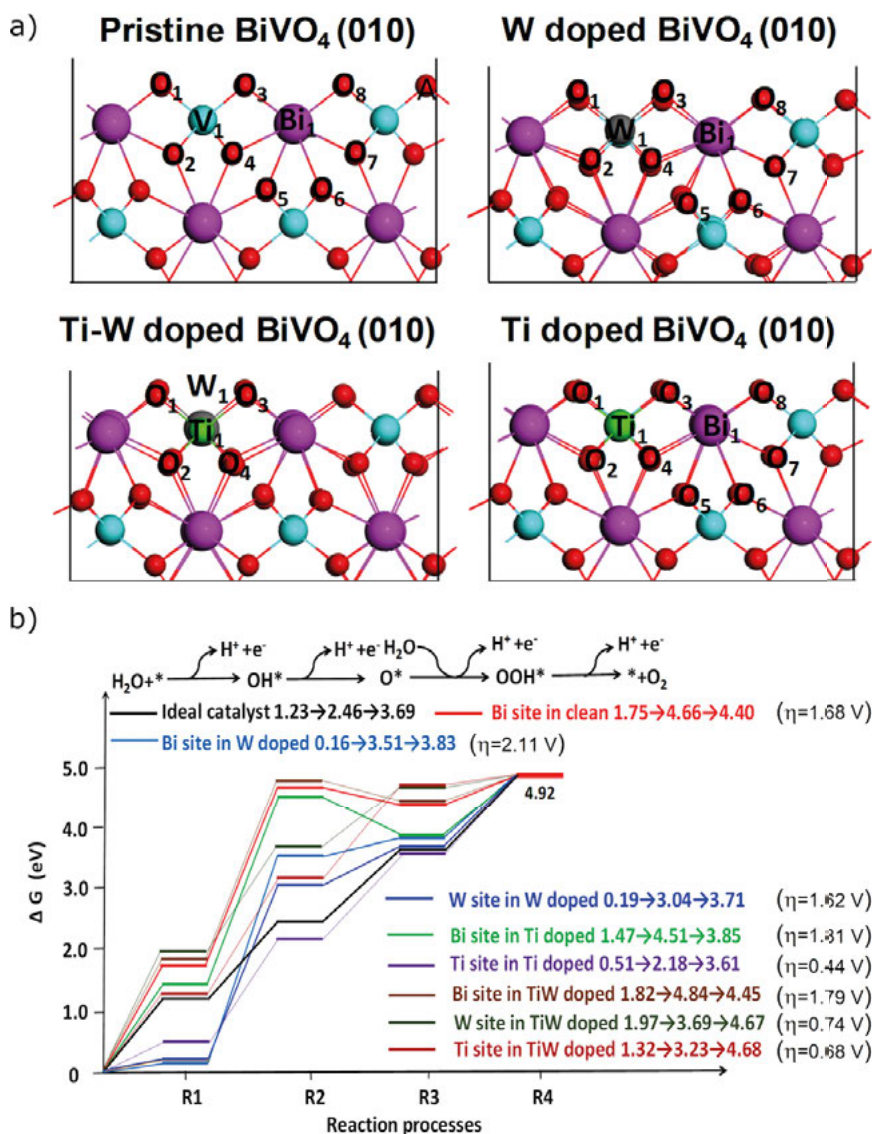


Figure 3.4. (a) The optimized structures of pristine, W doped, W–Ti codoped and Ti doped BiVO₄ (010) facets, where Bi, V, O, W and Ti are shown as purple, gray, red, blue and green spheres, respectively. (c) Free-energy profiles of the OER on different sites of BiVO₄ (010) facet; the black line is for the ideal catalyst. This figure is taken with permission from [122]. Copyright © 2018, The Royal Society of Chemistry.

Figure 3.4 (b). As compared with pristine BiVO₄, not much improvement has been found in the overpotential for Bi or W site. However, the Ti site possesses a lower overpotential in the W–Ti codoped sample (0.68 V). This explains the

experimentally observed photocurrent onset potential shift in W–Ti codoped $BiVO_4$ [122]. Although a further lower overpotential (0.44 V) is found for the Ti site on the Ti doped surface, but the experimentally observed performance is poor [122]. This is mainly due to the fact that the Ti monodoped sample has poor electron conductivity and consumes more voltage to overcome the large resistance. The detailed scenario of doping effect on OER has been explained in **Paper III** of this thesis.

4. Electronic and Optical Properties of Stable Mixed Hybrid Perovskite Solar Cells

In connection to the previous chapter, we have realised that overpotential is one of the most crucial parameters needed to efficiently split the water. In this aspect, hybrid perovskite could be employed to provide that potential, which essentially would produce the solar fuel in a more sustainable way. Organic-inorganic hybrid perovskites have emerged in the last decade with superior properties due to the synergistic effect between the flexible, straightforward-to-synthesize organic part with finely-tunable optoelectronic properties and the thermomechanically stable inorganic counterpart with a high carrier mobility [16, 125, 126]. There have been an enormous amount of research activities are going on to harvest the solar energy efficiently by developing solar cells with high conversion efficiencies [25, 127–130]. The general formula of perovskite is ABX_3 , where A is a organic/inorganic monovalent cation, B is a divalent metal cation and X is a halide anion motif. The crystal structures of the compounds could be classified based on their dimensionality of perovskite frameworks. More specifically it depends on the framework of PbI_3 polyhedra which could be (by corner sharing) extended 3D or 2D layered or 1D infinite chains [131, 132]. Irrespective of the simple hybrid perovskite (which

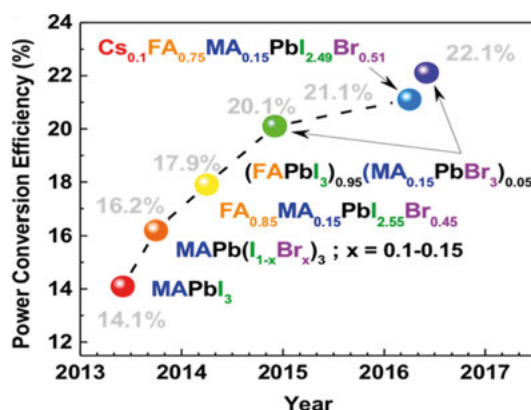


Figure 4.1. Efficiency of recently reported mixed perovskite solar cells including simple perovskite, $MAPbI_3$ certified by NREL [11]. This figure is taken with permission from [133]. Copyright © 2017, American Chemical Society.

composed of only one of the each three species, A , B , and X), currently there is a high predominance of research going on mixed hybrid perovskite (which

composed of more the one of each A , B , and X) [129, 133–135]. In fact, after the first certified record efficiency reported for hybrid perovskite solar cells using pure phase of $MAPbI_3$ [136], the following five National Renewable Energy Laboratory (NREL) records have used A and/or X site mixed hybrid perovskites as shown in Figure 4.1 [11, 133]. The theoretical approaches have been proved as a very efficient predictive tools for exploring the search space for new perovskites or tailoring the perovskites with their desired properties. In the following section, the effect of mixed cation and anion on the electronic properties along with the stability will be discussed.

4.1 Bromine induced thermodynamic stability in mixed-halide perovskite

Various recombination pathways in hybrid perovskites are needed to be suppressed in order to achieve the increased efficiency with less non-radiative carrier loss. The compositional flexibility of ABX_3 materials could be exploited to decrease such non-radiative recombination pathways. With this aim, as a promising “ A ” cation, guanidinium ($GA = [C(NH_2)_3]^+$) has come into the picture to use as an additive in $MAPbI_3$ [137]. The zero dipole moment of GA could influence the bias-induced ionic motion and subsequently the hysteresis behaviour [138]. This ligand has become promising in dye sensitized solar cells (DSSCs) as well [139] with the corresponding enhanced carrier lifetime. However, stability remains an issue in the case of $GAPbI_3$, which needs to be resolved and taken care of. This laid the foundation of this work, where it has been explored whether the stability could be enhanced using the bromination effect through a systematic theoretical investigation.

In order to investigate the stability of the perovskite under bromination, electronic structure calculations have been performed for three different systems – pristine $GAPbI_3$, $GAPb(I_{0.5}Br_{0.5})_3$ (half bromination) and $GAPbBr_3$ (full bromination). In the case of half bromination, the crystal structure with the minimum energy configuration has been confirmed among all the different possible configurations based on symmetrical arrangements of I and Br in Pb octahedra. The optimized structures with the minimum energy configuration are shown in Figure 4.2. For all the three cases, that the organic cation GA mainly acts as a spacer in between the Pb -octahedral chains. Due to the substitution of I with Br in the polyhedra, the orientation of the GA cation changes. This leads to a change in the polyhedral volume of about 24.3% upon transition from PbI_6 to $PbBr_6$, which causes the 5.41% volume change in the unit cell [140]. In case of PbI_6 , the average bond length of the shorter bonds is 3.17 Å and that of the longer ones is 3.26 Å, whereas in the case of $PbBr_6$, the shorter bonds contract to 2.97 Å and the longer bonds contract to 3.09 Å [140]. It is worth mentioning that all of these changes in the case of $GAPb(I_{0.5}Br_{0.5})_3$ are in between the two pure phases [140]. The small difference between ionic

radius of Br (196 pm) and that of I (220 pm) allows the full substitution of I with Br based on the Goldschmidt's empirical rules for elemental substitution.

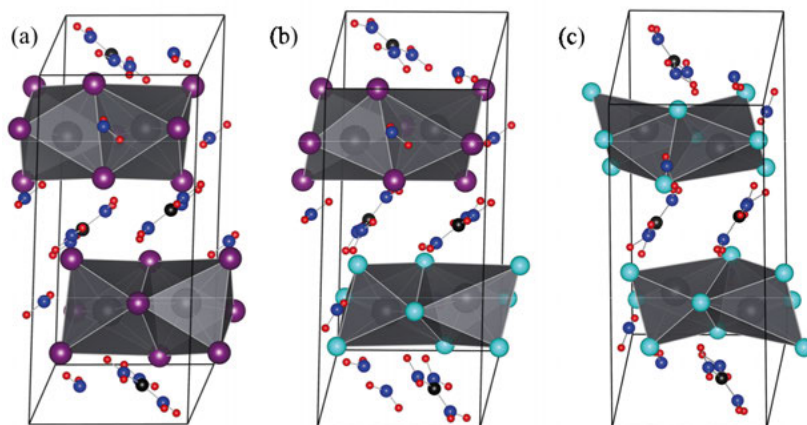


Figure 4.2. Optimized geometries of (a) GAPbI_3 , (b) $\text{GAPb}(\text{I}_{0.5}\text{Br}_{0.5})_3$ and (c) GAPbBr_3 . The black, blue, red, purple and cyan balls represent the C, N, H, I and Br atoms, respectively. The black polyhedra correspond to Pb-polyhedra. This figure is taken with permission from [140]. Copyright © 2017, The Royal Society of Chemistry.

These structural rearrangements with the insertion of bromine into the system tunes the formation energy. This formation energy could lead to the inference of the structural stability, which is one of the prime factors for practical application of guanidinium-based solar cells. The absolute stability of the iodide phase is determined by comparing the electronic energies of the GA cation and the lead iodide anion in a similar unit cell of GAPbI_3 . The formation energy calculation reflects the stability of GAPbI_3 with a formation energy of 5.64 eV per formula unit with respect to the organic cation and the lead iodide anion [140]. Similarly to this thermodynamic entity, the formation energy, also considered to compare the stabilities of the half brominated and fully brominated phases with respect to GAPbI_3 . The calculated formation energy of GAPbBr_3 and $\text{GAPb}(\text{I}_{0.5}\text{Br}_{0.5})_3$ are 0.68 and 0.36 eV with respect to GAPbI_3 respectively. Therefore, we can conclude that the fully brominated system is more thermodynamically stable as compared to the half brominated system. An increase in solar cell stability by replacing I with Br is also being experimentally demonstrated before by Noh *et. al.* [130]. In addition to the formation energy-based prediction of the structural stability in these considered systems, phonon-based stability is envisaged. The mere presence of negative vibrational frequencies is in favour of the stability of the corresponding system, which one could observe in the half and fully brominated

$GAPbI_3$ systems as well. It is noteworthy to mention here, that this stability implies pure structural stability without the interaction of water (moisture). Further investigation of electronic structure and optical responses due to the bromination has been elaborated in *Paper IV* of this thesis.

4.2 Electronic structure and optical response of mixed cation-mixed anion based Hybrid Perovskites

The recent progress in synthesis technique and experimental advancement has led to an unprecedented solar cell efficiency of 22.1% for the mixed cation ($MA=CH_3NH_3$ and $FA=CH(NH_2)_2$) and mixed halide (I/Br) based lead perovskite in the form of $FA_{0.85}MA_{0.15}Pb(I_{0.85}Br_{0.15})_3$ [11, 134]. However, the profound understanding of why this particular type of combination is showing such a great promise from efficiency perspective is still due, which requires the deeper electronic structure analysis. This work has been focussed to theoretically predict the structure of the mixed cation-mixed halide hybrid perovskites compound in an unbiased way. This has been done by mimicking the nearest neighbour structures of the reported $FA_{0.85}MA_{0.15}Pb(I_{0.85}Br_{0.15})_3$ [FMPB] in the form of $FA_{0.83}MA_{0.17}Pb(I_{0.83}Br_{0.17})_3$ [FMPIB1] and $FA_{0.875}MA_{0.125}Pb(I_{0.875}Br_{0.125})_3$ [FMPIB2] that are derived the structural phase space from $FAPbI_3$ [FPI] and $MAPbBr_3$ [MPB] parent compound respectively.

The most stable alpha phase (cubic, $Pm\bar{3}m$) of $MAPbBr_3$ and alpha phase of (trigonal, $P3m1$) $FAPbI_3$, as the parent phases have been considered to perform a systematic investigation to understand the structural variation in mixed phase. Among the many possible factors, the structural transition (polyhedral distortion) due to different size of cation as well as halide anion is an important factor to be considered. In this respect, Goldschmidt tolerance factor (t) is the most reliable empirical index to predict preferentially stable perovskite crystal structure [15]. Based on the effective cation and anion ionic radius, the effective tolerance factor of FPI, FMPI, FMPIB1, MPB, FMPB and FMPIB2 are 1.038, 1.025, 1.029, 0.979, 1.054, and 1.031 respectively. It is worth to mention here that the corresponding octahedral index of FPI, FMPIB1, MPB, and FMPIB2 are 0.464, 0.472, 0.520, and 0.470 respectively. These two factors fall within the acceptable range of 0.8-1.06 and over 0.41 respectively [141]. The tolerance factor index has more pronounced contribution in depicting the contribution of organic cation size and the mechanical stability of the corresponding perovskites systems. Moreover, it is observed that the lower effective tolerance factor is consistent with higher stability [142]. In general, when $t < 0.8$, the hybrid perovskite tends to form orthorhombic structure and when $0.8 < t < 1$, cubic structure is formed. The tolerance factor with the variation of ionic radius is shown in Figure 4.3.

The crystal structures of pristine FPI and the corresponding mixed phase FMPI and FMPIB1 are shown in Figure 4.3. We can observe from Figure 4.3 that Pb-polyhedra is continuing to be shared by the corner halide atoms even with the inclusion of FA and Br. Figure 4.3 also shows the crystal structure evolution from MPB to mixed phase FMPIB2, the random molecular motion generated from AIMD simulation has also been shown. In general, addition or subtraction of larger cation (FA) and anion (I) into the parent phase respectively increases or decreases the Pb-polyhedra volume [143]. Due to the different electronegativity and ionic radius of halide ion, the Pb-X (where X=I, Br) distance does also change. The average Pb-Br bond length in MPB is 2.972 Å, whereas in the mixed polyhedron of FMPIB2 the bond length becomes 3.068 Å. Similarly, the average Pb-I bond length in FPI is 3.171 Å and in mixed phase FMPIB1 the value decreases to 3.162 Å [143]. The band structure of FPI manifests the fact of the direct band gap of 0.26 eV near the vicinity of high symmetry A point [143], which is in reasonable agreement with the reported value [138]. It has been observed that the valence band maxima (VBM) and conduction band minima (CBM) are slightly off centered from the high symmetry point [143], which is due to the relativistic SOC effect due to the presence of heavy element Pb in the system. In terms of the orbital contributions, the hybridization of $I-5p$ (mostly p_z) and $Pb-6s$ is prevailed in VB edge. The CB regime is mostly contributed by $Pb-6p$ orbital with nearly equal contribution of $6p_x$, $6p_y$ and $6p_z$ [143]. In case of mixed cation-mixed halide configuration (FMPIB1), the direct band gap of 0.42 eV is observed at high symmetry Γ point. This band gap increment as compared to FPI is a common phenomenon that has been occurred with the inclusion of smaller Br anion replacing partially the larger I anion [144]. The orbital contributions at band edges are remaining same like FPI, while the $Br-4p$ orbital contributes almost 1 eV below the VBM. The other pristine phase, MPB is showing a direct band gap of 0.83 eV at Γ point [143]. The combined inclusion of FA cation and I anion in the cubic phase of MPB eventually reduces the band gap of FMPIB2 from 0.83 eV to 0.52 eV [143]. However, it retains the VBM and CBM at high symmetry Γ point as in pristine MPB phase. All these band gap variations with respect to the stoichiometry of organic cation and halide anion also imply the change in exciton binding energy, which is one of the governing factors for the photovoltaic efficiencies. This has been happened through the change in Bohr radius and dielectric screening values of different concentration of halogen elements, in this case I and Br. More detail of band splitting along with the optical absorption spectra are discussed in *Paper V* of this thesis.

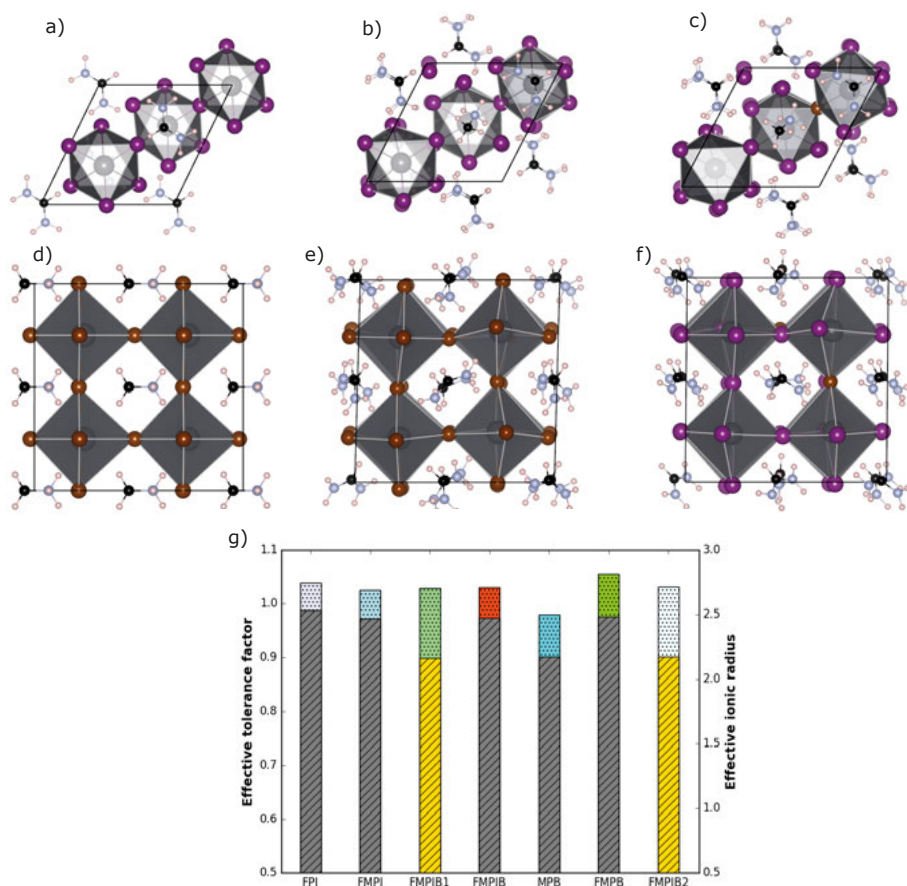


Figure 4.3. Crystal structure of (a) FPI, (b) FMPI, (c) FMPIB1, (d) MPB (e) FMPB (f) FMPIB2. (g) Relation of tolerance factor with ionic radius. Gold Hashed shed for anion radius. Black hashed shed for cation radius. Violet, brown, black, pink, and sky-blue ball represents respectively I, Br, C, H, N atoms. Gray polyhedra represent Pb-polyherda.

Part III:
Energy Storage

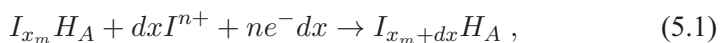
5. Thermodynamics and Kinetics of Battery Materials

The energy storage technology is equally important to successfully utilize the renewable energy resources as well as the energy generation process. In this regard, the rechargeable battery electrodes have shown its potentiality in the application of portable electronic device as well as for transport applications. The quest for the most efficient battery material is still needed to continue to meet the ongoing demand of modern society. In this connection, thermodynamics and kinetics of the battery material are two of the important issues, which will be discussed in this chapter, to understand the stability, potential and active alkali metal ion transport in the battery electrodes.

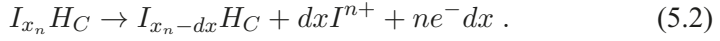
The reversible insertion/de-insertion of alkali metal ion, such as Li or Na into the host (electrode) material is the main feature of the rechargeable battery [145]. Due to the alkali metal ion insertion, it alters not only the host material (crystal) structure but also the electronic structure. It is expected that in the host material this alkali ion fully ionised and donates the electron in the host band. Now the band filling of the host material could be governed by the controlling the alkali metal ion content in the host material electrochemically. The first principles electronic structure calculation can be used to understand the insertion mechanism together with the prediction of the relevant properties of battery electrodes, such as open-circuit voltage (OCV), energy density (E_d), specific energy (E_s), activation energy barrier of alkali ion insertion in the electrode materials.

5.1 Thermodynamics of Ion Insertion in the Electrodes

Electrochemical cell delivers electrical energy upon discharging and consumes energy upon charging. The discharge process could be simulated by considering the system in thermodynamic equilibrium at open circuit condition of the cell. With the initial assumption, we have two host electrodes, H_C and H_A , for cathode and anode respectively. Those electrode will host the guest alkali ion of charge ne in the solution. This means with the flow of n electron in the external circuit one ion could be inserted in the electrode. Guest ion (I) concentration in H_C and H_A is x_m and x_n respectively. Also let us consider that dx is the amount of guest ion inserted and extracted during the charging-discharging process. Insertion reaction during the charging process at the anode is



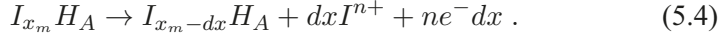
and extraction reaction at the cathode is



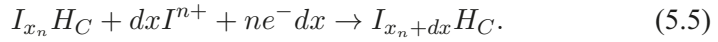
Subsequently the overall reaction will be:



The reaction at the anode in discharging process is as follows:



While at cathode the reaction is:



So the overall reaction will be:



At the open circuit condition, the resistance is infinity, and current becomes zero. Then the work done by the system will be the reversible electric work (W) which is equal to the variation of Gibbs free energy (G) as follows:

$$dw(x) = dG(x) = -V(x)dq = -V(x)nedx , \quad (5.7)$$

where V is the potential difference between H_C and H_A . By definition the Gibbs free energy change of a system at constant temperature (T) and pressure (P) is

$$dG = \sum_{i=1} \mu_i(x)dx_i , \quad (5.8)$$

where μ_i denotes the chemical potential of each species. Using Eq.5.8, the Gibbs free energy variation (dG) during discharge reaction will be:

$$\begin{aligned} dG(x) &= \left[\mu_I^{H_C}(x)dx + \mu_I^{H_A}(x)(-dx) \right]_{T,P} \\ &= \left[\mu_I^{H_C}(x) - \mu_I^{H_A}(x) \right]_{T,P} dx . \end{aligned} \quad (5.9)$$

The OCV of the cell as a function of chemical potential could be obtained by inserting Eq. 5.9 in Eq. 5.7, following the below equation:

$$V(x) = -\frac{\mu_I^{H_C}(x) - \mu_I^{H_A}(x)}{ne} \quad (5.10)$$

The lack of knowledge about the local ordering of the guest ion with continuous change of its concentration in the host structure, brings the difficulties to

compute the Gibbs Energy as a function of x . This is why instead of calculating the $V(x)$ curve, we could compute the average OCV (\bar{V}) by fixing lower and upper insertion limits, x_1 and x_2 respectively. The formulation of (\bar{V}) will be as follows:

$$\begin{aligned}\bar{V} &= \frac{1}{x_2 - x_1} \int_{x_1}^{x_2} dq V(x) \\ &= -\frac{1}{ne(x_2 - x_1)} \int_{x_1}^{x_2} dq \left(\mu_I^{H_C}(x) - \mu_I^{H_A}(x) \right) .\end{aligned}\quad (5.11)$$

We could rewrite Eq. 5.11 by using the definition of chemical potential, $\mu(x) = \left[\frac{\partial G(x)}{\partial x} \right]_{T,P}$ as follows:

$$\begin{aligned}\bar{V} &= -\frac{1}{x_2 - x_1} \int_{x_1}^{x_2} dx \left(\frac{\partial G^{H_C}(x)}{\partial x} - \frac{\partial G^{H_A}(x)}{\partial x} \right) \\ &= -\frac{1}{x_2 - x_1} [(G^{H_C}(x_2) - G^{H_C}(x_1)) - (G^{H_A}(x_2) - G^{H_A}(x_1))] \\ &= -\frac{\Delta G_{reaction}}{x_2 - x_1} .\end{aligned}\quad (5.12)$$

If we consider a metallic anode (e.g. Li or Na, as used in the following studies), where the chemical potential of the anode is constant, then Eq. 5.12 will be as follows:

$$\bar{V} = -\frac{1}{x_2 - x_1} [(G^{H_C}(x_2) - G^{H_C}(x_1)) - (x_2 - x_1)G^{Li/Na}] \quad (5.13)$$

Eq. 5.12 could be reformed as:

$$\bar{V} = -\frac{\Delta E_{reaction} + P\Delta V_{reaction} - T\Delta S_{reaction}}{x_2 - x_1} . \quad (5.14)$$

The contribution of $P\Delta V_{reaction}$ and $T\Delta S_{reaction}$ are very small ($\sim 0.01V$) in the average OCV value [146]. According to this approximation¹, Eq. 5.14 for the average OCV could be rewritten as follows:

$$\bar{V} = -\frac{\Delta E_{reaction}}{x_2 - x_1} . \quad (5.15)$$

Here, $\Delta E_{reaction}$ is the energy difference of the ground state configurations of $H_C(x_2)$, $H_C(x_1)$ and Li/Na metal anode. Energy of the ground state configurations at 0K could be obtained by solving the KS equation. Various global optimization techniques such as, *basin hopping*, *evolutionary algorithm* have been used in the following studies to predict the global optimized structure of the host material.

¹In principle this average OCV equation could be further improved by considering the cluster expansion technique and Monte Carlo simulation. The first will take care to predict any arbitrary configuration with respect to given host (to produce the $V(x)$ curve) and the later one will evaluate finite temperature behavior [146].

5.1.1 Thermodynamics of Na insertion in $\text{Na}_x\text{Fe}(\text{SO}_4)_2$

Eldfellite ($\text{NaFe}(\text{SO}_4)_2$), is a recent addition to the quest for efficient cathode material [147]. Its reversible sodium insertion capability has been observed experimentally at a voltage of 3.2 V versus Na/Na^+ for the $\text{Fe}^{3+}/\text{Fe}^{2+}$ redox activity [147]. This polyanion is displayed a moderate specific energy with lower sodium insertion rate [147]. The specific energy could be tuned by structural modification. In fact one possibility could be the full removal of Na ions from this compound to allow the $2e^-$ redox reaction. It means one redox reaction for no Na to one Na per formula unit (f.u.) of host: $\text{Na}^+ + e^- + \text{Fe}(\text{SO}_4)_2 \rightarrow \text{NaFe}(\text{SO}_4)_2$, and another reaction for one Na to two Na per f.u. of the host: $\text{Na}^+ + e^- + \text{NaFe}(\text{SO}_4)_2 \rightarrow \text{Na}_2\text{Fe}(\text{SO}_4)_2$. The in-depth understanding of the sodium intercalation and extraction process could be unveiled if we have the information of the structures in between full sodiation ($\text{Na}_2\text{Fe}(\text{SO}_4)_2$) and full desodiation ($\text{Fe}(\text{SO}_4)_2$). In this connection, we have explored different sodium concentrations for $\text{Na}_x\text{Fe}(\text{SO}_4)_2$, where $x = 0$ to 2 by varying x at an interval of 0.25. Global structures for all the compositions are obtained using basin-hopping Monte Carlo algorithm by considering more than 300 structures in each case [97].

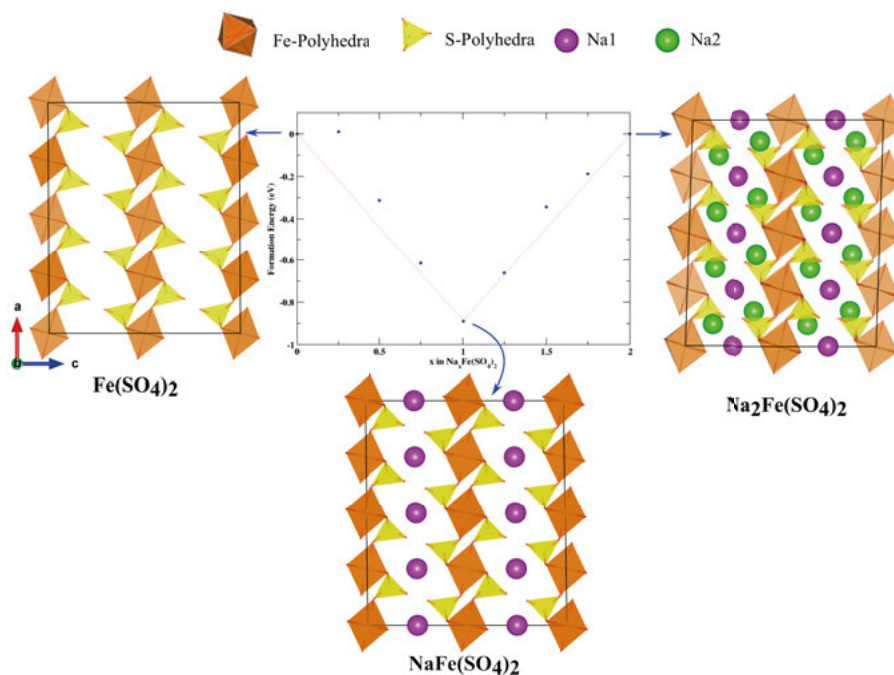


Figure 5.1. Crystal Structures of $\text{Fe}(\text{SO}_4)_2$, $\text{NaFe}(\text{SO}_4)_2$, and $\text{Na}_2\text{Fe}(\text{SO}_4)_2$ with the tie-line plot framed in the middle. This figure is taken with permission from [97]. Copyright © 2016, The Royal Society of Chemistry.

The formation energy of all structures with different Na concentration are calculated by using the following formula:

$$E_f = E_{Na_xFe(SO_4)_2} - \left[\frac{x E_{Na_2Fe(SO_4)_2} + (2-x) E_{Fe(SO_4)_2}}{2} \right], \quad (5.16)$$

where $E_{Na_xFe(SO_4)_2}$ is the calculated energy of the particular structure. Finally the most stable phase in between two end phase, $Fe(SO_4)_2$ and $Na_2Fe(SO_4)_2$ are calculated by constructing convex hull as shown in Figure 5.1. From Figure 5.1, it is clear that only $NaFe(SO_4)_2$ is below the tie-line. It confirms that only $NaFe(SO_4)_2$ is most stable phase among all the predicted structures of different Na concentration in between two end phases. The existence of only this stable phase, $NaFe(SO_4)_2$, ensures two potential plateaus during the cell reaction. The average OCV for sodium intercalation vs Na/Na^+ is calculated by using the following formula similar to Eq. 5.15:

$$\bar{V} = - \left[\frac{E_{Na_xFe(SO_4)_2} - (x - x_0) E_{Na} - E_{Na_{x_0}Fe(SO_4)_2}}{x - x_0} \right], \quad (5.17)$$

where $x = 1$ and $x_0 = 0$ for first sodium intercalation reaction, while $x = 2$ and $x_0 = 1$ for second sodium intercalation reaction and E is the ground state energy of the corresponding system. The calculated potential is shown in Figure 5.2. The first plateau of the voltage profile depicts the potential for first

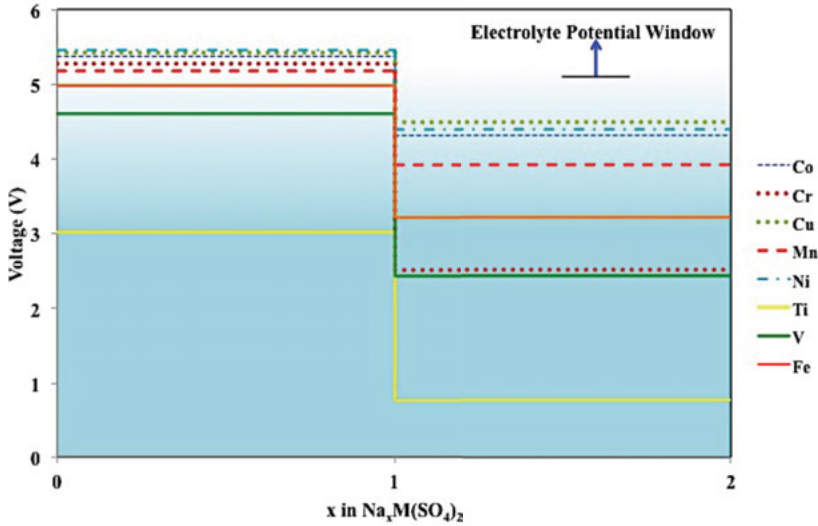


Figure 5.2. Open circuit voltage of the cell with transition metal (M) substitution, where $M = Co, Cr, Cu, Mn, Ni, Ti, V,$ and Fe . This figure is taken with permission from [97]. Copyright © 2016, The Royal Society of Chemistry.

redox reaction, where the sodium ions are removed from $NaFe(SO_4)_2$ to form $Fe(SO_4)_2$. The second plateau of the voltage profile at 3.21 V corresponds

to the redox reaction involved $\text{NaFe}(\text{SO}_4)_2$ and $\text{Na}_2\text{Fe}(\text{SO}_4)_2$ compounds. This intercalation potential value depicts a reasonable agreement with the reported experimental value of 3.2 V [147]. The potential profile for full desodiation is very close to the electrolyte stability window as shown in Figure 5.2, which suggests that it could be unfavorable to remove all sodium. Although the host without any sodium is thermodynamically and dynamically stable [97].

Tuning the redox center i.e. the transition metal atom could be one of the possibility to overcome the above mentioned concern. The effect of transition metal substitution on the potential profile is shown in Figure 5.2. The half-desodiation process for all the transition metal substitution infers, in general, an increasing trend of cell voltage with increasing atomic number of transition metal center. In case of full desodiation process, the change in cell voltage is quite anomalous, does not follow the trend with increasing the atomic number of transition metal. On the basis of electrolyte stability window and the cell voltage, the substitution of Ti and V are more acceptable since these two compounds deliver redox potential values smaller than 5 V during two Na insertion. However, at the same time, the Ti-based system shows very low potential, hence low specific energy for the transition from the +3 to +2 oxidation state, as compared to all the other substitutions. Therefore, V substitution evolves as the most promising candidate to have the reversible two Na ion insertion per redox-center. Moreover, the theoretical specific energy of V-substitution of the order of 689 W h kg^{-1} , which is higher as compared to the currently used cathode LiFePO_4 (440 W h kg^{-1}) [148]. **Paper VII** of this thesis has been detailed the thermodynamics with structural evolution.

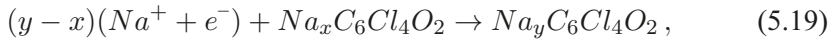
5.1.2 Ion insertion potential and capacity of organic cathode: chloranil

Over couple of years, organic positive electrode redraws the scientific attention along with the conventional transition metal oxides. It is due to their low production cost, environment friendliness, lightweight and easy tunability of the required potential. In this connection, Haegyeom *et. al.* discovered chloranil, $\text{C}_6\text{Cl}_4\text{O}_2$, compound as a cathode for sodium rechargeable batteries [51]. It is a derivative of the p-benzoquinone, where H atoms are substituted with the electron-withdrawing elements chlorine. Due to the high electronegativity of the substituents, the electron density could be displaced out of the molecular center. It results into higher values of the ion insertion potential. The reported average deintercalation voltage is of the order of 2.72 V vs Na/ Na^+ . This reported potential is comparable to the potential of inorganic compounds as in sodium batteries such as NaFeO_2 , having flat voltage profile of 3.3 V vs Na/Na+ related to the $\text{Fe}^{3+}/\text{Fe}^{4+}$ oxidation couple and reasonably higher than the reported values of organic cathode materials for sodium battery application [53]. Thermodynamic analysis of chloranil is important to understand the rea-

son for the insertion of approximately 1.4 Na per formula unit (f.u.) the host material which could yield an energy density of 405 Wh/kg [51]. The sodium ion insertion mechanism in $C_6Cl_4O_2$ could be studied by predicting the crystal structure of the intermediate sodiated phases: $Na_{0.5}C_6Cl_4O_2$, $NaC_6Cl_4O_2$, $Na_{1.5}C_6Cl_4O_2$, and $Na_2C_6Cl_4O_2$. The predicted crystal structures with the Na–O salt region are shown in Figure 5.3. The Na–O salt region in the predicted structures are formed mainly due to rotation of the chloranil molecule as depicted in Figure 5.3. Structural stability of all the predicted structures in terms of formation energy as a function of Na ion concentration are evaluated for the concerning structures using the following equation:

$$E_f = E_{Na_xC_6Cl_4O_2} - \frac{x E_{Na_2C_6Cl_4O_2} + (2-x) E_{C_6Cl_4O_2}}{2} \quad (5.18)$$

where E stands for the total energy of the subscripted compound while x could be as 0.5, 1 and 1.5. The formation energies calculated with PBE and PBE+D2 schemes are shown in Figure 5.4 (a). The compound with Na concentration of $x = 0.5$ appears in the tie-line of the convex hull for the PBE+D2 picture and out of the tie-line for the pure PBE, but with a small energetic distance from the line of the convex hull. On the other hand, the compound with $x = 1$ has emerged as a stable phase for both methods. Finally, the linear combination of the initial and final Na concentration, (where $x = 0$ and $x = 2$) are shown to be more energetically favorable as compared to the case of $x = 1.5$ for both the functional. The formation energies depicted in Figure 5.4 (b) emerge with a different scenario. The HSE06 approach, with different amount of exact exchange, has shown the bottom of the hull in a distinct position if compared with the PBE and PBE+D2 methods. Moreover, it displays the case for $x = 0.5$ out of the convex hull line while the other considered compositions show favorable formation energies. The average (de)intercalation potential vs Na/Na⁺ is assessed by computing the Gibbs free energy of the reaction:



where the difference of y and x being the charge transfers from the Na metal anode to the cathode. The average (de)intercalation potential could be computed as follows similar to Eq. 5.15:

$$\bar{V} = - \frac{E_{Na_yC_6Cl_4O_2} - E_{Na_xC_6Cl_4O_2} - (y-x)E_{Na}}{y-x}. \quad (5.20)$$

The computed potential profile is represented in Figure 5.5. The calculations have taken into account only the compositions lying on the tie-line of the convex-hull. The results appear in quite good agreement with the experimentally measured Na insertion potential, as reported in ref. [51]. First of all, the trend of the two voltage plateaus upon the cell discharge is well reproduced by

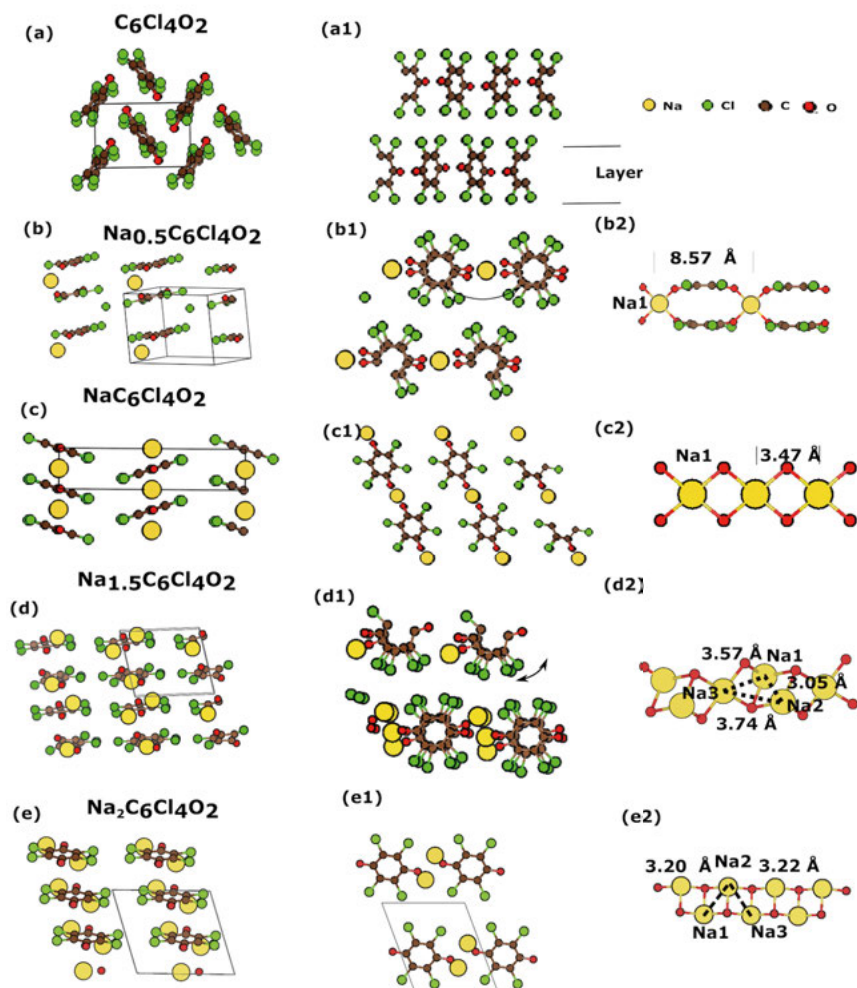


Figure 5.3. Representative picture of the experimental crystal structure of the chloranil (a) together with the most stable phases found by the evolutionary simulation for the compounds (b) $\text{Na}_{0.5}\text{C}_6\text{Cl}_4\text{O}_2$, (c) $\text{NaC}_6\text{Cl}_4\text{O}_2$, (d) $\text{Na}_{1.5}\text{C}_6\text{Cl}_4\text{O}_2$, and (e) $\text{Na}_2\text{C}_6\text{Cl}_4\text{O}_2$. Here, the yellow, red, green, and brown balls represent, respectively, Na atoms, O atoms, Cl atoms, and C atoms. First two columns of the figure depict different orientational views of all structures. The last column presents the changes in the Na–O bonds upon sodium insertion. The bond distances in this picture were computed in the PBE-D2 approach. This figure is taken with permission from [53]. Copyright © 2017, American Chemical Society.

theoretical prediction the different flavors. For the reaction, where x in Na_x is varying from $x = 0$ to $x = 1$, the reported experimental potential is 2.9 V vs

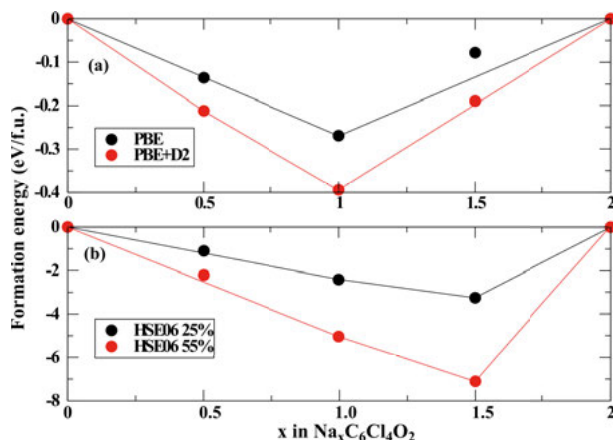


Figure 5.4. Formation energies as a function of x in eV/f.u. with (a) PBE and PBE+D2 and (b) HSE06 with 25% of exact exchange and HSE06 with 55% of exact exchange. The formation energies were computed considering the ground state structures found in the evolutionary simulation. This figure is taken with permission from [53]. Copyright © 2017, American Chemical Society.

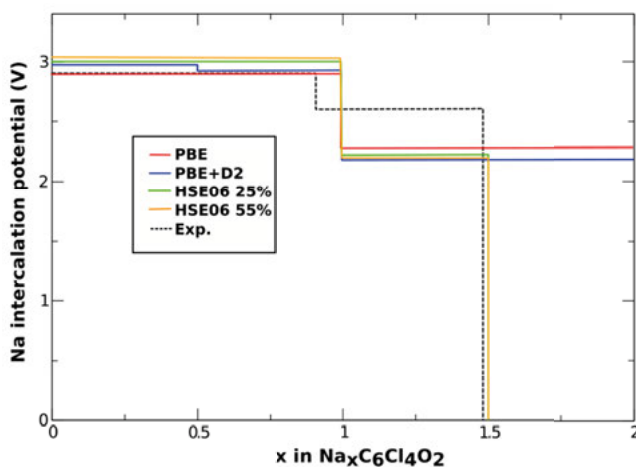


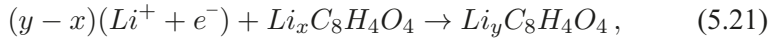
Figure 5.5. Calculated voltage profile of $\text{Na}_x\text{C}_6\text{Cl}_4\text{O}_2$ vs Na/Na^+ for x varying from 0 to 2. The dashed line represents the experimental values of 2.9 and 2.6 V [51]. The red line is the calculations with PBE, the blue line represents the calculations with PBE+D2, and the green line is the calculations with HSE06 with 25% of exact exchange and orange is the HSE06 with 55%. This figure is taken with permission from [53]. Copyright © 2017, American Chemical Society.

Na/Na^+ . The computed values are showing a range from 2.88 to 3.11 V vs Na/Na^+ depending on the used exchange–correlation functional. It depicts a maximum discrepancy of 7% for the HSE06 with 55% of exact exchange and less than 1% of the PBE functional. Experimentally the second voltage plateau

is obtained on a potential of 2.6 V vs Na/Na⁺. In this region of ionic concentration, the predicted Na insertion potential presents a discrepancy of about 9.6% when PBE is employed as the exchange–correlation functional as compared to the measured data. The addition of the long-range interactions with the PBE+D2 should emerge for better results since it can properly describe the related structural properties. However, no real improvement is obtained for the computation of the ion insertion potential with this method in comparison with the pure PBE. A similar result is also reported by T. Yamashita *et. al.* [149]. In fact, the discrepancies between the experimental potential and the computed potential with the HSE method yields greater values as compared to the case with the pure PBE. On the other hand, the inclusion of a percentage of exact exchange in the calculation induces the Na insertion to a maximum concentration of $x = 1.5$ (since the insertion potential goes to a negative value for x going from 1.5 to 2). This result is in really good agreement with the experimental measurement, which prescribes a maximum reversible Na concentration of $x = 1.42$ during the cell reaction [51]. So it is confirmed that ion insertion potential in chloranil could be predicted by PBE level theory, whereas the specific capacity of chloranil by HSE level theory. The detail of the thermodynamics of chloranil with respect to different level of theory is discussed in *Paper X* of this thesis.

5.1.3 Thermodynamics of Li-based organic anode: Terephthalate

The conjugated dicarboxylate family has emerged as a promising negative electrode for advanced Li-ion batteries due to the thermal stability, high charge storage capacity and rate capability and high cyclability [54]. For instance, di-lithium terephthalate, $Li_2C_8H_4O_4$ (denoted as Li_2TP), has recently been studied as an alternative to the currently used materials [150]. This compound showed reversible Li intercalation at 0.8 V vs. Li/Li⁺ and specific capacities of 300 mAh/g. Although, experimentally it has been observed that this Li intercalation is a kind of disproportionation reaction, since two redox reactions (for 2 e⁻ transfer) occur simultaneously at same potential. The average (de)intercalation potential vs. Li/Li⁺ is obtained by computing the Gibbs free energy of the reaction:



where the difference of y and x is the charge transfer from the Li metal anode to the cathode. The average (de)intercalation potential could be computed by using the following equation similar to Eq. 5.15:

$$\bar{V} = - \frac{E_{Li_yC_8H_4O_4} - E_{Li_xC_8H_4O_4} - (y - x)E_{Li}}{y - x}. \quad (5.22)$$

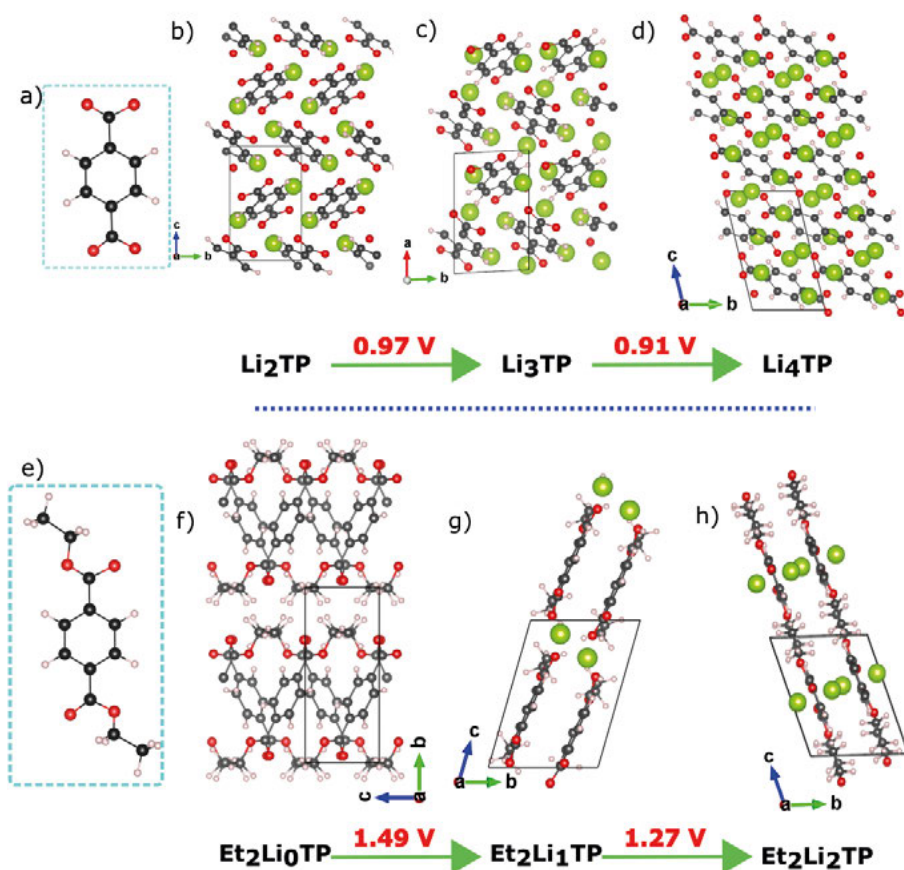


Figure 5.6. Crystal structure of (b) Li_2TP , (c) Li_3TP , (d) Li_4TP , (f) $\text{Et}_2\text{Li}_0\text{TP}$ (g) $\text{Et}_2\text{Li}_1\text{TP}$ and (h) $\text{Et}_2\text{Li}_2\text{TP}$. Molecular structure of (a) terephthalate (TP) and (e) ethylene protected TP. The green, black, red and light pink balls are representing respectively Li, C, O, and H atoms. This figure is taken with permission from [54]. Copyright © 2018, Elsevier.

The redox potential is one of the most important characteristics of electrode materials for battery. The initial step to compute the Li potential profile, is to verify the chemical stability of the intermediated phases. To study the reason of disproportionation reaction, capped TP molecule is used, where one of the redox centers is blocked by the hydrocarbon (HC) chain. Moreover, to account the effect of capping with the HC chain length, different HC, such as methyl (*Mt*) and ethyl (*Et*) are considered. Therefore the intermediated phases are Li_3TP , $\text{Et}_2\text{Li}_1\text{TP}$ and $\text{Mt}_2\text{Li}_1\text{TP}$ with respect to the initial and final states. Li_3TP , $\text{Et}_2\text{Li}_1\text{TP}$ and $\text{Mt}_2\text{Li}_1\text{TP}$ are emerged with formation energies of -0.03 eV, -0.11 eV and -0.15 eV per f.u., respectively. It means that both the compounds are lower in energy than the proportional

linear combination of initial and final states. So the calculation of the redox profile needs to consider these compositions in Eq. 5.22. The mono-lithiation and di-lithiation of Li_2TP leads to potentials of 0.97 V vs. Li/Li^+ and 0.91 V vs. Li/Li^+ respectively. The average potential is 0.94 V vs. Li/Li^+ , which is in good agreement with the experimental potential of 0.8 V [150]. This discrepancy, of the order of 0.14 V vs. Li/Li^+ , between the theoretical and experimental potential is also reported in the literature [149]. It is noteworthy that the predicted potentials of Li_2TP show close to single plateau with a small discrepancy of only 0.06 V whereas the ethylene capped TP shows completely distinguishable redox potential with a clear two-step for two redox reactions. The computed potentials are 1.49 V vs. Li/Li^+ , for Et_2Li_0TP to Et_2Li_1TP reaction, and 1.27V Li/Li^+ , for Et_2Li_1TP to Et_2Li_2TP reaction. Therefore, it could be concluded that with the protection group (the HC chain e.g. Mt , Et) the disproportionation redox reaction (as observed experimentally for Li_2TP) will be lost and replaced by two distinct reduction processes. In Mt capped case, the computed potentials are 1.54V vs. Li/Li^+ , for Mt_2Li_0TP to Mt_2Li_1TP reaction, and 1.24 V vs. Li/Li^+ , for Mt_2Li_1TP to Mt_2Li_2TP reaction.

Therefore, the main characteristics of the potential profile presented by Et capped TP are revealed for the Mt capped TP compound. It indicates that changing the capped group in the TP molecule to another aliphatic group does not bring back the disproportionation reaction observed in the reaction with Li_2TP . The detailed insight of the disproportionation is thoroughly studied in **Paper XI** of this thesis.

5.2 Diffusion kinetics of the guest ion

The guest ion, Li or Na ion diffusion in the host material is an important factor to define the rate performance of the battery. Fast diffusion of the alkali guest ion is also prime concern to deliver the electric current efficiently for high power performance. The diffusion trajectories as well as the diffusion mechanism of the alkali ion could be determined from *ab initio* molecular dynamics (AIMD) simulation. The diffusion coefficient could be obtained from the individual atomic position as a function of time, which is referred as the mean square displacement (MSD). The MSD could be expressed as follows:

$$MSD = \langle |\mathbf{R}(t) - \mathbf{R}(0)|^2 \rangle \quad (5.23)$$

$$\cong \frac{1}{t_{max}} \sum_{i=1}^N \sum_{t_0=0}^{t_{max}} |\mathbf{R}_i(t + t_0) - \mathbf{R}_i(t_0)|^2. \quad (5.24)$$

Here $\langle \dots \rangle$ defines the time averaging over all the atoms. The positions of i^{th} atom at time $(t + t_0)$ and t_0 is specified by $\mathbf{R}_i(t + t_0)$ and $\mathbf{R}_i(t_0)$ respectively.

t_{max} is the maximum time taken in the time-average. The linear regime of the MSD could be fitted by the Einstein relation for three dimension system as follows:

$$MSD = 6Dt + C, \quad (5.25)$$

where C and D are the constant. The constant D is denoted as diffusion coefficient, which depicts how long an atom would travel within a given time on average.

5.2.1 Ionic diffusion in $\text{Na}_x\text{Fe}(\text{SO}_4)_2$

Eldfellite has been stabilized within the monoclinic prismatic crystal class having a space group $C2/m$. From the crystal structure, it has been observed that the Na^+ and Fe^{3+} cations are arranged in a different ab plane and alternatively propagated along the c direction. The six-oxygen coordinated Fe-polyhedra, FeO_6 , are linked with the neighboring SO_4 tetrahedra by their shared polyhedral vertex oxygen atom. Therefore, each FeO_6 octahedra is connected with six SO_4 tetrahedra. Polyhedral arrangement inside the crystal suggests the Na ion diffusion could be happened in between the polyhedral layers.

To have the proper justification, along with the insight of Na diffusion, AIMD simulation has been performed for 50 ps with the time step of 2 fs. Subsequently, the diffusion path has been further analysed with NEB method. For AIMD simulation, temperature variation of 900, 1000, 1100, 1200, 1300 and 1500 K has been considered to accelerate the dynamic process in the canonical ensemble (NVT implies fixed particle number, volume, and temperature). The trajectories of the sodium atoms during AIMD are shown in Figure 5.4 (a). This trajectories suggest that the diffusion of sodium ions is mostly happening in between the planes formed by the S–Fe–S polyhedra in the $\text{Na}_2\text{Fe}(\text{SO}_4)_2$ crystal structure. At the same time, Na ion trajectories do not cross the polyhedral layers due to the strong electrostatic repulsion in the layer.

The Na trajectories reveal the primary diffusion mechanism that has been occurred through hopping between the Na1 positions to the Na2 positions. Subsequently, when the ion is at the Na2 position, it can come back to Na1 or even move to a Na3 position, as is shown in Figure 5.7 (a). The Arrhenius plot for diffusion coefficients at temperatures of 900, 1000, 1100, 1200, 1300 and 1500 K for Na ion diffusion is shown in Figure 5.7 (b). The slope of this plot is the activation energy, which could be obtained by the Arrhenius relation:

$$D = \nu \exp^{-\frac{E_a}{k_B T}}, \quad (5.26)$$

where D is the diffusion coefficient and E_a is the activation energy barrier. The activation energy barrier according to the Eq. 5.26 is 0.58 eV. Consequently, the average activation energy barrier of Na1–Na2 path and Na2–Na3

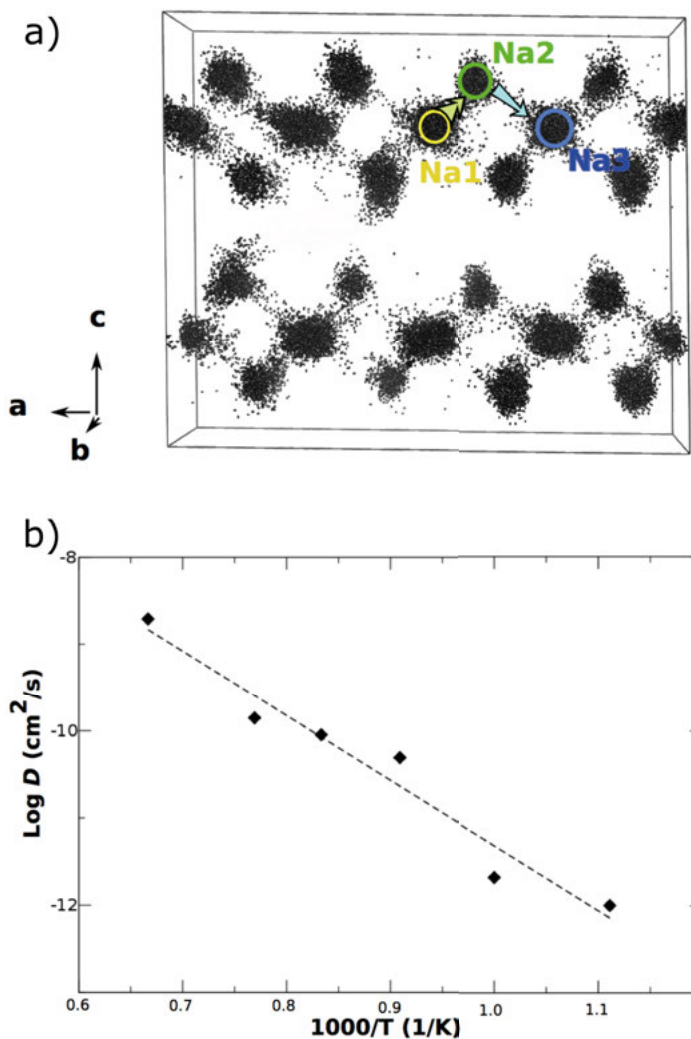


Figure 5.7. (a) Na ion trajectories over the simulated time scale at 1500 K. (b) Arrhenius plot for $\text{Na}_2\text{Fe}(\text{SO}_4)_2$. This figure is taken with permission from [97]. Copyright © 2016, The Royal Society of Chemistry.

from NEB method is 0.64 eV, which is very close to the activation energy barrier calculated from the AIMD simulation.

Within the specified duration of the AIMD simulation, it does not show any atomic diffusion of Na in the half-sodiated phase, $\text{NaFe}(\text{SO}_4)_2$. The cNEB calculations have been carried out for the half-sodiated phase in order to have a full picture of the diffusion process. Two different possibilities are considered here: diffusion with (i) the mono vacancy, and (ii) divacancy of Na. The first approach depicts an activation energy barrier in the order of 1.15 eV, whereas

the second mechanism delivers the activation energy is in the order of 1.13 eV. Therefore both of this approach implies that the migration of Na^+ ions in $\text{NaFe}(\text{SO}_4)_2$ must not be mediated by any of them. This also indicates very poor reaction rate in the half-sodiated phase. More details of diffusion kinetics have been described in *Paper VII* of this thesis.

6. Summary and Future Outlook

Since the last few decades, it has been realized that global warming could be a serious warning to the extinction of civilization. The consequence of this serious threat has convinced and motivated most of the nations throughout the world to find out the way against the raise of average temperature of the world. One highly potential option could be lowering and eventually nullifying the carbon footprint from the fossil fuel. This would be possible by effectively and efficiently using renewable energy instead of the non-renewable energy. Regarding this aspect, materials modeling is a prime choice to identify the potential materials to harvest and store the renewable energy by exploring the search space theoretically.

In this thesis, *ab initio* density functional theory along with molecular dynamics and global optimization methods are used to unveil and understand the material specific structure and properties. This thesis is focused on proposed “green energy cycle” (in the *Introduction* of this thesis), while understanding the insight from the energy production to the storage. The energy production part has mainly discussed about the electrocatalyst for solar fuel production in terms of water splitting and the solar cell to supply the over potential for water splitting. Subsequently, the energy storage part is discussed to store the energy electrochemical in the battery.

Chapter 3 of this thesis have envisaged the hydrogen evolution and oxygen evolution reactions (HER and OER) on two-dimensional (2D) monolayers based on first-principles electronic structure calculations. The effect of Ti functionalization on borophene monolayer has been investigated from the perspective of HER and OER activities enhancement. These activities have been probed based on the reaction coordinate, which is conceptually related to the adsorption free energies of the intermediates of HER and OER. The Ti-functionalized borophene has been emerged as a promising material for HER and OER mechanisms. Further on the series of this noble metal free monolayer catalyst, 2D borophene and Al_2C monolayer has been investigated for HER and OER. Along with the pristine Al_2C monolayer, the system functionalized with Nitrogen (N), Phosphorous (P), Boron (B), and Sulphur (S) have also investigated. After determining the individual adsorption energy of hydrogen and oxygen on the different functionalized Al_2C monolayers, the adsorption free energies are predicted for each of the functionalized monolayers in order to assess their suitability for HER and OER. The corresponding electronic properties together with the free energy model of the functionalized Al_2C monolayers enable to gain a profound understanding of the individual

system and their relation to the water splitting mechanism. The efficient charge separation of photo-generated electrons and holes is critical to achieve high solar energy to hydrogen conversion efficiency in photoelectrochemical (PEC) water splitting. The n-type doping is generally used to improve the conductivity by increasing the majority carrier density while enhancing simultaneously the charge separation in the photoanode. For probing this phenomena, n-type doping (W) in $BiVO_4$ has been considered, which is further codoped with Ti. The determined adsorption energy and corresponding Gibbs free energies depict that the Ti site is more energetically favorable for water splitting. Moreover, the Ti site possesses a lower overpotential in the W–Ti codoped sample as compared to the mono-W doped sample.

The effect of mixed cation and mixed anion substitution in the hybrid perovskite has been discussed in *Chapter 4*. It has been shown that the insertion of bromine (Br) into the system could modulate the stability of the Guanidinium lead iodide ($GAPbI_3$) hybrid perovskite. Further the structural integrity of the mixed cation and mixed anion in the perovskite crystal structure is investigated behind the record efficiency of the recently reported hybrid perovskite based solar cell, $FA_{0.85}MA_{0.15}Pb(I_{0.85}Br_{0.15})_3$, $FA_{0.83}MA_{0.17}Pb(I_{0.83}Br_{0.17})_3$ and $FA_{0.875}MA_{0.125}Pb(I_{0.875}Br_{0.125})_3$, two compositions are considered for the study, which are closest to the reported one. These two structures are derived from $FAPbI_3$ and $MAPbBr_3$ parent compound respectively. It has been observed that the Goldschmidt tolerance factor (t) and octahedral index of mixed phases are within the acceptable range of 0.8-1.06 and over 0.41 respectively. This lower effective tolerance factor is consistent with the enhanced stability. There is an increment in the band gap with the inclusion of smaller bromine anion by replacing partially the larger iodine anion.

The subsequent *Chapter 5* is devoted to understand the electrochemical storage mechanism for sodium (Na) and lithium (Li) ion insertion in the electrode materials. For this purpose, both inorganic electrode (eldfellite, $NaFe(SO_4)_2$) and more sustainable organic electrode (di-lithium terephthalate, Li_2TP) are considered. The mineral eldfellite is one of the recently proposed inexpensive cathode materials for Na-ion based batteries. Density functional theory framework has been used to investigate the phase stability, electrochemical properties and ionic diffusion of this eldfellite cathode material. The crystal structure of eldfellite undergoes a volume shrinkage of $\sim 8\%$ upon full removal of Na ions while showing no imaginary frequencies at the Γ point of phonon dispersion. This evokes the stability of the host structure. It has suggested the possibility to get higher specific energy by inserting two Na ions per redox-active metal. The main bottleneck for the application of eldfellite as a cathode is the high activation energies for the Na^+ ion diffusion, which could be higher than 1 eV for the charged state. This higher activation energy produces a lower ionic insertion rate. The key factor, which is the variation of Li-O coordination in the terephthalate, for the disproportionation redox reaction in Li_2TP is identified using the density functional theory. This governs the stability of

the intermediate phase with respect to the terminal phase in the two electrons redox reaction. The phase stability in terms formation energy obtained from the electronic energy eventually also controls the open circuit voltage, hence the possibility of appearance or disappearance of disproportionation redox reaction.

Finally, we have concluded that, in this thesis, density functional theory driven materials modelling for the application from energy production to the energy storage has been elucidated in a nutshell. In this context, this thesis has depicted how the various probing methods could be used to understand structures driven properties for the application of energy materials. These all together would efficiently explore the renewable energy materials to make more sustainable and green environment.

7. Svensk sammanfattning

Under de senaste årtiondena har det uppmärksammats att global uppvärmning kan vara ett allvarligt hot mot civilisationen. Konsekvensen av detta hot har övertygat och motiverat de flesta länderna i världen att finna ett sätt att motverka ökningen av jordens medeltemperatur. En möjlig lösning skulle kunna vara en minskning och slutligen nullifiering av koldioxidutsläpp från fossila bränslen. Det här kan bli möjligt genom en effektivisering av och genom att använda förnybar energi istället för icke-förnybar energi. I det här avseendet är materialmodellerande ett prima exempel på hur man kan identifiera lovande material, som kan användas för att producera och lagra förnybar energi genom att söka igenom och testa olika material teoretiskt.

I den här avhandlingen har ab initio densitetsfunktionalteori tillsammans med molekylärdynamik och globala optimeringsmetoder använts för att upptäcka och förstå materialets specifika struktur och egenskaper. Den här avhandlingen fokuserar på idén ”grön energicykel” (i Introduktionen av den här avhandlingen), genom förståelse av energiproduktion till lagringen av energin. Energiproduktionensdelen handlar mestadels om elektrokatalysm, för soldriven bränsleproduktion i termer av vattensplittring och solcellen för tillförsel av potentialen, nödvändig för vattensplitting. Vidare handlar energilagringensdelen om hur energin lagras elektrokemiskt i batteriet.

I Kapitel 3 berättas om hydrogen evolution och oxygen evolution reactions (HER och OER), vätgas och syrgasproduktion på tvådimensionella (2D) monolager baserade på första princip-elektronstrukturberäkningar. Effekten av Ti-funktionalisering av borofenmonolager har undersökts från perspektivet av ökad HER- och OER-aktivitet. De här aktiviteterna har testats enligt reaktionskoordinaterna, vilka är begreppsmässigt relaterade till den fria energin hos mellanprodukterna i HER och OER. Det Ti-funktionaliserade borofenlagret har visat sig vara ett lovande material i HER- och OER-mekanismen. Vidare i raden av den här ädelmetallsfria monolagerskatalysatorn, borofen, har Al_2C 2D-monolager undersökts för HER och OER. Tillsammans med det rena Al_2C -monolagret har även system funktionaliserade med kväve (N), fosfor (P), bor (B) och svavel (S) undersökts. Efter att ha bestämt de individuella adsorptionsenergierna för väte och syre på de olika funktionaliserade Al_2C -monolagrena, beräknas den fria adsorptionsenergin för varje funktionaliserat monolager för att kunna bedöma deras lämplighet för HER och OER. Med motsvarande elektroniska egenskaper tillsammans med den fria energimodellen hos de funktionaliserade Al_2C -monolagren kunde djupgående förståelse av de individuella systemen och deras relation till

vattensplittringsmekanismen erhållas. Effektiv laddningsförskjutning av fotogenererade elektroner och hål är nödvändig för att erhålla ett högt solenergi-vätmvandlingsratio i en fotoelektrokemisk (PEC) vattensplittring. N-dopning används generellt för att förbättra ledningsförmågan genom att öka majoritetsbärardensiteten och på samma gång expandera laddningsförskjutningen i fotoanoden. För att undersöka detta fenomen har n-dopning i $BiVO_4$ testats, vilket också dopades med Ti. Fastställd adsorptionsenergi och motsvarande Gibbs fria energi visar att Ti-adsorptionsstället är energimässigt favoriserat för vattensplittring. Dessutom har det W-Ti-dopade provet lägre "overpotential" jämfört med provet endast dopat med W.

Effekten av utbytet av mixad katjon och mixad anjon i hybridperovskit diskuteras i kapitel 4. Det visades att insättandet av brom (Br) i systemet kunde variera stabiliteten hos Guanidiniumblyjodidhybridperovskit. Vidare undersöktes den strukturella hållfastigheten hos den mixade katjon och den mixade anjonen i perovskitkristallstrukturen, vilken nyligen rapporterades från en hybridperovskitbaserad solcell, $FA_{0.85}MA_{0.15}Pb(I_{0.85}Br_{0.15})_3$.

$FA_{0.83}MA_{0.17}Pb(I_{0.83}Br_{0.17})_3$ and $FA_{0.875}MA_{0.125}Pb(I_{0.875}Br_{0.125})_3$, två kompositioner är inkluderade i studierna, som ligger närmast den rapporterade. Det här två strukturerna är framställda från respektive $FAPbI_3$ - och $MAPbBr_3$ -moderförening. Det observerades att Goldschmidt-toleransfaktorn (t) och det oktaediska indexet för mixade faser ligger inom rimliga respektive gränser 0.8-1.06 och över 0.41. Den lägre effektiva toleransfaktorn är konsistent med ökad stabilitet. Bandgapet ökar med integrering av den mindre bromanjonen genom utbyte med den i viss mån större jodidanjonen.

Vidare är kapitel 5 avsatt för att förstå den elektrokemiska lagringsmekanismen för natrium- (Na) och litium- (Li) joninsättning i elektrodmaterial. Både den inorganiska elektroden eldfellite ($NaFe(SO_4)_2$) och den mer hållbara organiska elektroden dilithiumterephthalate (Li_2TP) prövas. Mineralen eldfellite är ett av de nyligen lanserade billiga katodmaterialen i Na-jonbaserade batterier. Ramverket från densitetsfunktionalteorin användes för att undersöka fasstabiliteten, elektrokemiska egenskaper och jondiffusion hos detta eldfellitekatodmaterial. Kristallstrukturen hos eldfellite minskar sin volym med ungefär 8% vid total borttagning av Na-joner och saknar imaginära fonondispersionsfrekvenser i Γ -punkten. Detta bidrar till stabiliteten hos värdstrukturen. Detta gör det möjligt att få en högre specifik energi genom insättningen av två Na-joner per redoxaktiv metall. Den huvudsakliga flaskhalsen hos användandet av eldfellite som katod är de höga aktiveringsenergierna hos Na^+ -jondiffusionen, vilka kan vara högre än 1 eV i den laddade fasen. Den höga aktiveringsenergin bidrar till ett lägre joninsättningsratio. Den avgörande faktorn, vilken är variationen av Li-O-koordinationen hos terephthalate för disproportionationredoxreaktionen i Li_2TP , är identifierad med hjälp av densitetsfunktionalteorin. Detta styr stabiliteten hos mittenfasen med avseende på den slutgiltiga fasen i tvåelektronsredoxreaktionen. Fasstabiliteten i termer av bildningsenergi framtagen av elektroniska energin, kontrollerar slutligen också spännin-

gen, med andra ord sannolikheten för förekomsten eller försvinnandet av disproportionationreaktionen.

Slutligen i den här avhandlingen har vi kommit till, att densitetsfunktionsteoridrivna materialmodellering för applikationer från energiproduktion till energilagring har klargjorts in i minsta detalj. I det här avseendet har den här avhandlingen visat hur olika testmetoder kan användas för att förstå strukturdrivna egenskaper för energimaterialapplikationer. Allt tillsammans skulle på ett effektivt sätt kunna utforska material för förnybar energi, för att åstadkomma en hållbarare och grönare miljö.

8. Acknowledgments

This thesis is the outcomes of the last few years of work, not only by me but also all of you who have helped and supported me in various ways. Therefore I would like to thank all of those people.

Prof. Rajeev Ahuja, for giving me the opportunity to start my Ph.D. in the materials theory division. Especially for supporting my research both mentally and academically. Erasmus Mundus for awarding me the EMINTE fellowship, which not only provide financial support for my Ph.D. but also give me the opportunity to see the world outside of my country. My co-supervisors, Prof. Gunnar Niklasson and Dr. Sudip Chakraborty, for their endless support to review my study plan and to overcome various difficulties in my research from time to time. Rafael, one of my colleague and my first collaborator too, who helped to publish my first paper as a first author after long struggling. Thanks to also my all of other colleagues including Vivek, Emil, Naresh; especially, Non, John for discussing and solving many things in our lunch table! I would like to thank all of my other collaborators Tomas Edvinsson, Zhen, Martin Sjodin, Moyses Araujo, Bertrand, Malin, Håkan Rensmo, for providing excellent experimental support. A special thanks Sudip-da, Anton, Soumyajyoti-da, Ritwik, Kate, John, Non, Ajita for their endless support to critically read and comment on my thesis. I want to express a heartily thanks to Prof. Kantesh Balani, who always encouraged me in my tough time. My family, all of you, for your warm support, most of all my parents and my sister for your patience and encouragement. Really thankful to Suhas's family for providing food in my busy time and Ritwik to provide me accommodation for the first few days in Uppsala. Soumyajyoti-da (Captain) for arranging some exciting trip as well as many outings in Uppsala. And special thanks to my other friends for encouraging me in various ways: Ajita, Ambrin, Anshul, Bhaskar-da, Cherry, Cristina, Deepesh, Fairoja, Nishant, Rahul, Ravi, Sayani,...may be I am missing some name here. Finally, I would like to thank everyone who thought the thesis looked interesting enough to read.

References

- [1] International Energy Agency. *World Energy Outlook 2011*. OECD Publishing, Paris, 2011.
- [2] World Bank. *Guide to Climate Change Adaptation in Cities*. Science, 2011.
- [3] S. Shafiee and E. Topal. *When will fossil fuel reserves be diminished?* Energy Policy, 37(1):181–189, 2009.
- [4] R. Lindsey. *Climate and earth’s energy budget: Feature articles*, 2010.
- [5] BP. *Statistical Review of World Energy*, 2016.
- [6] IEA. *Key World Energy Statistics 2015*. Technical report, 2015.
- [7] I. Mora-Seró. *How Do Perovskite Solar Cells Work?* Joule, 2(4):585–587, 2018.
- [8] W. Ke, G. Fang, J. Wan, H. Tao, Q. Liu, L. Xiong, P. Qin, J. Wang, H. Lei, G. Yang, M. Qin, X. Zhao, and Y. Yan. *Efficient hole-blocking layer-free planar halide perovskite thin-film solar cells*. Nature Communications, 6, 2015.
- [9] Y. Jin and G. Chumanov. *Solution-Processed Planar Perovskite Solar Cell Without a Hole Transport Layer*. ACS Applied Materials & Interfaces, 7(22):12015–12021, 2015.
- [10] A. Chodos. *April 25, 1954: Bell Labs Demonstrates the First Practical Silicon Solar Cell*. APS News-This month in Physics history, 2009.
- [11] NREL. *Solar Cell Efficiency Chart*. Solar Cell Efficiency Chart, 1(1), 2017.
- [12] R. Blandford and M. Watkins. *This Month in Physics History: April 25, 1954: Bell Labs Demonstrates the First Practical Silicon Solar Cell*. APS News, 18(4):2, 2009.
- [13] A. Mohammad Bagher. *Types of Solar Cells and Application*. American Journal of Optics and Photonics, 3(5):94–113, 2015.
- [14] M. De Graef and M. E. McHenry. *Structure of materials: an introduction to crystallography, diffraction and symmetry*. Cambridge University Press, 2012.
- [15] V. M. Goldschmidt. *Die gesetze der krystallochemie (The laws of crystal chemistry)*. Naturwissenschaften, 14(21):477–485, 1926.
- [16] Akihiro Kojima, K. Teshima, Y. Shirai, and T. Miyasaka. *Organometal Halide Perovskites as Visible- Light Sensitizers for Photovoltaic Cells*. J Am Chem Soc, vol. 131:6050–6051, 2009.
- [17] J.-H. Im, C.-R. Lee, J.-W. Lee, S.-W. Park, and N.-G. Park. *6.5% efficient perovskite quantum-dot-sensitized solar cell*. Nanoscale, 3(10):4088–4093, 2011.
- [18] M. M. Lee, J. Teuscher, T. Miyasaka, T. N. Murakami, and H. J. Snaith. *Efficient hybrid solar cells based on meso-superstructured organometal halide perovskites*. Science, 338(6107):643–647, 2012.
- [19] H.-S. Kim, C.-R. Lee, J.-H. Im, K.-B. Lee, T. Moehl, A. Marchioro, S.-J. Moon, R. Humphry-Baker, J.-H. Yum, J. E. Moser, et al. *Lead iodide*

- perovskite sensitized all-solid-state submicron thin film mesoscopic solar cell with efficiency exceeding 9%*. Scientific reports, 2:591, 2012.
- [20] M. A. Green, Y. Hishikawa, E. D. Dunlop, D. H. Levi, J. Hohl-Ebinger, and A. W. Ho-Baillie. *Solar cell efficiency tables (version 51)*. Progress in Photovoltaics: Research and Applications, 26(1):3–12, 2018.
 - [21] J. Chen and N.-G. Park. *Inorganic Hole Transporting Materials for Stable and High Efficiency Perovskite Solar Cells*. The Journal of Physical Chemistry C, 122(25):14039–14063, 2018.
 - [22] J. Nakazaki and H. Segawa. *Evolution of organometal halide solar cells*. Journal of Photochemistry and Photobiology C: Photochemistry Reviews, 35:74–107, 2018.
 - [23] M. A. Green and A. Ho-Baillie. *Perovskite Solar Cells: The Birth of a New Era in Photovoltaics*. ACS Energy Letters, 2(4):822–830, 2017.
 - [24] E. Mosconi, P. Umari, and F. De Angelis. *Electronic and optical properties of mixed Sn-Pb organohalide perovskites: A first principles investigation*. Journal of Materials Chemistry A, 3(17):9208–9215, 2015.
 - [25] W.-J. Yin, J.-H. Yang, J. Kang, Y. Yan, and S.-H. Wei. *Halide perovskite materials for solar cells: a theoretical review*. J. Mater. Chem. A, 3(17):8926–8942, 2015.
 - [26] L. Yu and A. Zunger. *Identification of potential photovoltaic absorbers based on first-principles spectroscopic screening of materials*. Physical Review Letters, 108:068701, 2012.
 - [27] H. Fang and P. Jena. *Atomic-Level Design of Water-Resistant Hybrid Perovskites for Solar Cells by Using Cluster Ions*. The Journal of Physical Chemistry Letters, 8:3726–3733, 2017.
 - [28] I. Dincer and C. Acar. *Review and evaluation of hydrogen production methods for better sustainability*. International Journal of Hydrogen Energy, 40(34):11094–11111, 2014.
 - [29] Z. Zou, J. Ye, K. Sayama, and H. Arakawa. *Photocatalytic and photophysical properties of a novel series of solid photocatalysts, $\text{BiTa}_{1-x}\text{Nb}_x\text{O}_4$ ($0 \leq x \leq 1$)*. Chemical Physics Letters, 343(3-4):303–308, 2001.
 - [30] S. Dunkle and K. Suslick. *Photodegradation of BiNbO_4 powder during photocatalytic reactions*. The Journal of Physical Chemistry C, 113(24):10341–10345, 2009.
 - [31] D. Chen and J. Ye. *Selective-Synthesis of High-Performance Single-Crystalline $\text{Sr}_2\text{Nb}_2\text{O}_7$ Nanoribbon and SrNb_2O_6 Nanorod Photocatalysts*. Chemistry of Materials, 21(11):2327–2333, 2009.
 - [32] A. Kudo and Y. Miseki. *Heterogeneous photocatalyst materials for water splitting*. Chemical Society Reviews, 38(1):253–278, 2009.
 - [33] M. Ashokkumar. *An overview on semiconductor particulate systems for photoproduction of hydrogen*. International Journal of Hydrogen Energy, 1998.
 - [34] M. Ni, M. K. H. Leung, D. Y. C. Leung, and K. Sumathy. *A review and recent developments in photocatalytic water-splitting using TiO_2 for hydrogen production*. Renewable and Sustainable Energy Reviews, 11(3):401–425, 2007.
 - [35] I. K. Konstantinou and T. A. Albanis. *TiO_2 -assisted photocatalytic degradation of azo dyes in aqueous solution: Kinetic and mechanistic*

- investigations: A review*. Applied Catalysis B: Environmental, 49(1):1–14, 2004.
- [36] O. Alfano, D. Bahnemann, A. Cassano, R. Dillert, and R. Goslich. *Photocatalysis in water environments using artificial and solar light*. Catalysis Today, 58(2-3):199–230, 2000.
- [37] M. A. Fox and M. T. Dulay. *Heterogeneous Photocatalysis*. Chem. Rev., 93(January 1993):341–357, 1993.
- [38] J. M. Herrmann. *Heterogeneous photocatalysis: Fundamentals and applications to the removal of various types of aqueous pollutants*. Catalysis Today, 53(1):115–129, 1999.
- [39] I. C. Man, H. Y. Su, F. Calle-Vallejo, H. A. Hansen, J. I. Martínez, N. G. Inoglu, J. Kitchin, T. F. Jaramillo, J. K. Nørskov, and J. Rossmeisl. *Universality in Oxygen Evolution Electrocatalysis on Oxide Surfaces*. ChemCatChem, 3(7):1159–1165, 2011.
- [40] J. K. Nørskov, T. Bligaard, A. Logadottir, J. R. Kitchin, J. G. Chen, S. Pandelov, and U. Stimming. *Trends in the Exchange Current for Hydrogen Evolution*. Journal of The Electrochemical Society, 152(3):J23–J26, 2005.
- [41] T. Nagaura and K. Tozawa. *Lithium ion rechargeable battery*. Progress in Batteries & Solar Cells, 9:209–217, 1990.
- [42] D. Larcher and J. M. Tarascon. *Towards greener and more sustainable batteries for electrical energy storage*. Nature Chemistry, 7(1):19–29, 2015.
- [43] K. Kubota and S. Komaba. *Review—Practical Issues and Future Perspective for Na-Ion Batteries*. Journal of The Electrochemical Society, 162(14):A2538–A2550, 2015.
- [44] N. Nitta, F. Wu, J. T. Lee, and G. Yushin. *Li-ion battery materials: Present and future*. Materials Today, 18(5):252–264, 2015.
- [45] L. Li, Y. Zheng, Shilin Zhang, J. Yang, Z. Shao, and Z. Guo. *Recent progress on sodium ion batteries: Potential high-performance anodes*. Energy & Environmental Science, 11:2310–2340, 2018.
- [46] D. L. Williams, J. J. Byrne, and J. S. Driscoll. *A High Energy Density Lithium/Dichloroisocyanuric Acid Battery System*. Journal of The Electrochemical Society, 116(1):2–4, 1969.
- [47] S. Muench, A. Wild, C. Friebe, B. Häupler, T. Janoschka, and U. S. Schubert. *Polymer-Based Organic Batteries*. Chemical Reviews, 116(16):9438–9484, 2016.
- [48] H. Alt, H. Binder, a. Koehling, and G. Sandstede. *Investigation into the use of quione compounds for battery cathodes*. Electrochimica Acta, 17(5):873–887, 1972.
- [49] F. Goto, K. Abe, K. Ikabayashi, T. Yoshida, and H. Morimoto. *The polyaniline/lithium battery*. Journal of Power Sources, 20(3-4):243–248, 1987.
- [50] K. Nakahara, S. Iwasa, M. Satoh, Y. Morioka, J. Iriyama, M. Suguro, and E. Hasegawa. *Rechargeable batteries with organic radical cathodes*. Chemical Physics Letters, 359(5-6):351–354, 2002.
- [51] H. Kim, J. E. Kwon, B. Lee, J. Hong, M. Lee, S. Y. Park, and K. Kang. *High Energy Organic Cathode for Sodium Rechargeable Batteries*. Chemistry of Materials, 27(21):7258–7264, 2015.

- [52] R. B. Araujo, A. Banerjee, P. Panigrahi, L. Yang, M. Sjödin, M. Strømme, C. M. Araujo, and R. Ahuja. *Assessing the electrochemical properties of polypyridine and polythiophene for prospective applications in sustainable organic batteries*. Physical Chemistry Chemical Physics, 19(4):3307–3314, 2017.
- [53] R. B. Araujo, A. Banerjee, and R. Ahuja. *Divulging the Hidden Capacity and Sodiation Kinetics of $\text{Na}_x\text{C}_6\text{Cl}_4\text{O}_2$: A High Voltage Organic Cathode for Sodium Rechargeable Batteries*. The Journal of Physical Chemistry C, 121(26):14027–14036, 2017.
- [54] A. Banerjee, R. B. Araujo, M. Sjödin, and R. Ahuja. *Identifying the tuning key of disproportionation redox reaction in terephthalate: A Li-based anode for sustainable organic batteries*. Nano Energy, 47:301–308, 2018.
- [55] R. B. Araujo, A. Banerjee, P. Panigrahi, L. Yang, M. Strømme, M. Sjödin, C. M. Araujo, and R. Ahuja. *Designing strategies to tune reduction potential of organic molecules for sustainable high capacity battery application*. Journal of Materials Chemistry A, 5(9):4430–4454, 2017.
- [56] M. Born and R. Oppenheimer. *Zur quantentheorie der molekeln*. Annalen der Physik, 389(20):457–484, 1927.
- [57] P. A. M. Dirac. *The quantum theory of the electron*. Proceedings of the Royal Society of London. Series A, Containing Papers of a Mathematical and Physical Character, 117(778):610–624, 1928.
- [58] V. Fock. *Näherungsmethode zur Lösung des quantenmechanischen Mehrkörperproblems (Approximation method for solving the quantum mechanical multibody problem)*. Zeitschrift für Physik, 61(1-2):126–148, 1930.
- [59] L. H. Thomas. *The calculation of atomic fields*. In *Mathematical Proceedings of the Cambridge Philosophical Society*, volume 23, pages 542–548. Cambridge University Press, 1927.
- [60] E. Fermi. *A statistical method for the determination of some atomic properties*. Rend. Accad. Naz. Lincei, 6:602–607, 1927.
- [61] P. A. Dirac. *Note on exchange phenomena in the Thomas atom*. In *Mathematical Proceedings of the Cambridge Philosophical Society*, volume 26, pages 376–385. Cambridge University Press, 1930.
- [62] P. Hohenberg and W. Kohn. *Inhomogeneous electron gas*. Physical review, 136(3B):B864, 1964.
- [63] R. M. Martin. *Electronic structure: basic theory and practical methods*. Cambridge university press, 2004.
- [64] A. J. Cohen, P. Mori-Sánchez, and W. Yang. *Challenges for density functional theory*. Chemical reviews, 112(1):289–320, 2011.
- [65] D. Mejía-Rodríguez, X. Huang, J. M. del Campo, and A. M. Köster. *Hybrid functionals with variationally fitted exact exchange*. In *Advances in Quantum Chemistry*, volume 71, pages 41–67. Elsevier, 2015.
- [66] J. P. Perdew and A. Zunger. *Self-interaction correction to density-functional approximations for many-electron systems*. Physical Review B, 23(10):5048, 1981.
- [67] J. P. Perdew and Y. Wang. *Accurate and simple analytic representation of the electron-gas correlation energy*. Physical Review B, 45(23):13244, 1992.

- [68] D. M. Ceperley and B. Alder. *Ground state of the electron gas by a stochastic method*. Physical Review Letters, 45(7):566, 1980.
- [69] I. Mazin, M. Johannes, L. Boeri, K. Koepernik, and D. J. Singh. *Problems with reconciling density functional theory calculations with experiment in ferropnictides*. Physical Review B, 78(8):085104, 2008.
- [70] A. D. Becke. *Density-functional exchange-energy approximation with correct asymptotic behavior*. Physical review A, 38(6):3098, 1988.
- [71] J. P. Perdew and Y. Wang. *Pair-distribution function and its coupling-constant average for the spin-polarized electron gas*. Physical Review B, 46(20):12947, 1992.
- [72] J. P. Perdew, K. Burke, and M. Ernzerhof. *Generalized gradient approximation made simple*. Physical review letters, 77(18):3865, 1996.
- [73] K. Kim and K. Jordan. *Comparison of density functional and MP2 calculations on the water monomer and dimer*. The Journal of Physical Chemistry, 98(40):10089–10094, 1994.
- [74] A. D. Becke. *Density-functional thermochemistry. III. The role of exact exchange*. The Journal of chemical physics, 98(7):5648–5652, 1993.
- [75] P. Stephens, F. Devlin, C. Chabalowski, and M. J. Frisch. *Ab initio calculation of vibrational absorption and circular dichroism spectra using density functional force fields*. The Journal of Physical Chemistry, 98(45):11623–11627, 1994.
- [76] J. Heyd, G. E. Scuseria, and M. Ernzerhof. *Hybrid functionals based on a screened Coulomb potential*. The Journal of chemical physics, 118(18):8207–8215, 2003.
- [77] S. Kristyán and P. Pulay. *Can (semi) local density functional theory account for the London dispersion forces?* Chemical physics letters, 229(3):175–180, 1994.
- [78] P. Hobza, J. šponer, and T. Reschel. *Density functional theory and molecular clusters*. Journal of computational chemistry, 16(11):1315–1325, 1995.
- [79] J. Pérez-Jordá and A. D. Becke. *A density-functional study of van der Waals forces: rare gas diatomics*. Chemical physics letters, 233(1-2):134–137, 1995.
- [80] S. Grimme, J. Antony, T. Schwabe, and C. Mück-Lichtenfeld. *Density functional theory with dispersion corrections for supramolecular structures, aggregates, and complexes of (bio) organic molecules*. Organic & Biomolecular Chemistry, 5(5):741–758, 2007.
- [81] S. Grimme. *Accurate description of van der Waals complexes by density functional theory including empirical corrections*. Journal of computational chemistry, 25(12):1463–1473, 2004.
- [82] S. Grimme. *Semiempirical hybrid density functional with perturbative second-order correlation*. The Journal of chemical physics, 124(3):034108, 2006.
- [83] S. Grimme, J. Antony, S. Ehrlich, and H. Krieg. *A consistent and accurate ab initio parametrization of density functional dispersion correction (DFT-D) for the 94 elements H-Pu*. The Journal of chemical physics, 132(15):154104, 2010.
- [84] A. Tkatchenko and M. Scheffler. *Accurate molecular van der Waals interactions from ground-state electron density and free-atom reference data*. Physical review letters, 102(7):073005, 2009.

- [85] N. Ashcroft and N. Mermin. *Solid State Physics, Holt-Saunders International Editions: Science: Physics*, 1976.
- [86] J. C. Phillips and L. Kleinman. *New Method for Calculating Wave Functions in Crystals and Molecules*. Phys. Rev., 116:287, 1959.
- [87] C. Herring. *A new method for calculating wave functions in crystals*. Physical Review, 57(12):1169, 1940.
- [88] P. E. Blöchl. *Projector augmented-wave method*. Physical review B, 50(24):17953, 1994.
- [89] J. Pannetier, J. Bassas-Alsina, J. Rodriguez-Carvajal, and V. Caignaert. *Prediction of crystal structures from crystal chemistry rules by simulated annealing*. Nature, 346(6282):343, 1990.
- [90] J. C. Schön and M. Jansen. *First Step Towards Planning of Syntheses in Solid-State Chemistry: Determination of Promising Structure Candidates by Global Optimization*. Angewandte Chemie International Edition in English, 35(12):1286–1304, 1996.
- [91] A. R. Oganov and C. W. Glass. *Crystal structure prediction using ab initio evolutionary techniques: Principles and applications*. The Journal of chemical physics, 124(24):244704, 2006.
- [92] A. R. Oganov, A. O. Lyakhov, and M. Valle. *How Evolutionary Crystal Structure Prediction Works and Why*. Accounts of chemical research, 44(3):227–237, 2011.
- [93] C. Freeman, J. Newsam, S. Levine, and C. Catlow. *Inorganic crystal structure prediction using simplified potentials and experimental unit cells: application to the polymorphs of titanium dioxide*. Journal of Materials Chemistry, 3(5):531–535, 1993.
- [94] D. J. Wales and J. P. Doye. *Global optimization by basin-hopping and the lowest energy structures of Lennard-Jones clusters containing up to 110 atoms*. The Journal of Physical Chemistry A, 101(28):5111–5116, 1997.
- [95] S. Goedecker. *Minima hopping: An efficient search method for the global minimum of the potential energy surface of complex molecular systems*. The Journal of chemical physics, 120(21):9911–9917, 2004.
- [96] K. Kotmool, T. Kaewmaraya, S. Chakraborty, J. Anversa, T. Bovornratanarak, W. Luo, H. Gou, P. C. Piquini, T. W. Kang, H.-k. Mao, et al. *Revealing an unusual transparent phase of superhard iron tetraboride under high pressure*. Proceedings of the National Academy of Sciences, 111(48):17050–17053, 2014.
- [97] A. Banerjee, R. B. Araujo, and R. Ahuja. *Unveiling the thermodynamic and kinetic properties of $\text{Na}_x\text{Fe}(\text{SO}_4)_2$ ($x = 0-2$): toward a high-capacity and low-cost cathode material*. Journal of Materials Chemistry A, 4(46):17960–17969, 2016.
- [98] Q. Zhu, A. R. Oganov, C. W. Glass, and H. T. Stokes. *Constrained evolutionary algorithm for structure prediction of molecular crystals: methodology and applications*. Acta Crystallographica Section B, 68(3):215–226, 2012.
- [99] J. O. Bockris and T. N. Veziroglu. *Estimates of the price of hydrogen as a medium for wind and solar sources*. International journal of hydrogen energy, 32(12):1605–1610, 2007.

- [100] J. Rossmeisl, Z.-W. Qu, H. Zhu, G.-J. Kroes, and J. K. Nørskov. *Electrolysis of water on oxide surfaces*. Journal of Electroanalytical Chemistry, 607(1-2):83–89, 2007.
- [101] J. K. Nørskov, J. Rossmeisl, A. Logadottir, L. Lindqvist, J. R. Kitchin, T. Bligaard, and H. Jonsson. *Origin of the overpotential for oxygen reduction at a fuel-cell cathode*. The Journal of Physical Chemistry B, 108(46):17886–17892, 2004.
- [102] J. Rossmeisl, A. Logadottir, and J. K. Nørskov. *Electrolysis of water on (oxidized) metal surfaces*. Chemical physics, 319(1-3):178–184, 2005.
- [103] J. K. Nørskov, T. Bligaard, A. Logadottir, J. Kitchin, J. G. Chen, S. Pandalov, and U. Stimming. *Trends in the exchange current for hydrogen evolution*. Journal of the Electrochemical Society, 152(3):J23–J26, 2005.
- [104] E. Skúlason, G. S. Karlberg, J. Rossmeisl, T. Bligaard, J. Greeley, H. Jónsson, and J. K. Nørskov. *Density functional theory calculations for the hydrogen evolution reaction in an electrochemical double layer on the Pt (111) electrode*. Physical Chemistry Chemical Physics, 9(25):3241–3250, 2007.
- [105] A. Banerjee, S. Chakraborty, N. K. Jena, and R. Ahuja. *Scrupulous Probing of Bifunctional Catalytic Activity of Borophene Monolayer: Mapping Reaction Coordinate with Charge Transfer*. ACS Applied Energy Materials, 1(8):3571–3576, 2018.
- [106] N. Marković, B. Grgur, and P. N. Ross. *Temperature-dependent hydrogen electrochemistry on platinum low-index single-crystal surfaces in acid solutions*. The Journal of Physical Chemistry B, 101(27):5405–5413, 1997.
- [107] K. Kunitatsu, T. Senzaki, M. Tsushima, and M. Osawa. *A combined surface-enhanced infrared and electrochemical kinetics study of hydrogen adsorption and evolution on a Pt electrode*. Chemical physics letters, 401(4-6):451–454, 2005.
- [108] A. J. Medford, A. Vojvodic, J. S. Hummelshøj, J. Voss, F. Abild-Pedersen, F. Studt, T. Bligaard, A. Nilsson, and J. K. Nørskov. *From the Sabatier principle to a predictive theory of transition-metal heterogeneous catalysis*. Journal of Catalysis, 328:36–42, 2015.
- [109] R. Parsons. *The rate of electrolytic hydrogen evolution and the heat of adsorption of hydrogen*. Transactions of the Faraday Society, 54:1053–1063, 1958.
- [110] B. Hinnemann, P. G. Moses, J. Bonde, K. P. Jørgensen, J. H. Nielsen, S. Hørch, I. Chorkendorff, and J. K. Nørskov. *Biomimetic hydrogen evolution: MoS₂ nanoparticles as catalyst for hydrogen evolution*. Journal of the American Chemical Society, 127(15):5308–5309, 2005.
- [111] J. Bockris. *Hydrogen economy in the future*^{fn2}. International Journal of Hydrogen Energy, 24(1):1–15, 1999.
- [112] J. H. Montoya, L. C. Seitz, P. Chakthranont, A. Vojvodic, T. F. Jaramillo, and J. K. Nørskov. *Materials for solar fuels and chemicals*. Nature materials, 16(1):70, 2017.
- [113] P. C. Vesborg and T. F. Jaramillo. *Addressing the terawatt challenge: scalability in the supply of chemical elements for renewable energy*. Rsc Advances, 2(21):7933–7947, 2012.

- [114] M. E. Björketun, A. S. Bondarenko, B. L. Abrams, I. Chorkendorff, and J. Rossmeisl. *Screening of electrocatalytic materials for hydrogen evolution*. Physical Chemistry Chemical Physics, 12(35):10536–10541, 2010.
- [115] S. H. Mir, S. Chakraborty, P. C. Jha, J. Wärmå, H. Soni, P. K. Jha, and R. Ahuja. *Two-dimensional boron: lightest catalyst for hydrogen and oxygen evolution reaction*. Applied Physics Letters, 109(5):053903, 2016.
- [116] J. Dai, X. Wu, J. Yang, and X. C. Zeng. *Al_xC monolayer sheets: two-dimensional networks with planar tetracoordinate carbon and potential applications as donor materials in solar cell*. The journal of physical chemistry letters, 5(12):2058–2065, 2014.
- [117] R. Almeida, A. Banerjee, S. Chakraborty, J. Almeida, and R. Ahuja. *Theoretical Evidence behind Bifunctional Catalytic Activity in Pristine and Functionalized Al₂C Monolayers*. ChemPhysChem, 19(1):148–152, 2018.
- [118] C. J. Rupp, S. Chakraborty, J. Anversa, R. J. Baierle, and R. Ahuja. *Rationalizing the hydrogen and oxygen evolution reaction activity of two-dimensional hydrogenated silicene and germanene*. ACS applied materials & interfaces, 8(2):1536–1544, 2016.
- [119] S. H. Mir, S. Chakraborty, J. Wärmå, S. Narayan, P. C. Jha, P. K. Jha, and R. Ahuja. *A comparative study of hydrogen evolution reaction on pseudo-monolayer WS₂ and PtS₂: insights based on the density functional theory*. Catalysis Science & Technology, 7(3):687–692, 2017.
- [120] W. Luo, Z. Yang, Z. Li, J. Zhang, J. Liu, Z. Zhao, Z. Wang, S. Yan, T. Yu, and Z. Zou. *Solar hydrogen generation from seawater with a modified BiVO₄ photoanode*. Energy & Environmental Science, 4(10):4046–4051, 2011.
- [121] F. F. Abdi, L. Han, A. H. Smets, M. Zeman, B. Dam, and R. Van De Krol. *Efficient solar water splitting by enhanced charge separation in a bismuth vanadate-silicon tandem photoelectrode*. Nature communications, 4:2195, 2013.
- [122] X. Zhao, J. Hu, B. Wu, A. Banerjee, S. Chakraborty, J. Feng, Z. Zhao, S. Chen, R. Ahuja, T. C. Sum, et al. *Simultaneous enhancement in charge separation and onset potential for water oxidation in a BiVO₄ photoanode by W–Ti codoping*. Journal of Materials Chemistry A, 6(35):16965–16974, 2018.
- [123] J. Hu, X. Zhao, W. Chen, H. Su, and Z. Chen. *Theoretical insight into the mechanism of photoelectrochemical oxygen evolution reaction on BiVO₄ anode with oxygen vacancy*. The Journal of Physical Chemistry C, 121(34):18702–18709, 2017.
- [124] M. Oshikiri and M. Boero. *Water molecule adsorption properties on the BiVO₄ (100) surface*. The Journal of Physical Chemistry B, 110(18):9188–9194, 2006.
- [125] Y. Zhao and K. Zhu. *Organic–inorganic hybrid lead halide perovskites for optoelectronic and electronic applications*. Chemical Society Reviews, 45(3):655–689, 2016.
- [126] J. C. Tan and A. K. Cheetham. *Mechanical properties of hybrid inorganic–organic framework materials: establishing fundamental structure–property relationships*. Chemical Society Reviews, 40(2):1059–1080, 2011.

- [127] S. I. Seok, M. Grätzel, and N.-G. Park. *Methodologies toward Highly Efficient Perovskite Solar Cells*. Small, 14(20):1704177, 2018.
- [128] A. Jain, O. Voznyy, and E. H. Sargent. *High-throughput screening of lead-free perovskite-like materials for optoelectronic applications*. The Journal of Physical Chemistry C, 121(13):7183–7187, 2017.
- [129] B. Philippe, M. Saliba, J.-P. Correa-Baena, U. B. Cappel, S.-H. Turren-Cruz, M. Gratzel, A. Hagfeldt, and H. Rensmo. *Chemical distribution of multiple cation (Rb^+ , Cs^+ , MA^+ , and FA^+) perovskite materials by photoelectron spectroscopy*. Chemistry of Materials, 29(8):3589–3596, 2017.
- [130] J. H. Noh, S. H. Im, J. H. Heo, T. N. Mandal, and S. I. Seok. *Chemical management for colorful, efficient, and stable inorganic–organic hybrid nanostructured solar cells*. Nano letters, 13(4):1764–1769, 2013.
- [131] C. C. Stoumpos, L. Frazer, D. J. Clark, Y. S. Kim, S. H. Rhim, A. J. Freeman, J. B. Ketterson, J. I. Jang, and M. G. Kanatzidis. *Hybrid germanium iodide perovskite semiconductors: active lone pairs, structural distortions, direct and indirect energy gaps, and strong nonlinear optical properties*. Journal of the American Chemical Society, 137(21):6804–6819, 2015.
- [132] R. K. Misra, B.-E. Cohen, L. Iagher, and L. Etgar. *Low-Dimensional Organic–Inorganic Halide Perovskite: Structure, Properties, and Applications*. ChemSusChem, 10(19):3712–3721, 2017.
- [133] L. K. Ono, E. J. Juarez-Perez, and Y. Qi. *Progress on perovskite materials and solar cells with mixed cations and halide anions*. ACS applied materials & interfaces, 9(36):30197–30246, 2017.
- [134] T. J. Jacobsson, J.-P. Correa-Baena, M. Pazoki, M. Saliba, K. Schenk, M. Grätzel, and A. Hagfeldt. *Exploration of the compositional space for mixed lead halogen perovskites for high efficiency solar cells*. Energy & Environmental Science, 9(5):1706–1724, 2016.
- [135] O. Weber, B. Charles, and M. Weller. *Phase behaviour and composition in the formamidinium–methylammonium hybrid lead iodide perovskite solid solution*. Journal of Materials Chemistry A, 4(40):15375–15382, 2016.
- [136] J. Burschka, N. Pellet, S.-J. Moon, R. Humphry-Baker, P. Gao, M. K. Nazeeruddin, and M. Grätzel. *Sequential deposition as a route to high-performance perovskite-sensitized solar cells*. Nature, 499(7458):316, 2013.
- [137] N. De Marco, H. Zhou, Q. Chen, P. Sun, Z. Liu, L. Meng, E.-P. Yao, Y. Liu, A. Schiffer, and Y. Yang. *Guanidinium: a route to enhanced carrier lifetime and open-circuit voltage in hybrid perovskite solar cells*. Nano letters, 16(2):1009–1016, 2016.
- [138] G. Giorgi, J.-I. Fujisawa, H. Segawa, and K. Yamashita. *Organic–inorganic hybrid lead iodide perovskite featuring zero dipole moment guanidinium cations: a theoretical analysis*. The Journal of Physical Chemistry C, 119(9):4694–4701, 2015.
- [139] X. A. Jeanbourquin, X. Li, C. Law, P. R. Barnes, R. Humphry-Baker, P. Lund, M. I. Asghar, and B. C. O’Regan. *Rediscovering a key interface in dye-sensitized solar cells: guanidinium and iodine competition for binding sites at the dye/electrolyte surface*. Journal of the American Chemical Society, 136(20):7286–7294, 2014.

- [140] A. Banerjee, S. Chakraborty, and R. Ahuja. *Bromination-induced stability enhancement with a multivalley optical response signature in guanidinium $[C(NH_2)_3]^+$ -based hybrid perovskite solar cells*. Journal of Materials Chemistry A, 5(35):18561–18568, 2017.
- [141] W. Travis, E. Glover, H. Bronstein, D. Scanlon, and R. Palgrave. *On the application of the tolerance factor to inorganic and hybrid halide perovskites: a revised system*. Chemical Science, 7(7):4548–4556, 2016.
- [142] Z. Li, M. Yang, J.-S. Park, S.-H. Wei, J. J. Berry, and K. Zhu. *Stabilizing perovskite structures by tuning tolerance factor: formation of formamidinium and cesium lead iodide solid-state alloys*. Chemistry of Materials, 28(1):284–292, 2015.
- [143] A. Banerjee, S. Chakraborty, and R. Ahuja. *Rashba Triggered Electronic and Optical Properties in De Novo Designed Mixed Halide Hybrid Perovskites*. Paper V of this thesis (Nano Letter–submitted).
- [144] G. E. Eperon, S. D. Stranks, C. Menelaou, M. B. Johnston, L. M. Herz, and H. J. Snaith. *Formamidinium lead trihalide: a broadly tunable perovskite for efficient planar heterojunction solar cells*. Energy & Environmental Science, 7(3):982–988, 2014.
- [145] M. S. Whittingham. *Insertion electrodes as SMART materials: the first 25 years and future promises*. Solid State Ionics, 134(1-2):169–178, 2000.
- [146] Y. S. Meng and M. E. Arroyo-de Dompablo. *First principles computational materials design for energy storage materials in lithium ion batteries*. Energy & Environmental Science, 2(6):589–609, 2009.
- [147] P. Singh, K. Shiva, H. Celio, and J. B. Goodenough. *Eldfellite, $NaFe(SO_4)_2$: an intercalation cathode host for low-cost Na-ion batteries*. Energy & Environmental Science, 8(10):3000–3005, 2015.
- [148] J. Liu, J. Wang, X. Yan, X. Zhang, G. Yang, A. F. Jalbout, and R. Wang. *Long-term cyclability of $LiFePO_4$ /carbon composite cathode material for lithium-ion battery applications*. Electrochimica Acta, 54(24):5656–5659, 2009.
- [149] T. Yamashita, H. Momida, and T. Oguchi. *Crystal structure predictions of $Na_xC_6O_6$ for sodium-ion batteries: First-principles calculations with an evolutionary algorithm*. Electrochimica Acta, 195:1–8, 2016.
- [150] M. Armand, S. Grugeon, H. Vezin, S. Laruelle, P. Ribière, P. Poizot, and J.-M. Tarascon. *Conjugated dicarboxylate anodes for Li-ion batteries*. Nature materials, 8(2):120, 2009.

Acta Universitatis Upsaliensis

*Digital Comprehensive Summaries of Uppsala Dissertations
from the Faculty of Science and Technology 1760*

Editor: The Dean of the Faculty of Science and Technology

A doctoral dissertation from the Faculty of Science and Technology, Uppsala University, is usually a summary of a number of papers. A few copies of the complete dissertation are kept at major Swedish research libraries, while the summary alone is distributed internationally through the series Digital Comprehensive Summaries of Uppsala Dissertations from the Faculty of Science and Technology. (Prior to January, 2005, the series was published under the title "Comprehensive Summaries of Uppsala Dissertations from the Faculty of Science and Technology".)



ACTA
UNIVERSITATIS
UPSALIENSIS
UPPSALA
2019

Distribution: publications.uu.se
urn:nbn:se:uu:diva-369695